UNIVERSITY OF SOUTHAMPTON
FACULTY OF PHYSICAL SCIENCES AND ENGINEERING
Optoelectronics Research Centre

Gallium Phase Change as a Mechanism for Resonance Tuning in Photonic Nanostructures

by

Robin Francis Waters

Thesis for the degree of Doctor of Philosophy

October 2016

The investigation which is the subject of this thesis was carried out under the terms of QinetiQ Agreement No: UoSMASTSUB/1000067064

UNIVERSITY OF SOUTHAMPTON

ABSTRACT

FACULTY OF PHYSICAL SCIENCES AND ENGINEERING
OPTOELECTRONICS RESEARCH CENTRE
Doctor of Philosophy

GALLIUM PHASE CHANGE AS A MECHANISM FOR RESONANCE TUNING IN PHOTONIC NANOSTRUCTURES

By Robin Waters

This thesis covers contributions to the field of electromagnetic metamaterials, a broad, dynamic area that has produced a considerable array of new phenomena and is now looking to the prospect of tuning and switching the characteristics of novel materials and surfaces, using many means including thermal and electromagnetic excitation, in order to extend their usefulness and to enable their application in practical devices. In particular, this work develops materials that allow electromagnetic and thermal control of material optical properties and methods that facilitate the use of metasurface physics on macroscopic scales.

The reversible photoconductivity effect produced by phase coexistence in an elemental metal has been enhanced in a metamaterial for the first time. A gap plasmon absorber type metasurface was developed to enhance the photoconductivity of a gallium metal interface under near infrared illumination, achieving an order of magnitude increase in the strength of the phenomenon in a pump-probe experiment. The enhanced nonlinearity displayed at the pump wavelength of 1310nm corresponds to an effective nonlinear dielectric susceptibility $\chi^{(3)}$ of greater than $1 \times 10^{-8}\,\mathrm{m}^3\,\mathrm{V}^{-2}$.

Competing descriptions of the mechanism behind the reversible photoconductivity effect in elemental gallium, including an analytic model based on heat transfer, a non-thermal model of light-induced excitation, full finite element simulation and a novel cellular automaton method have been implemented and compared. These models have been adapted and applied to the metasurface-enhanced interface for the enhancement of the effect. It was found that an exclusively thermodynamic theoretical treatment of laser heating is insufficient to explain the magnitude of the observed excitation and hence an additional possibly non-thermal photoexcited mechanism must contribute.

Processing methods were developed for the testing of nano-imprint metamaterial manufacturing with liquid metals under controlled environmental conditions, using a custom-built pressure controlled processing chamber. Using this methodology a feasibility study of the production of a nanoimprinted liquid metal photonic structure was conducted, successfully demonstrating the infiltration of nanoscale gratings of period 600nm with liquid gallium and optical switching of the resulting composite interface.

The templated deposition of ordered arrays of gallium nanoparticles on structured substrates has been demonstrated for the first time. Bulk gallium was thermally evaporated onto substrates structured with gratings and checkerboard-type patterns of period 200 to 1600 nm. Fourier and image analysis of the produced ordering shows a pronounced tendency for the nanoparticle growth to align with the substrate patterns in both positional frequency and diameter. Such ordered arrays of metallic particles could form an active medium as a component of a plasmonic metamaterial.

Contents

List of Tables and Figures

Nomenclature

1D	One-dimensional
2D	Two-dimensional
3D	Three-dimensional
6N	99.9999 %
CCD	Charge coupled device imaging sensor
CIE	International Committee on Illumination
CMOS	Complementary metal oxide semiconductor
CVD	Chemical vapour deposition
CW	Continuous wave
DFT	Discrete Fourier transform
DNA	Deoxyribonucleic acid
EDX	Energy dispersive X-ray
EM	Electromagnetic
FEM	Finite element modelling
FIB	Focused ion beam
FP	Fabry-Pérot cavity resonance
FWHM	Full width at half maximum
GBP	Grain boundary penetration
ITO	Indium tin oxide
JJ	Josephson Junction
LC	Liquid crystal
LC resonance	Inductive-capacitative Lorentzian resonance

LSPR	Localised surface plasmon resonance
NIR	Near infrared
ORC	Optoelectronics Research Centre, Univeristy of Southampton
PET	Polyethylene tetrephthalate
PLD	Pulsed laser deposition
PVD	Physical vapour deposition
RTP	Room temperature and pressure
SEM	Scanning electron microscope
SRR	Split ring resonator
VW	Volmer-Weber

DECLARATION OF AUTHORSHIP

I, Robin Francis Waters, declare that the thesis entitled “Gallium Phase Change as a Mechanism for Resonance Tuning in Photonic Nanostructures” and the work presented in the thesis are both my own, and have been generated by me as the result of my own original research. I confirm that:

- this work was done wholly or mainly while in candidature for a research degree at this University;
- where any part of this thesis has previously been submitted for a degree or any other qualification at this University or any other institution, this has been clearly stated;
- where I have consulted the published work of others, this is always clearly attributed;
- where I have quoted from the work of others, the source is always given. With the exception of such quotations, this thesis is entirely my own work;
- I have acknowledged all main sources of help;
- where the thesis is based on work done by myself jointly with others, I have made clear exactly what was done by others and what I have contributed myself;
- parts of this work have been published as the journal papers and conference contributions listed in Appendix D.

Signed: ____________________

Date: ____________________

Acknowledgements

I would like to thank my supervisor Prof. Nikolay Zheludev for making this research possible and for his valuable input and support at key points in my studies. I would also like to thank my supervisor Dr. Kevin Macdonald for his tireless and helpful commitment to discussion of experiments and invaluable assistance in the preparation of publications.

I am fortunate to have been able to collaborate with Dr. Vassili Fedotov and visiting researchers Mr. Akihiko Ohtsu and Dr. Liwei Zhang, who contributed usefully to the research presented in this thesis. I would also like to thank Dr. Bruce Ou for his expert assistance in the preparation of experiments and the contributions of all my colleagues in the nanophotonics and metamaterials research group who have made the ORC a better place to be. I am indebted too to the support staff, who have been consistently friendly and helpful. I am thankful to have been able to work alongside all of you.

The work reported in this thesis was funded by the Defence Science and Technology Laboratory (Dstl) through the Materials And Structures Technology (MAST) Programme, via QinetiQ Ltd (Farnborough), and by the Engineering and Physical Sciences Research Council (EPSRC, grants EP/G060363/1 and EP/M009122/1). I would personally like to thank Dr. Peter Hobson of QinetiQ for his support and oversight.

Thank you finally to my family for their support and to my friends, new and old, who have made my time here so much more than the research.

Chapter 1

Introduction

Photonics is, as traditionally understood, the study of light as a quantum entity and its emission, transmission and extinction in technologies including lasers, optical fibres and sensors. Light is one of the most fundamental and most well-understood phenomena in existence, with its electromagnetic origins, physical properties and its interaction with diverse media mapped out with precision and accuracy. Over the last decade this field has been blown open with new possibilities enabled by metamaterials, but the fundamental physics remains the same.

Materials science is a much broader field, encompassing theories describing material properties from mechanical deformation and ferromagnetism through nuclear magnetic resonance and topological insulators to superconductivity. Like photonics its understanding is heavily derived from fundamental physics, but it is diversified with a much greater portion of empirical chemical data.

In this thesis entitled “Gallium Phase Change as a Mechanism for Resonance Tuning in Photonic Nanostructures”, the author investigates a confluence between these two fields: the study of how nanophotonic structures interact with the light-induced phase dynamics of a gallium surface. This is considered in this work primarily from the point of view of its status as a metamaterial and a nonlinear system. This chapter endeavours to define these and other necessary concepts in order to ground the work in the context in which it was conducted and give an overview of the thesis as a whole. Electromagnetic (EM) metamaterials are designed materials engineered to display EM wave response functions not seen in nature by combining and manipulating the structure of conventional materials in unconventional ways. The study of electromagnetic metamaterials has over the past decade become an important topic of research. Such materials have been shown to act as perfect wave absorbers,[1–3] thin and negative index lenses which enable the anomalous refraction of light,[4,5] invisibility cloaks[6] and ’rainbow traps’,[7] among many other examples. Nonlinearity may be simply described as a non-linear relationship between the inputs and outputs of a system, hence nonlinear optics describes systems for which this is true of light. For most materials, extreme intensities are necessary to observe optical nonlinearity. Larger nonlinear effects have been discovered in certain semiconductors and polymers. Many nonlinearities discovered in bulk metals arise from anharmonicities in the electronic binding function which are small corrections to the symmetric harmonic function of the ideal metal and consequently are small relative to their semiconductor and polymer counterparts, along with being difficult to access due to the lossy nature of metallic media.[8]

Consider a melting metal. Due to differences in atomic binding energy between the surface of a metallic crystal and the bulk, melting originates from the surface plane. Furthermore the suppression of binding energy can cause a suppression in the observed melting point at the interface. Under appropriate conditions a thin layer of liquid may form at the surface. This mechanism, which is most readily observed in metals, is dubbed ‘surface disordering’ or ‘surface melting’.[9]

The optical properties of gallium, specifically its bulk electric permittivity in the visual and near infrared spectra, vary considerably between liquid and solid phases of the metal. Consequently the depth of surface melting has a large effect on the reflective properties of the surface. Laser radiation has a strong effect on the observed surface melt, with the result that application of the laser strongly affects surface reflectivity. This is effectively an optical nonlinearity . By virtue of the fact that only a microscopic volume of gallium is required to melt in order to observe the change, relatively little intensity is needed to produce nonlinear reflectivity.[10] It should be noted, however, that this is not a nonlinear mechanism in the same sense as the optical Kerr effect or frequency mixing processes, as it arises primarily from light-induced heating as opposed to the direct optical excitation of electron energy levels. Consequently it is referred to as an effective nonlinearity.

Since electromagnetic metamaterials affect how light interacts with media, it is possible to enhance nonlinear properties of materials using metamaterial techniques. This is one of the most successful areas of the field and a number of different mechanisms for nonlinearity enhancement have been established.[11] However, prior to this work, enhancent of the reflective nonlinearity of a melting metal had yet to be demonstrated.

1.1 Thesis Overview

The thesis is divided into 8 chapters:

- Chapter 1: Introduction; this chapter.
- Chapter 2: Background. Supplies a history of metamaterials along with some relevant theory and a literature review of a subset of metamaterials related to the work described in following chapters.
- Chapter 3: Foundational methods and experiments. Describes the experimental work and methods used and built upon later.

- Chapter 4: Optically reconfigurable gallium phase change metamaterial absorber. Describes the construction, experimental methods and realised results of this form of electromagnetic metamaterial.
- Chapter 5: Modelling gallium phase change dynamics. Discusses the implementation of and comparisons between several methods for modelling the phase change dynamics enabling the experiment in chapter 4.
- Chapter 6: Nanoimprint-based patterning for phase change plasmonic metamaterials. Covers the development of nanoimprint-based metamaterials in both simulation and experiment.
- Chapter 7: Templated assembly of metal nanoparticle films on polymer substrates. Describes the investigation of organisation imposed on deposited gallium nanoparticle films by patterning the PET substrate.
- Chapter 8: Conclusion. Summarises the thesis and discusses future directions for research.

Chapter 2

Background

2.1 History and Fundamentals of Metamaterials

The traditional definition of an EM metamaterial is that of a 2D or 3D array of resonators, designed to produce EM response functions not observed in natural or bulk materials. An important part of this definition is that these elements are of significantly smaller dimension than the intended operating wavelength or wavelength range, such that the material may be modelled as an effective medium.

The term ‘metamaterial’ itself was coined by Rodger M. Walser[12] in the late 1990s to encompass this idea, meaning literally ‘materials made from other materials’. The extraordinary properties of metamaterials are obtained by designing resonator devices of sub-wavelength dimensions dubbed ’meta-atoms’ or ’meta-molecules’ in analogy to the effects of real atoms in, for example, photonic crystals. Arranged in arrays, the effect of such resonators may no longer be fully characterised using diffractive scattering theory, but may by described by an effective medium approximation. By changing the design of the resonators, it is possible to adjust the effective electric permittivity ϵ_r and magnetic permeability μ_r of the medium arbitrarily at the design wavelength, resulting in such exotic properties as wavefront phase tailoring and a negative refractive index (also known as double negative after the reqirement for negative ϵ_r and μ_r or left handed due to the reversal of the ’right hand rule’ governing photon fields), which in turn enables powerful applications of transformation optics such as the aforementioned electromagnetic cloaking and ’optical black holes’.[13]

While these applications are wholly new, the concept of media with extrinsic EM properties induced by manipulation of their structure is not a purely modern phenomenon. The first examples arrived not long after the unified theory of electromagnetism, prominently Bose’s demonstration that a metal-dielectric stack can act as a linear polariser for microwave radiation along with experiments with similar systems preceding the turn of the 20th century.[14] The exploitation of the near field (a modern umbrella term for sub-wavelength-scale EM phenomena) in microwave antenna design began with beam shaping experiments for the development of radar during WWII. The concept of the negative refractive index was developed in a 1968 paper by Veselago,[15] though no suggestion was given as to how it could be obtained. The first demonstration of structural magnetism, that is the generation of negative μ_r by structural design, in 1999 by Pendry et al.[16]was a key turning point, but it was not until a seminal paper by the same group in 2006[17] describing a transformation optics framework for a microwave cloak that research in the area exploded. Today metamaterials have been developed targeting a great range of frequencies from the ultraviolet to the microwave spectrum inclusive. Terahertz waves in particular are a target for development of new systems, as developing sensing technologies using other methods has proven difficult.[18]

Despite this, the picture is by no means complete. As illustrated above, a great many applications are held within the metamaterial possibility space and the majority of those in development are still in their infancy with regard to practical device manufacture. In fact only a handful of devices have made it close to that stage.[19] One contributing reason for this is that most metamaterials only function in the vicinity of the narrow frequency band for which they were designed. Many useful applications rely on materials functioning at a range of wavelengths (eg, adaptable biosensors), to adapt to environmental conditions ('cloaking', feedback effects) or to tune the strength of metamaterial-induced properties or turn them off entirely. Functional materials of this kind have already been demonstrated using a variety of different techniques[2,3,20,21] and are discussed further in the literature review section.

2.2 Metamaterial Resonance

Metamaterials utilise a plethora of different techniques to obtain the resonant responses necessary to their intended functions. Such resonance types include Fabry-Pérot (FP) cavity resonance,[3,22] LC resonance, surface plasmon resonance[23]and trapped modes.[24] Here the former three of these mechanisms most relevant to this work are discussed.

Fabry-Pérot resonance is the creation of an effective optical cavity by arranging multilayers to take advantage of multiple reflection. Not exclusive to metamaterials, this type of resonance is often harnessed in combination with other resonance types. Possibly the simplest type of FP structure is the $\lambda/4$ antireflection coating. This structure consists of a single nanoscale dielectric film on top of a surface and is designed so that the optical path length of light reflected from the lower boundary of the coating and being transmitted through the upper bounary is $\lambda/2$ longer than that reflected from the upper boundary, requiring a film of thickness $\lambda/(4n)$ where n is the refractive index of the film. This causes destructive interference between the two reflected waves and hence minimises reflectivity. This principle also applies for path differences of $3\lambda/2$, $5\lambda/2$ and so on. Hence the film thickness must satisfy

$(2m-1)\lambda/(2n)$, where m is any positive integer.

The most commonly applied source of metamaterial resonance is LC (inductive-capacitative Lorentzian resnonance). By designing elements with a natural inductance L and capacitance C (or even using standard electronic components) it is possible to tailor a resonant response in the resulting material with resonant frequency $\omega^2 = 1/LC$. This relies on a quasistatic approximation, that the wavelength is sufficiently large relative to the metamolecule that the field may be treated as static and lacking spatial variation in the implementation of the circuit model. Hence this approximation expects $\lambda \gg s$ for wavelength λ and element size s. This method is favoured due to its capacity to engineer coupling to both electric and magnetic fields of incident radiation and thus being able to vary ϵ_r and μ_r independently, often achieved using a relatively simple 2D 'split-ring' geometry.

As frequencies approach the optical spectra (near infrared to ultraviolet) this technique reduces in effectiveness as it relies on metals behaving as near-perfect conductors (or, equivalently, having a large negative value of electric permittivity), an approximation that breaks down in this spectral region. As the frequency approaches the limit of these methods, surface plasmons must be harnessed.

2.2.1 Surface plasmons

Plasmons are quanta of 'plasma oscillations' observed in the conduction band electrons of conductive materials. Their resonant frequency is known as the 'plasma frequency' of the material, given by

$$\omega_p^2 = \frac{n_e e^2}{m^* \epsilon_0} \tag{2.1}$$

where ω_p is the plasma frequency, n_e is the free electron number density, e is the electron charge, m^* is the electron effective mass and ϵ_0 is the electric permittivity of free space.[25] For gold, a metal with an extremely high free electron density, this returns a value of 2.18 PHz (corresponding to a wavelength of 138 nm), which agrees very well with the experimental value. When the operating frequency of a metamaterial approaches the plasma frequency of its constituent metals, plasma oscillation must be taken into account in its design. In this case of particular significance is the surface plasmon.

Surface plasmons are a special case of plasmon that can occur at the interface of a metal with free space (or, similarly, a dielectric). A plasmon on the metallic side of the interface may couple to a free space field oscillation on the other. The resulting hybrid quasi-particle propagates along the surface until quelled by damping in the metal.[26] Most optical-regime metamaterials take advantage of surface plasmon resonance to obtain more useful characteristics.[1,4,27,28]

Surface plasmon coupling may be understood by consideration of the

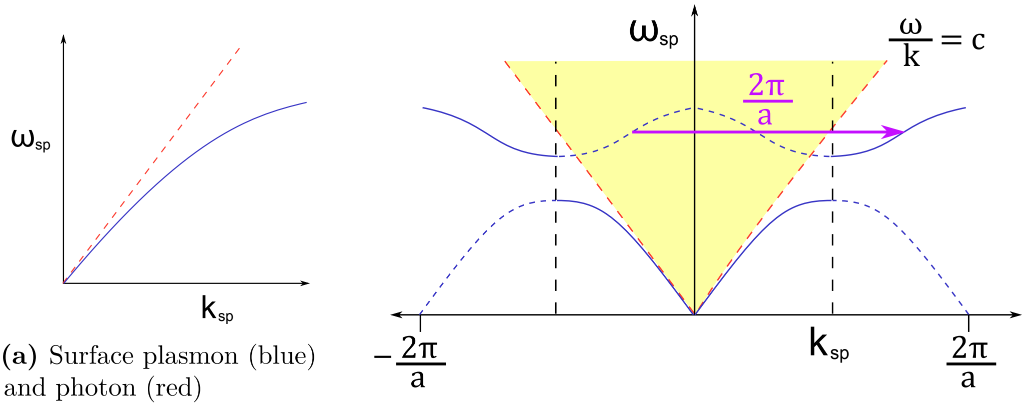

(a) Surface plasmon (blue) and photon (red) dispersion

(b) Modified surface plasmon dispersion

Figure 2.1: Dispersion relations and surface plasmon coupling. The grating enables scattering by multiples of its reciprocal lattice vector, effectively bringing the surface plasmon dispersion between the light lines (shaded area), allowing plasmonic coupling.

wavevectors of the photon and the excited plasmon. It is well known that light incident on a plane metallic interface will be reflected: there is no significant loss and hence no plasmonic coupling. This is due to a mismatch between the momentum k-vector of surface plasmons k_{sp} and that of incident photons k_λ (fig. 2.1a). By structuring the surface, however, it becomes possible for plasmons to be excited. The simplest structure to enable this is a 1D grating.[26]

As can be seen from the dispersion relations of the two in fig. 2.1a, for any given frequency, the k_{sp} is always greater than k_λ. In the planar configuration, for coupling to arise, the component of the incident light's wave vector that lies along the surface k_x must equal k_{sp}. Hence if k_{sp} can be induced to be effectively less than k_λ, then there will be a specific incident angle for which $k_{sp} = k_x$ and resonant coupling occurs. This is known as the surface plasmon resonance angle.[29] In the simple case of the grating coupler the periodicity of the grating enables a reciprocal-space scattering of k_λ by a multiple of the grating's reciprocal lattice vector $k_g = \frac{2\pi}{a}$ where a is the grating's real-space period,[30] as demonstrated in fig. 2.1b. Hence the coupling is the direct result of nanostructuring of the surface.

This description supplies an understanding of the mechanism behind plasmonic coupling in a simplified setting, but more complex systems such as metamaterials are generally best understood though using numerical simulations to extract the excited plasmonic oscillations.[31] There are often, for a given system, many plasmonic resonances available for excitation; as an example, fig. 2.2 displays a 3D plot of the localised surface plasmon resonances of a silver nanocube.[32]

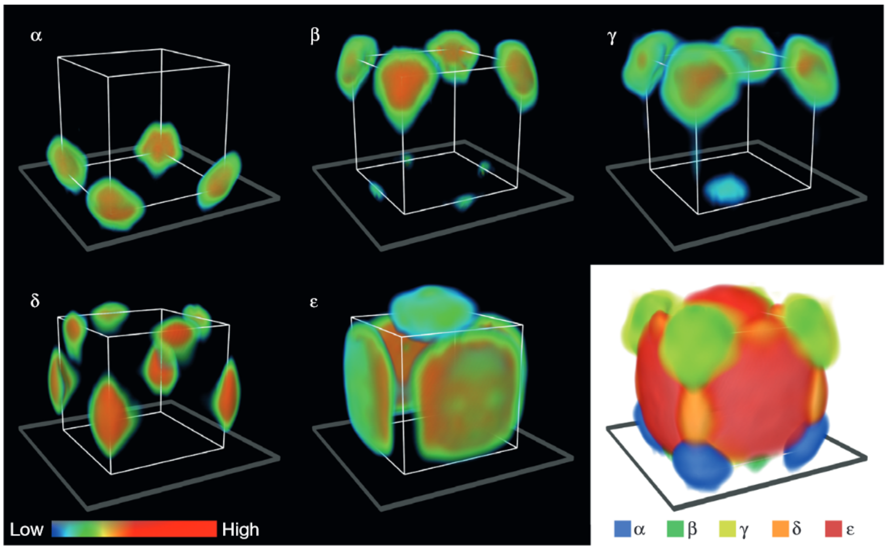

Figure 2.2: 3D visualisation of SP resonances in a silver nanocube.[32] The colour bar represents LSPR electric field intensity and the letters correspond to individual LSPR resonant modes.

2.3 The choice of gallium as an optical material

The choice of metal for metamaterial construction is usually between gold, silver, copper and aluminium.[33] Silver is generally the optimum choice as it maintains excellent metallic properties up to its plasma frequency. Gold's metallic properties are slightly inferior, but it does not suffer from oxidation to the same extent and hence is the most common choice. Copper is more attractive for lower-frequency applications due to its reduced cost. Aluminium, while generally being a poor metal, has an unusual band structure which results in superior properties in the ultraviolet while underperforming in the visible and near infrared and this has been harnassed to produce one of the highest-frequency functioning metamaterials seen to date.[34] Liquid gallium has good metallic properties which, like aluminium, extend into the ultraviolet. As a result liquid gallium is potentially useful in the construction of extreme-high-frequency metamaterials. But it is in the context of phase transitions that gallium really becomes appealing. To this end we will look at the phases of the element accessible to us.

2.3.1 Solid α-gallium

The stable crystalline form of bulk gallium at RTP (room temperature and pressure) is designated α. This phase is a one-face-centred orthorhombic crystal with atomic dimers centred around each lattice point. Correspondingly each atom has a single nearest neighbour at 2.44 Å.[35] This structure has led authors to conclude that the crystal is partially covalently bonded in nature, which is highly unusual for a metal but is bourne out by its lower reflecivity which is somewhat in line with a semiconductor or 'semi-metal'.[36,37] Due to its significantly varying lattice vectors in each axis ($a = 4.51, b = 4.49, c = 7.65\,\text{Å}$), α-gallium is highly anisotropic, with both optical and thermal properties varying considerably with orientation. As a result its optical properties are also highly anisotropic - see appendix A for the values used in each axis. However in non-ideal conditions α gallium does not form as a single monolithic crystal, but contains random deviations and changes in orientation as the melt front propagates away from its point of nucleation. As a result on the macroscopic scale the phase often does not display a single prevailing orientation but rather a mixture of crystalline orientations - a polycrystal. The standard method for determining the optical properties of a mixture of two differing media (here differing crystalline orientations of elemental gallium) is the Maxwell Garnett formula.[38] Unfortunately this forumula is invalid in the current situation as it assumes spatially separated inclusions of a secondary medium within the primary one, but in gallium volume fraction of each phase is too high to be considered an inclusion. Hence the dielectric constant ϵ of the polycrystal is approximated using the mean of the values of the three phases.

2.3.2 Liquid gallium

Gallium's liquid phase is highly reflective and displays, anomalously for a metal with partial covalent bonding, highly metallic properties across a broad wavelength band that includes the visual spectrum.[39] This may be partially due to the higher density of the liquid (by 8%), but is understood to be largely caused by a natural ordering of dimers at the liquid interface, creating a strongly concentrated layer of conduction-band electrons, as determined by X-ray scattering measurements.[40] Thus an unusually large change in optical properties is associated with solid-liquid transitions in gallium ($|\epsilon_l - \epsilon_s| \sim 90$ at $1\,\mu\text{m}$, ϵ_l and ϵ_s being respectively the complex relative permittivities of liquid and polycrystalline solid gallium), at the bulk melting point T_m of 29.76°C.[41,42] This change in optical properties is illustrated by the reflectivity spectra of the relevant phases, as displayed in fig. 2.3.

2.3.3 Metastable phases

Due to the additional degrees of freedom afforded by gallium's unusual atomic arrangement, the solid state may exist in up to nine different structural phases. There are three primary phases of crystalline gallium available in the bulk, with α-gallium (Ga-I) available at RTP and two more, Ga-II and Ga-III, available at multi-kilobar pressures.[43] The remaining phases were discovered to exist exclusively in confined nanoparticles. It has been shown that it is possible to reversibly switch between multiple of these metastable phases within a single nanoparticle by application of a laser.[44,45] More recently it was shown using high-resolution transmission electron microscopy that two phases may coexist in a single nanoparticle and the phases available are strongly affected by the type of substrate on which the nanoparticles are grown.[46]

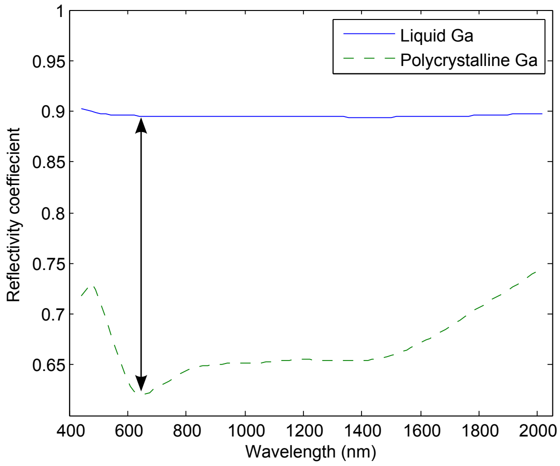

Figure 2.3: Normal incidence reflectivity of gallium metal in liquid and solid phases across the visual and near infrared spectra, compiled from the literature. The point of greatest contrast is highlighted and corresponds to an absolute change (relative to perfect reflectivity) of 0.27 and a relative change of ~42%.

2.3.4 Surface melt.

Solid gallium in conformal contact with a dielectric surface displays partial melting a few to tens of nanometres into the metal (depending on temperature and the nature of the surface), a phenomenon known as 'surface melt'. This effect has been shown to be heavily strengthened by pumping the surface using an optical laser. The speed and depth of the melting are strongly dependent on the proximity of the ambient temperature to gallium's melting point in addition to the intensity of the pump.[42] These characteristics have seen gallium previously exploited in nonlinear mirrors for laser cavity Q-switching[47] (c.f. saturable absorbers), and for all-optical and 'active plasmonic' signal modulation,[10, 48, 49] including in the form of a gallium/aluminum metamaterial composite formed by grain boundary penetration.[48] Indeed, the term 'active plasmonic' itself was originally introduced to describe functionality based upon gallium surface metallization.[50]

2.3.5 Comparison with other phase change media.

Gallium is a promising candidate for use as an optical phase change mechanism in metamaterials, but there is competition from other materials, notably those discussed in the phase change component of the attached literature review: vanadium dioxide (and derivatives) and chalcogenide glasses. The former - VO_2 - is a transition metal oxide with an insulator-to-metal thermal phase transition at 68 °C (the temperature cannot be defined more precisely than this as it is a second order transition). The latter are a class of polymorphic glasses whose phase transitions can be tuned to varying temperatures and the effects of those transitions controlled depending on chemical constituents and ratios. VO_2 displays a very large switch in optical properties (and even larger in the infrared) at its phase transition, but suffers from being extremely brittle and inconsistent: films much thicker than tens of nanometers can deform under their own thermal stress when the transition is induced, making any research involving the material highly prone to a lack of repeatability. Efforts have been made to mitigate this but have met with limited success.[51] The chalcogenides are less inconsistent but display relatively small changes in properties on transition (limited primarily to the real part of the refractive index) and require higher temperatures to switch (100 °C and above). These are both in contrast to gallium with its easily attainable transition temperature of 29.76 °C and facilitated transition through surface melt. They also transition to relatively stable phases,[52] which is useful for some applications but a hindrance in environment-responsive devices. Conversely, gallium is useful for the design of such devices, but at the cost of devices designed to function in an environment-indpendent manner. There are other metals which also display the surface melting property, but these also suffer from a relatively small change in reflectivity at the relevant phase transition.[53] Two key candidates are indium and bismuth, which have melting points of 156 and 272 °C respectively. Hence of these, gallium has the greatest change in optical properties and the most accesible melting point, thus making it the best choice in a research setting.

The usual approach to creating a metamaterial with dynamic electromagnetic properties is the hybridisation of an 'active' medium with a resonant metallic metamaterial framework. In addition to this methodology, gallium may also be used to replace the metallic backplane in the type of triple layer structure used to absorb incident radiation: this structure normally consists of a structured upper metallic layer deposited onto a dielectric spacer, which is itself deposited onto a metallic backplane. This combination of materials forms an optical cavity able to contain and hence absorb all incident radiation at the intended resonant frequency.[54] By swapping a noble metal backplane for gallium, it becomes possible to switch the quality factor of the resonant cavity and hence the quality factor of absorption. A resonance shift may be induced as well. Hence gallium's metallic nature allows it to fulfil functions excluded from other phase change media.

2.4 Other relevant properties of gallium

We have extensively discussed the attractive qualities of Gallium for application in plasmonics. However, the metal has a number of other properties which should be taken into account in its application in real devices, which are described as follows.

The low melting point of gallium. It is convenient in research to be able to simply and completely melt the metal by bringing it a few degrees above room temperature. However in application, devices are expected to be robust to changes in environent. In such cases one way to mitigate this issue is to increase the melting point by alloying it with other metals (such as iron, indium and nickel).[55] A potential application of this work, however, is to design metamaterials that are reactive to the environment. In this context temperature sensitivity is desirable.

Supercooling of gallium. Supercooling is the reduction in temperature of a material below its melting point without a corresponding change in phase. It is generally observed in extremely pure samples of material, e.g. distilled water, where there exist negligible impurities from which a crystal may nucleate. Most pure liquids are capable of supercooling by several degrees. Gallium is unusual in its ability to overcool to a much more significant degree.[56,57] It follows that gallium's response to cycles of temperature is hysteretic, which may or may not be desirable. If undesirable, introduction of impurities minimises the effect. The level to which gallium will overcool (and hence the depth of the hysteresis) is dependent on the purity of the gallium, the level to which it has been overheated above its melting point and the size of the spaces within which the gallium has been confined.[58]

The necessity to melt the material in order to obtain useful switching. Liquids are understandably not a standard component in micro- or nano-scale devices due to their relative difficulty of handling. Fortunately this problem may be alleviated through the exclusive use of the surface melting phenomenon to obtain optical switching. In such a design the vast majority of the gallium remains in solid phase with a just a nanometre scale surface of liquid providing the switching functionality. Hence the quantity of liquid involved is negligible and relatively simple to contain.

Liquid metal embrittlement.[59] This is a little-known property which is nonetheless common to many liquid metals. There is significant literature on the topic, in particular on the infiltration of aluminium by gallium, though a systematic theoretical description of this phenomenon remains elusive. The explanation put forward is a consideration of surface energy. It is known that gallium infiltrates only at the boundaries of crystalline grains; monocrystals are immune to this effect. There exist certain classes of grain boundary, for example in aluminium, which have more than twice the surface energy of a liquid gallium/aluminium surface. In this case it is energetically favourable for the gallium to fill the grain boundary when the two are brought into mutual contact.[60]

With a liquid at the interface, grain boundary sliding is very likely, which markedly reduces the mechanical strength of the composite. As a result liquid gallium should be kept isolated in most situations, a factor that may be addressed by and should be taken into account in device design. The gallium-based metamaterials documented in this thesis rely on containment of gallium by covering with a dielectric material. As an addendum, it should be noted the thermal phase switching of gallium's optical properties is still very significant after infiltration.[61]

Surface energy considerations. Some applications in this thesis require the nanostructuring of liquid gallium. Nanostructures are extremely difficult to impose upon liquids, particularly liquids with a large surface tension such as metals. The required pressure differential ΔP to obtain a structure with the desired radii of curvature is given by the Young-Laplace equation.[62] This macroscopic relation has recently been shown to be valid at the nanoscale.[63]

$$\Delta P = \gamma \left(\frac{1}{r_1} + \frac{1}{r_2} \right) \tag{2.2}$$

Here r_1 and r_2 are the orthogonal radii of curvature and γ is the surface tension.

The oxide layer. Untarnished gallium will quickly develop an oxide layer of up to 3 nm even in a low pressure environment (though high vacuum will cause the layer to dissipate[64]). The thin layer only has a small effect on surface optical properties, but strongly affects its interaction with other materials. In the absence of oxide, gallium is strongly repelled by dielectric surfaces including glass, sapphire and some plastics,[56] but oxidised gallium will adhere to such surfaces and produce a mirror surface, leaving a thin layer of metal behind if allowed to flow away.[64] The oxide layer is also a rigid solid and can even be used to hold the metal in rigid structures for a sufficiently high surface area to volume ratio.[65]

Nano-confinement. As previously discussed, freezing of a pure liquid is enabled by rare local solid crystal nucleations that propagate throughout the bulk. As a result supercooling becomes significant in very pure liquids as the incidence of these events decreases. This effect is increased further still by nano-confinement as individually confined liquid particles do not maintain a bulk over which a freeze front may propagate. Due to this phenomenon and the availability of very pure samples, nano-confined gallium has previously been shown to exhibit supercooling down from the freezing point at 29.8 °C to as low as -123 °C,[66] with no defined minimum yet discovered. It is likely that the oxide layer plays a part in isolating the liquid gallium beneath and hence maintaining the liquid phase of supercooled gallium.

2.5 Beam propagation

In this thesis is documented research using laser radiation for characterisation and excitation. Analysis of this requires a physical description of the laser beam. In experiments for which a theoretical description is required, the light beam is modelled classically at the focus only. In the focal plane the transmitted intensity of the beam is considered to have a gaussian positional dependence.

$$I(r, z) = \frac{P}{\pi r_0^2} \exp\left(-\frac{r^2}{r_0^2}\right) \tag{2.3}$$

The beam is rotationally symmetric where r is the radial distance, r_0 is the radius of $1/e$ intensity and P is the total power of the beam. From this definition we can determine that the total beam power P relates to the intensity I_0 at the focal point by $P = \pi I_0 r_0^2$. The full width at half maximum distance (FWHM) of the beam relates to r_0 by $\text{FWHM} = 2\sqrt{\ln 2}\ r_0$.

2.6 Nonlinear optics

Nonlinear optics is the study of systems displaying a non-linear relationship between light input into and output from them. The initial discovery of a nonlinear effect was in the increase in the extinction of light passing through uranium-doped glass with an increase in light intensity in 1926.[67] The discovery of the electro-optic Kerr effect, which came even earlier, could also be considered to be the origin of the field, though it was first discovered under static electric fields as opposed to those induced by light. It was not until the advent of the laser in 1960 that sufficient optical intensity was available for the phenomenon to be detected and studied in a wider variety of materials. The most prominent effects discovered include two-photon absorption (first predicted in 1931[68]), second harmonic generation[69] and the optical Kerr effect.[70]

There are several ways to describe the optical properties of a medium mathematically. The most common are the electric susceptibility, the electric permittivity and the refractive index. For electromagnetic waves (under the conventional assumption of a magnetic permeability of unity) each of these descriptions is equivalent. Nonlinear phenomena may be described using versions of these with components which depend on (powers of) electric field. Material optical nonlinearity is most commonly described using the nonlinear electric susceptibility tensor. The linear one-dimensional electric susceptibility χ relates electric polarisation density $\mathbf{P}$ to electric field $\mathbf{E}$ and the permittivity of free space ϵ_0 as $\mathbf{P} = \epsilon_0 \chi \mathbf{E}$. When generalised to include components with non-linear dependence on electric field this becomes

$$\mathbf{P} = \mathbf{P}_0 + \epsilon_0 \chi^{(1)} \mathbf{E} + \epsilon_0 \chi^{(2)} \mathbf{E}^2 + \ldots \tag{2.4}$$

which corresponds to a nonlinear electric susceptibility χ_{nl} of

$$\chi_{nl} = \chi^{(1)} + \chi^{(2)} \mathbf{E} + \chi^{(3)} \mathbf{E}^2 + \ldots \quad . \tag{2.5}$$

With sufficient knowledge of a system, it is possible to define a nonlinear coefficient which determines the reflective and transmissive properties of the material. In this case the knowledge required is the variation of the optical constants ϵ with intensity I of the medium. The most commonly chosen definition assumes a nonlinear coefficient proportional only to I and as $I \propto \mathbf{E}^2$ this is defined by $\chi^{(3)}$ (by equation 2.5). This definition has been previously used to obtain the effective $\chi^{(3)}$ of an optically thick gallium film, using $\chi^{(3)} = \Delta\epsilon/4\pi I$.[41] This is a useful approximation that functions well in defining the nonlinear properties of a bulk. It loses accuracy however when considering a more complex structure which includes a nonlinear medium as a structured component. It is not valid to assign effective medium properties such as $\chi^{(3)}$ to a metamaterial containing structures with length scales close to the wavelength; indeed it has been shown that the metamaterial lattice size must be smaller than the wavelength by a factor greater than 30 for the approximation to function correctly.[71] Hence I will not use such a description when working with a structured metamaterial and instead use a figure of merit to gauge the nonlinear characteristics of such a surface.

Under the above definition of a nonlinear response, the change in reflectivity of gallium due to incident radiation may be considered an effective nonlinearity and characterised as such. The effective value of $\chi^{(3)}$ for gallium has been estimated at $1 \times 10^{-8}\,\mathrm{m}^2\,\mathrm{V}^{-2}$,[41] which compares favourably with other methods of obtaining a nonlinear response - see fig. 2.4. From this figure it may be seen that the speed of nonlinear response and its strength have a quite consistent relationship in nonlinear materials. Through the use of metamaterials it is possible to improve upon the scaling shown to an extent, as demonstrated by the example metamaterials designed to improve nonlinear response. When the inherent reflective nonlinearity of gallium, that is, its change in laser reflectivity in response to excitation by that laser, is plotted on this graph, it is already ahead of the curve. This response is of a nature very different to that found in other nonlinear systems, being slower but having an extremely high nonlinear coefficient. Hence metamaterials based on this paradigm have a stong footing for achieving an excellent nonlinear response.

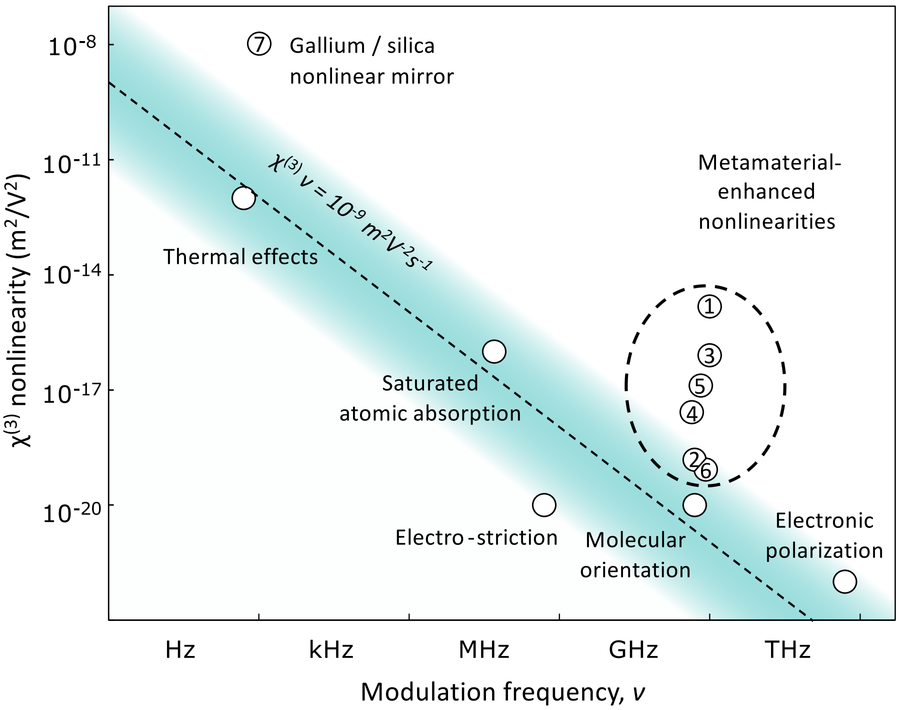

Figure 2.4: Relationship between speed and strength of nonlinear response for bulk nonlinear media, metamaterial enhancement of nonlinearity and gallium surface melting. References: 1 - split ring resonators for field confinement,[72] 2 - nanorods for field confinement,[73] 3 - SRR metamaterial hybridised with carbon nanotubes,[74] 4 - SRR metamaterial hybridised with graphene,[75] 5 - field confinement in Si layer of fishnet metamaterial,[76] 6 - field confinement in Si layer of fishnet metamaterial in a pump probe experiment and[77] 7 - a gallium/silica nonlinear mirror.[41] Unlabeled points - Boyd Nonlinear Optics.[78] Figure adapted from previous conference presentation by Eric Plum.[79]

2.7 Literature review

A gallium phase change nonlinearity based metamaterial is not merely a nonlinear system, but also a switchable and tunable ‘adaptive’ device. This review identifies the construction, active mechanisms and scope of applications of the established literature and suggests directions for growth.

Metamaterials with electromagnetic properties which depend on external inputs, henceforth ‘reconfigurable metamaterials’, have been demonstrated using a variety of techniques and materials, here categorised by tuning method. The categories covered are structural reconfiguration, magnetic tuning, semiconductor conductivity control, liquid crystals, phase change materials, component based techniques, graphene voltage biasing, superconductivity current criticality and nonlinearity maximisation.

Structural reconfiguration. The massive dependence of metamaterials’ electromagnetic responses on their internal resonant geometries is a well understood phenomenon.[80] As such, actively changing that geometry is a natural route to producing a tunable metamaterial. This idea has been demonstrated using a variety of approaches, including change in the shape,[81] rotation[82] or distribution[83] of the resonant elements. Mechanisms include harnessing Coulomb,[84] Lorentz[85] or optical forces to tune the shape of individual elements or their relative positions using ‘comb drives’,[83] thermomechanical systems such as bimetallic strips,[82] microfluidics[86] or in the case of polymer-substrate materials, mechanically deforming the substrate[87–90] - see fig. 2.5 for examples of these mechanisms.

Until recently, structurally reconfigurable metamaterials were largely limited to the infrared regime by the increasing impracticability of complex low-tolerance device manufacture at smaller scales. Comb drives, for example, require the comparatively imprecise method of isotropic etching to suspend the mobile elements, and as such are not seen at frequencies below the terahertz (THz). Coulomb, Lorentz, optomechanical and thermal mechanisms are more flexible, with the most advanced examples reaching into the near infrared (NIR). The difficulty of fabricating thousands of identical mechanical devices on the necessary nanometre scale precludes much further reduction in size; devices operating in this region are simplified relative to many of their terahertz cousins. Nonetheless, electromechanical photonic metamaterial systems providing fast continuous tuning of NIR optical properties (up to 8% optical signal modulation at megahertz frequencies) and high-contrast (250%) irreversible switching have been demonstrated.[84]

Nonlinear mechanically reconfigurable metamaterials are emerging onto the scene, using such phenomena as optical gradient forces,[91] internal magnetic coupling-induced compression and thermal expansion within arrays of helical structures[92] (see fig.2.6a), SRR compressive coupling[88] and optically induced split

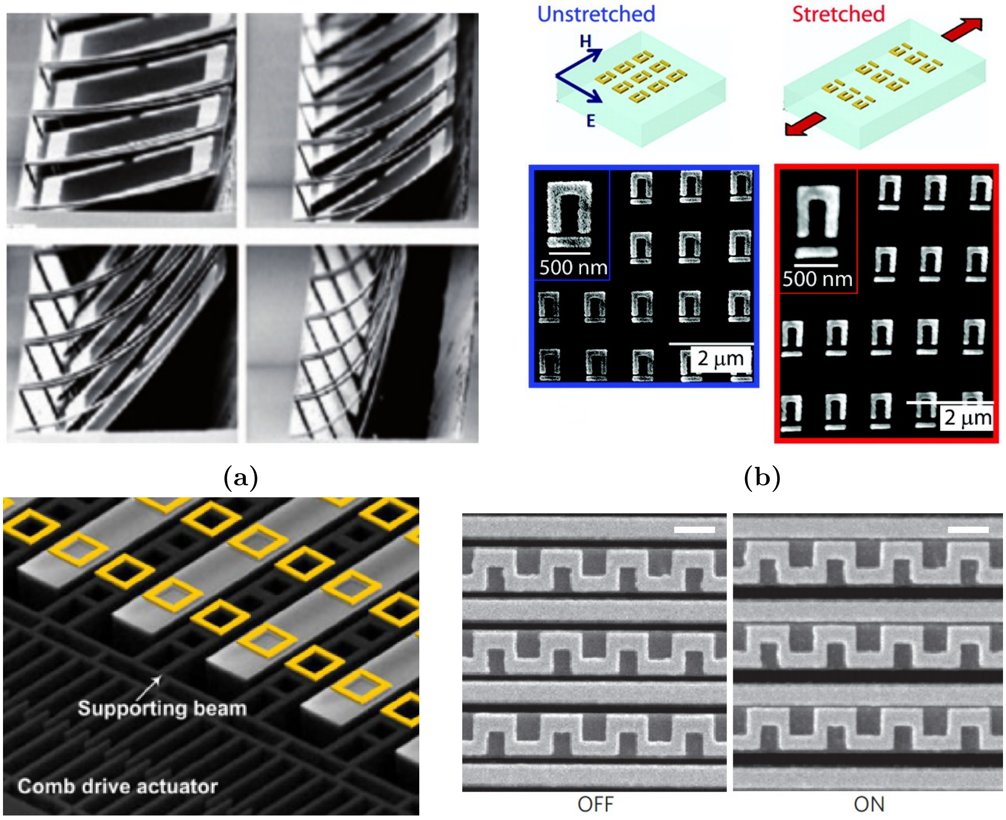

(a) **(b)**

(c) **(d)**

Figure 2.5: Structurally reconfigurable metamaterials. (a) Thermally tunable rotating split ring resonators (SRRs) for transmission modulation.[82] (b) Metamaterial reconfiguration by tensile substrate deformation.[89] (c) Electromechanical reconfiguration to create and destroy polarisation symmetry.[83] (d) NEMS (nanoelectromechanical systems) for transmission control in the near infrared.[84]

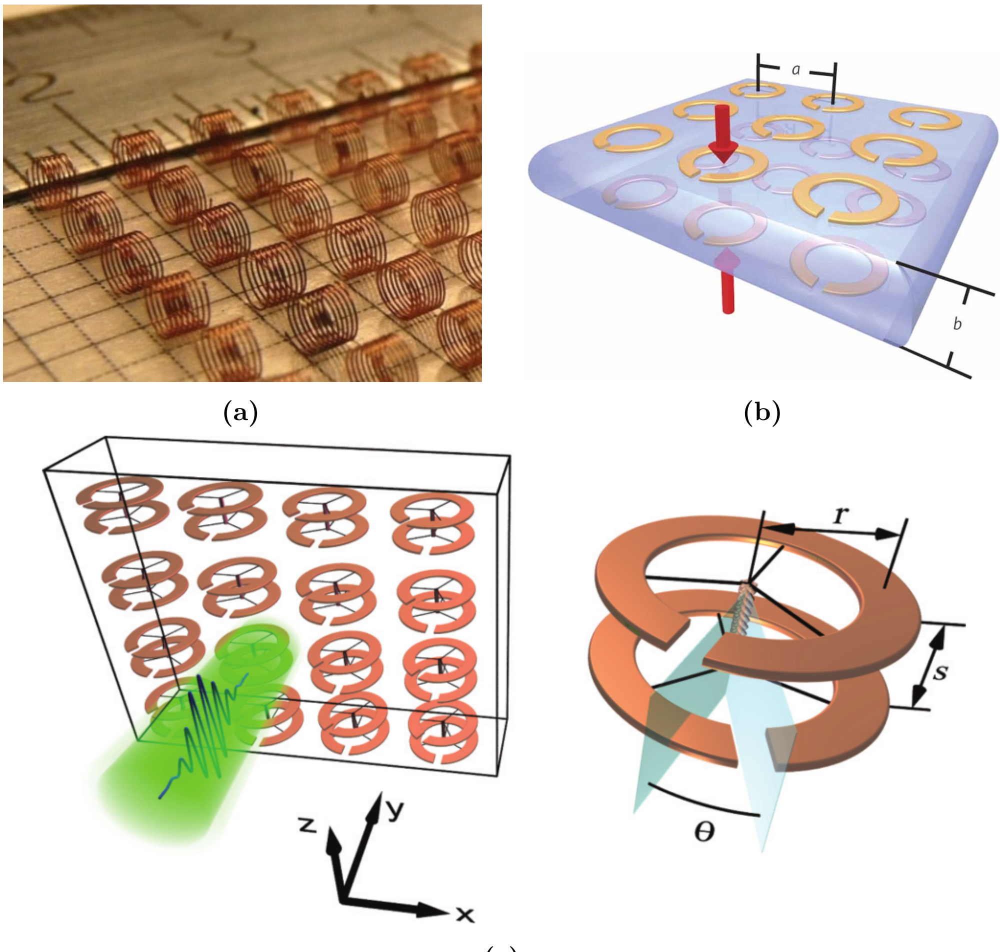

(a) (b)

(c)

Figure 2.6: Nonlinear reconfigurable metamaterials utilising (a) helical-element magnetic coupling compression[92] (b) substrate deformation though magnetic coupling in SRRs[88] and (c) SRR rotation.[94]

ring resonator (SRR) rotation (both theoretically[93] and experimentally[94]).

There is increasing interest in the application of polymers as substrates in order to take advantage of their mechanical properties. One example by Fan, Zhang et al. demonstrates the production of an optically tunable flexible metamaterial operation in the terahertz.[95] This method enables metamaterials to conform to curved surfaces, a desirable element in practical application,[96] but limits substrate choice to flexible plastics, which have relatively low refractive indices and poor electical conductivity. One use to which this substrate type has been put is applying tension to the substrate, changing the relative positions of resonator elements positioned on it and thus tuning the frequency response of those resonators - see fig. 2.5b.

Reconfiguration-type methods in general are powerful in their control of a metamaterial's properties: moving resonators relative to one another can create or destroy polarisation symmetry (see fig.2.5c), entirely suppress or create resonances anew or experimentally exhibit transmission modulation contrast of up to 30dB.[97] These benefits often come at the cost of relatively low switching speeds, where the magnitude of induced displacements is traded against the size and therefore resonant mechanical frequency of components. The more exotic systems such as deformable substrates and microfluidics are at a relatively early stage and more studies are needed to reach firm conclusions, though modulation frequencies will likely be limited to the kilohertz.

Optomechanical and electrically actuated metamaterials' material breakdown thresholds limit performace: for example, the current density damage threshold of nanoscale conductive paths. Similar issues arise when working with large electric fields and high laser intensities. The necessity of approaching material constraints in order to obtain appreciable tuning, even when using ideal materials such as noble metal conductive elements, implies that these methods are not well suited to practical applications, unless radically more efficient mechanisms are revealed.

Magnetically switchable metamaterials are tuned by variation of the magnetic field externally to the metamaterial by SRR resonance hybridsation with a magnetic material.[98,99] See fig. 2.7a for an example of this type of metamaterial investigated computationally. There are as yet only a handful of publications in this category, but new research is ongoing.[100] Currently these metamaterials have only been proven viable in the GHz and THz regimes and require large external fields to exhibit significant switching (e.g. of the order of 0.5 Tesla[98]), though the paradigm may offer opportunity for improvement.

Semiconductor switchable metamaterials. The conductivity of doped semiconductors can be varied wildly by external factors such as illumination and temperature, with carrier concentrations varying by up to several orders of magnitude in highly doped cases. Due to this semiconductors may be integrated into metamaterials to realise tuning as the substrate[101–103] or part[20,104] or all[105] of the resonators themselves - or, in one theoretical case, the entirety of the metasurface in question.[106] Semiconductors convey the benefits of simple switching techniques, robust solid-state implementation and a huge range (up to 10 orders of magnitude[102]) of conductivity control. Switching is attained through thermo- or photo-excitation of the charge carriers within the semiconductor, enabling control of the material's extrinsic properties. This is commonly achieved by using semiconducting 'bridges' between metallic elements,[20,104] enabling the effective geometric parameters of the conductive elements to be continuously varied by charge carrier excitation (see fig. 2.7b for examples). Semiconductors, being the primary building block of the silicon chip, present the dual benefits of nanosecond-or-below switching times and excellent nanolithography process compatibility. However, the absolute levels of conductivity obtainable within semiconductors are not as high as some of the materials used in, for example, phase change reconfiguration, and as a result the achieved changes in optical properties are relatively small. Nor are they sufficient to compete with what has been achieved

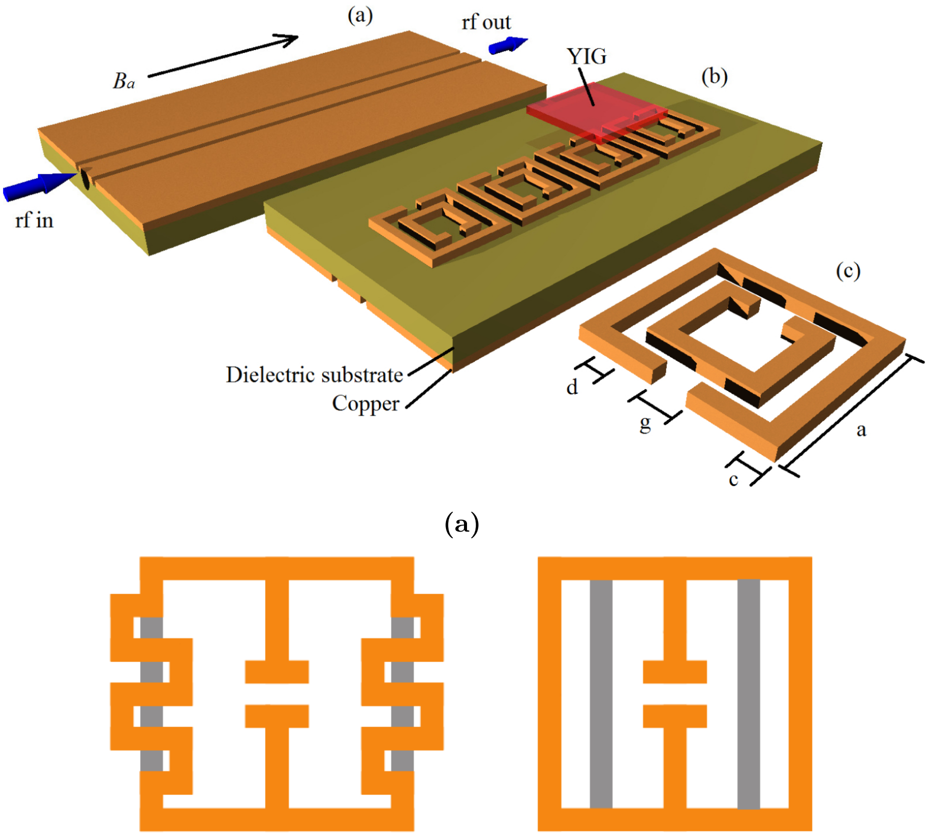

(a)

(b)

Figure 2.7: Magnetic-field and semiconductor switchable metamaterials. (a) Magnetically tunable metamaterial employing yttrium iron garnet.[98] (b) Semiconductor-tuned metamaterial unit cell designs. Metallic elements are shown in orange, semiconducting inclusions in grey. As the conductivity of the semiconductors is increased, portions of the metallic resonators are bypassed, changing their resonant frequency. Figure is adapted from Chen et al.[20]

through mechanical reconfiguration. Despite this shortcoming, transmission modulation from 15% to 70%[107] and frequency tuning of up to 26%[108] have been obtained using semiconductor reconfiguration at wavelengths in the terahertz.

Phase change switchable metamaterials take advantage of a strong change in electromagnetic properties at phase transitions of certain materials. This class of metamaterials typically comprise a metallic structured layer either on or under an unstructured active layer of phase change material. The material then either suppresses or enhances resonances in the structured layer, depending on its phase state at any given time. The phase transitions of these materials may not be induced exclusively thermally, but also through photoexcitation[109, 110] and voltage application.[110, 111] Metamaterials in this category exhibit some of the strongest switching capabilities, with modulation contrasts of up to 40dB reported.[112]

The current phase change material of choice for commercial application is chalcogenide glass. This class of material exhibits highly discontinuous electromagnetic properties across phase transitions, in particular, transitions between amorphous 'glass-like' and crystalline states. The nature and temperatures of the phase transitions, as well as the refractive index of the glass, may be tuned by varying the ratios of the constituent elements or by doping.[113] The transitions may also be induced electrically or optically, a method established as the basis of phase change memory in re-writable discs and emergent forms of electronic random access memory. Major motivations to use chalcogenides in particular include their high refractive index switching contrast, non-volatile switched states (for applications in phase change memory) and low loss dielectric nature. On the other hand, the relatively stable switching involved requires an active energy input to be reversed and the quality of the switching is significantly degraded after large numbers of cycles.

Recent work in the area of chalcogenide metamaterials, most notably from the University of Southampton, has demonstrated electro- and all-optical, reversible, non-volatile switching in the near- to mid-IR spectral range with transmission/reflection contrast ratios of 4:1 from device structures of highly subwavelength ($\simeq \frac{\lambda}{27}$) thickness (fig. 2.8a) metamaterials.[114, 115] New concepts are also now emerging elsewhere based on finite element computational modelling.[116, 117] More recent work includes a rewritable metamaterial analogue of a Fresnel lens produced by selective laser crystallisation of chalcogenide glass[118]

Another phase change technology being applied in switchable metamaterials is vanadium dioxide (VO_2). VO_2, unlike chalcogenide glass, exhibits a Mott insulator-to-metal transition when heated to 68 °C.[119, 120] Such a phase transition displays a very strong change in optical properties,[121] in particular because metallic-phase VO_2 is able to propagate surface plasmons, but this metallic nature introduces losses into the system. In addition to thermally, the transition has also

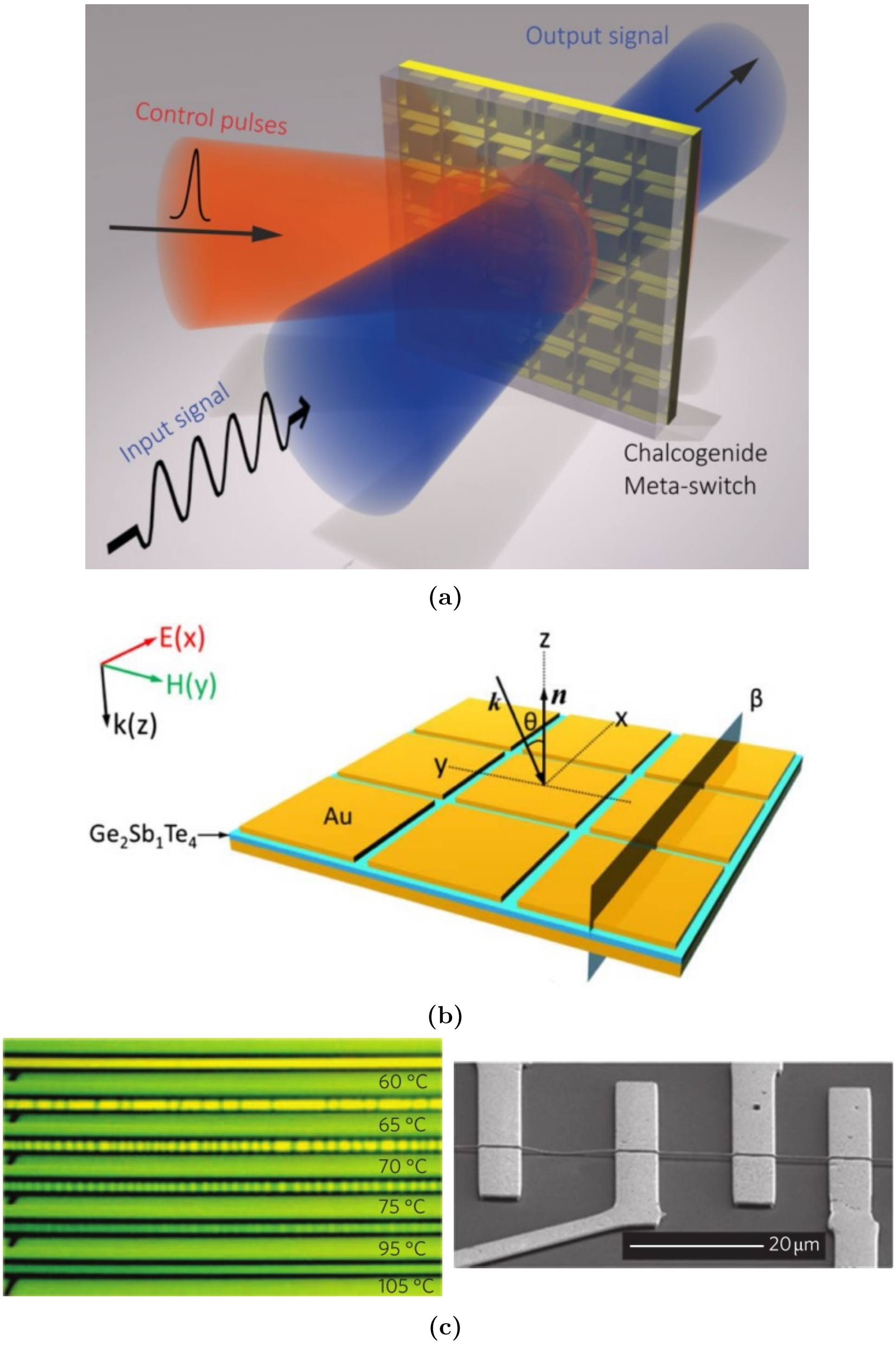

Figure 2.8: Phase change materials and metamaterials. (a) Chalcogenide glass transmission switch.[115] (b) Chalcogenide-based absorption modulator.[116] (c) Vanadium dioxide nanobeams. Left: demonstration of insulator-metal transition in vanadium dioxide nanobeams as viewed under optical microscopy.[51] Right: SEM imagery of suspended nanobeams.

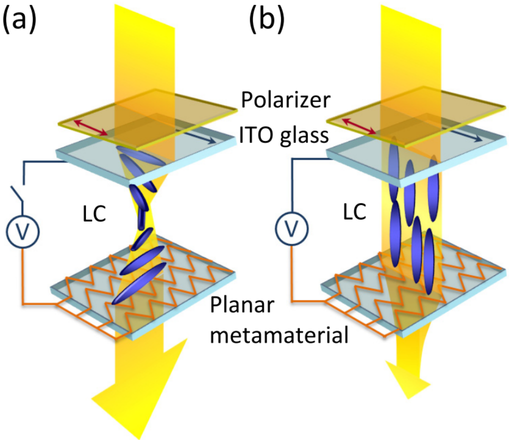

Figure 2.9: Liquid crystal metamaterial.[127] A liquid crystal (LC) alignment layer is applied to the upper ITO interface, inducing the LC at that interface to align in a given direction. At the opposing interface the metamaterial itself acts as an alignment layer orthogonal to the first, producing 'twisted' LC alignment in the intervening space (a). When a voltage is induced across the LC (using the ITO and metamaterial as electrodes), it aligns with the electric field (b). The variation in the liquid crystal's alignment controls polarisation rotation of the incident light, influencing coupling to the metamaterial and hence modulating transmission.

been shown to be excited by optical and THz pulses[122,123] and electric fields.[111] Maximal VO_2 switching is dependent on temperature variation over a broad range for an optimal response,[124] though considerable modulation is possible under less extreme conditions. In photonic (near-/mid-IR) metamaterial systems VO_2 has been seen to provide transmission absorption resonance tuning of up to ~20%[21,125] and the concept of 'gradient index' resonance modulation has been demonstrated for VO_2-hybridized THz split ring resonators.[126] VO_2 films show degradation due to intrinsic thermal stress induced by the deposition mechanism and sometimes unrepeatability of results due to domain motion through switching cycles. These limitations can be circumvented by producing the compound in much more ordered nanobeam domains[51] (see fig. 2.8c) but this method introduces limitations of its own, specifically that deposition is limited to this type of confined domain rather than the more useful continuous film. Arguments for the use of VO_2 come in the form of impressively strong reflectivity switching and fast unidirectional switching times (<2ns);[111] the metamaterials designed to harness it may thus show extremely strong switching of up to ~40dB,[112,124] though the most impressive changes are achieved using cryostat temperature control, a relatively slow and impractical technique.

Liquid crystal (LC) switchable metamaterials have been harnessed to influence electromagnetic waves from the terahertz to the optical.[128,129] Engineered effects of LC metamaterials include transmission control,[130] adjustable absorbers[131] variable phase shifters[132] and tunable negative refractive indices.[133] A number of working mechanisms have been published, from simple thermal phase switching of an LC-immersed metamaterial array[128] to complex systems involving gain media (electromagnetic materials in which input radiation can excite the release of additional radiation) and LC alignment through electric fields and other means. The majority of LC-metamaterials use a metamaterial-LC-electrode sandwich approach, where the electrode is made of a transparent conductor such as indium tin oxide (ITO).[127,130,131] By inducing a voltage difference between the metamaterial and the electrode the LC can be aligned out of the sample plane, producing response switching. More complex implementations use LC alignment structures on the upper and lower surfaces of the LC layer to further strengthen switching;[127,134] fig. 2.9 shows one example developed at the University of Southampton.[127] In this work the alignment, polarizer and electrode layers of a conventional twisted nematic LC cell are replaced by a single metamaterial layer and resonant transmission modulation with a contrast ratio of 5:1 at 7 V is delivered. In a subsequent planar geometry[135] intensity and phase modulation of terahertz radiation is achieved via in-plane reorientation of LC molecules. Modulation depths of around 15dB have been reported in LC metamaterials and reproducibility is excellent, with devices being stable over many thousands of switching cycles. However LC mechanisms typically require more involved multilayer deposition processes than other methodologies and switching typically occurs over a millisecond or more, thereby precluding application in certain processes such as those required in microelectronics or high-speed sensing.

Graphene switchable metamaterials are a relatively recent development, following from the wider ranging interest in the (opto)electronic properties of the material. Graphene based metamaterials may offer improved functionality through graphene's unique attributes of massless two-dimensional electrons and linear band structure.[138] Inclusion of graphene in metamaterials has only recently been demonstrated[136] (fig. 2.10a), but tunable variants harnessing these properties are already becoming established. Tuning of fabrication parameters has enabled absorption variation approaching 100% in the terahertz using graphene-insulator stacks[139] despite an intrinsic monolayer absorption of ~2%.[140] As a result the tremendous modulation promised by graphene's unique band structure is difficult to harness; early work on actively tunable metamaterials using graphene micro-ribbon structures showed broad-band transmission resonance tuning but a small modulation depth of ~1%.[138] However more recent successes by Zhu et al. show dispersion tuning of an optical fishnet metamaterial[137] (see fig. 2.10b) and NIR reflectivity increases of up to 261%[141] of the minimum level. In both cases tunability is obtained by applying a bias voltage to a single graphene monolayer embedded in the metamaterial. This is much like the tuning method in semiconductors and the switching is very fast as a result. A nonlinear variant has also appeared with fast optical modulation of ~1%.[75] More recently an infrared

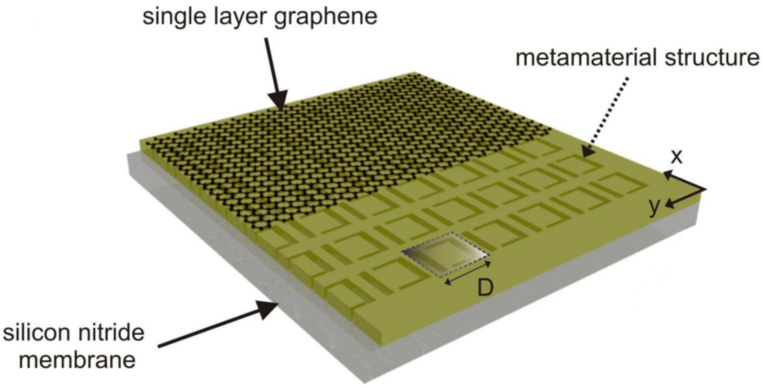

(a)

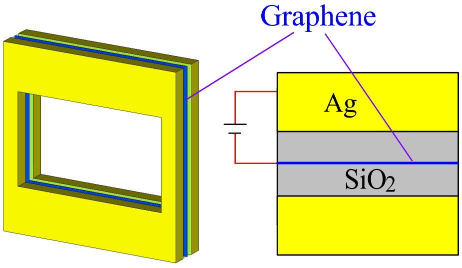

(b)

Figure 2.10: Graphene switchable metamaterials. (a): The first example of a metamaterial incorporating graphene.[136] (b): Graphene voltage bias tunable negative index metamaterial. Image adapted from.[137]

reflectance control metamaterial was developed that exhibits an electrical-doping-induced inversion in reflected polarisation of 80%.[142] Graphene has also been harnassed in the reshaping of terahertz beams as a nonlinear function of their intensity.[143] Graphene's virtually unique properties, in particular its exhibition of linear dispersion and Dirac points make it extremely useful in engineering novel phenomena. However its status as an atomically thin material with an intrinsic absorption of around 2% makes achieving this quite difficult, with many applications relying on 'graphene multilayers' which dilutes the more interesting properties of the material. Expensive dedicated equipment is also needed to make large contiguous sheets of graphene and most research is conducted with smaller 'flakes' exfoliated from monolithic graphite, which is harder to work with and produces less reproducible results.

Component-based switchable metamaterials incorporate discrete circuit components (capacitors, transistors etc) that are readily bought or manufactured in place. Some implementations use off the shelf components (generally for microwave or millimetre wave metamaterials) while others use in-place manufacturing to build semi-standard components directly on the metamaterial. The component most often integrated is the varactor diode[2, 144–146] due to its highly nonlinear capacitative response to applied voltages. The diode is placed at a strategic location in each metamaterial resonator, then its capacitance is varied by voltage biasing the resonator elements on either side of it. This enables modulation of electronic coupling within resonators, affecting the resonant response of the metamaterial. In-place manufactured transistors have also been used to control carrier concentrations within metamaterial elements.[147] Schottky diodes may also be manufactured in place through appropriate choice of the materials used for the substrate and the metamaterial array.[18, 101] Through the use of individually electrically connected collections of meta-atoms ('pixels') such a paradigm has additionally been used to obtain spatially controlled transmission modulation in the terahertz.[148] Component integration brings the advantage of greater control of the resonators' operational parameters but at the cost of increasing the minimum size of the individual elements; most of the metamaterials in this category function only in the microwave or, in some cases, the longer-wavelength end of the terahertz spectrum. The switching and nonlinear characteristics achieved are exemplary, but applications are limited to the microwave.

Superconductivity breakdown switchable metamaterials take advantage of the critical current phenomenon in superconductors whereby superconductivity is only maintained up to a certain threshold current. The transition to a non-superconducting state has a large effect on the resonant properties of the metamaterial itself, enabling high-sensitivity switching in response to a variety of thermal, electric, magnetic, and photonic excitations. Due to the nature of the

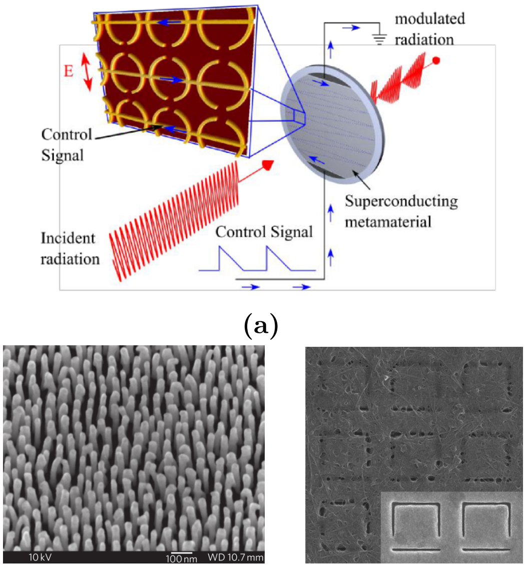

(a)

(b) (c)

Figure 2.11: Nonlinearity maximisation switchable metamaterials. (a): Superconductivity breakdown GHz modulator.[149] (b): Nanorod nonlinear metamaterial.[73] (c): carbon nanotube & nanostructured gold film hybridised nonlinear metamaterial.[74]

process the metamaterial must be both electrically connected and cryogenically cooled. This phenomenon has been successfully demonstrated in the gigahertz (GHz) regime[149] for transmission modulation (fig. 2.11a) and as the basis of a planar metamaterial bolometer.[150] This effect can be induced on a fast timescale, but relies on conductive cooling to return to a superconducting state, with a wait time on the order of microseconds. Like all superconduction-related phenomena, it is confined by photon energy to the sub-THz spectral range and requires cryogenic cooling to manifest, though the latter is no longer the bar to practical application it once was.

Nonlinearity maximisation switchable metamaterials. The implicit subwavelength thickness of metasurfaces normally precludes the application of conventional electronic nonlinearities in such systems; laser spectral broadening systems, for instance, can use hundreds of wavelengths of nonlinear material to obtain their desired result. It has been shown, however, that nanostructuring thin sheets of nonlinear material can massively increase their effective nonlinear response through electric field enhancement within the structures[73] - see fig. 2.11b. This method shows fast (femtosecond to picosecond) modulation contrast of up to 80%. The near-IR excitonic nonlinearity of carbon nanotubes can be enhanced by more than an order of magnitude through hybridization with photonic metamaterials[74,151] (fig. 2.11c) and indeed the nonlinearity of the metal of the metamaterial framework itself can be enhanced via nanostructuring.[72] An impedance matching metamaterial has been designed taking advantage of Josephson Junctions (JJ) and SQUID (Superconducting quantum interference device) phemomena to obtain frequency tuning of up to 50%. Additionally a paper has been published describing a thermally and magnetically tunable JJ-based SQUID metamaterial with a total tunability of ~56%. Other work exhibits the use of electric field confinement to affect the nonlinear response,[152] one in particular by Al-Naib et al. showing a 50nm phase shift for an optical nonlinear absorber at incident powers as low as $6\mu W/\mu m^2$.[153] Nonlinear mechanisms can be relatively fast, up to the femtosecond range, but tend to show relatively low levels of switching and necessarily switch radiation at the same wavelength used for excitation, which may or may not be desired, depending on application.

Conclusions. This review reveals an increasingly busy field, albeit one as yet some distance from practical application and with room for unusual approaches. The research focuses on attempting to produce functional materials with high levels of switching at wavelengths as short as each technology makes possible. Speed of response and efficiency of excitation of that response are generally considered secondary concerns as researchers attempt to make the next jump in functional frequency. There is a considerable body of work on metamaterial systems employing only dielectric materials in order to minimise losses,[154] but with the exception of some chalcogenide glass based materials, this does not generally extend to reconfigurable metamaterials, with the vast majority based on the same plasmonic principles used since the first experiments demonstrating the negative refractive index.

Metamaterials based on gallium fit into this picture well for several reasons. Of relevance here is the efficiency of excitation (specifically the laser intensity needed to excite it), the speed of the response and the range of wavelengths over which a response can be engineered. Referring back to fig. 2.4, the effective nonlinear coefficient $\chi^{(3)}$ of gallium is on the extreme end of what is possible in any material. Given the inverse relationship between $\chi^{(3)}$ and the speed of response that is seen in the same figure, this means gallium's response to excitation, i.e. the full time until a response has subsided, is relatively slow, in at least the sub-microsecond range. This informs the applications to which gallium's nonlinear response may be applied: the slow response rules out high-speed electronics, but the excellent effective $\chi^{(3)}$ nonlinear coefficient lends itself to applications requiring high sensitivity such as biomedical sensing, gas sensing and detection of infrared radiation.

Chapter 3

Foundational Methods and Experiments

3.1 Thin film multilayers

The field of metamaterials has by and large turned to thin ’metasurfaces’ for the development of the unique properties available through subwavelength structuring. Accordingly most metamaterial structures consist of multilayers, generally with a degree of patterning. Hence methods of depositing, structuring and modelling the optical properties of thin film multilayers become necessary; this subsection covers these.

3.1.1 Theory

The work with multilayer films documented in this thesis involved normal incidence reflection from isotropic absorbing films, so this subset of thin film theory will be the focus of this section. The following formalism can be generalised to the cases of angled incidence and anisotropic films.

The optical properties of thin films may be calculated using a variety of techniques which are useful in different situations. In the case of multilayer films it is most convenient to use the transfer-matrix method.[155] In this method the form of calculation is

$$\begin{bmatrix} E_T \\ F_T \end{bmatrix} = \mathbf{M}. \begin{bmatrix} E_I \\ F_I \end{bmatrix} \tag{3.1}$$

where E_I and E_T are the incident and transmitted electric fields and $F_i = dE_i/dz$ for a multilayer aligned along axis z. $\mathbf{M}$ describes the overall effect of a series of mutually aligned media and is related to the individual matrices defining the properties of each medium by

$$\mathbf{M} = \mathbf{M}_n.\mathbf{M}_{n-1} \ldots \mathbf{M}_2.\mathbf{M}_1 \tag{3.2}$$

for n elements where $\mathbf{M}_1$ is the first element encountered by incident radiation and $\mathbf{M}_n$ is the last. For a single homogeneous isotropic absorbing film j, $\mathbf{M_j}$ is defined as follows.

$$\mathbf{M_j} = \begin{bmatrix} \cos(n_j k d_j) & \frac{1}{k}\sin(n_j k d_j) \\ -k\sin(n_j k d_j) & \cos(n_j k d_j) \end{bmatrix} \tag{3.3}$$

where k is the wavenumber of the incident radiation, $n_j = n'_j + in''_j$ is the complex refractive index of the film and d_j is the thickness of the film. This may be used along with equation 3.2 to describe the overall properties of an arbitrary thin film multilayer.

The intensity reflection coefficent R of a multilayer is then given by[156]

$$R = \left[\frac{(\mathbf{M}_{21} + kn_I kn_T \mathbf{M}_{12}) + i(kn_I \mathbf{M}_{22} - kn_T \mathbf{M}_{11})}{(-\mathbf{M}_{21} + kn_I kn_T \mathbf{M}_{12}) + i(kn_I \mathbf{M}_{22} + kn_T \mathbf{M}_{11})}\right]^2 \tag{3.4}$$

where n_I and n_T are the complex refractive indices in the incident and transmission media. This method is highly convenient for thin films of many layers as it can be easily evaluated using matrix software such as MATLAB. The direct calculation can quickly become cumbersome as the number of layers increases.

3.1.2 Thin film deposition

The deposition of thin films was conducted using two differing forms of vacuum evaporation: resistance and electron beam evaporation. These are both forms of physical vapour deposition (PVD). The former vacuum process functions by the simple expedient of passing a current through a tungsten crucible containing the source material until the increasing vapour pressure of the material causes material to be deposited, as measured by a quartz crystal microbalance. The sample substrate is placed on a turntable above the source to ensure an even coating. Electron beam evaporation functions equivalently but uses a high intensity electron beam, directed into a crucible via magnetic field, to heat the source.

3.1.3 Patterning and imaging

Both patterning and sub-optical imaging are enormously facilitated through access to a FEI company dual beam combination SEM (scanning electron microscope) and FIB (focussed ion beam) system. The SEM component of the system enables imaging of nanoscale objects by sequential raster scanning of the area to be imaged (again, controlled by magnetic fields) and sampling the backscatter with a CCD. The FIB component uses an analogous system to direct the path of gallium ions, through which both patterning and imaging of the target are enabled. The dual beam is limited by the fact that a conductive surface is required for processing (necessitating deposition of metals onto dielectrics to be patterned) and because it causes some level of contamination of samples with gallium. On the other hand, it may pattern virtually any material efficiently, with the main limiting factor being that only a small area (up to 500 microns across or so) may be reasonably patterned at a time. This particular method was chosen for the patterning due to the short turnaround time for prototyping and inspection of the patterned structures under SEM. Other methods such as photolithography and wet etching require additional steps for mask preparation and process optimisation.

3.2 Characterisation

The primary characterisation tool used was microspectrophotometry. Certain experiments used further tools and these are discussed in the relevant chapters. The microspectrophotometer consists of a standard digital imaging optical microscope with an additional optical element: a small mirror is positioned in the output beam such that the vast majority of the signal goes to the imaging CCD and a small specified component is redirected to the spectrophotometer. The spectrophotometer uses a monochromator and CCDs to determine the spectral makeup of the signal in the chosen area. There are two CCD sensors: a standard silicon-based device that operates in the range of 400-950 nm and an InGaAs sensor that operates across 900-2000 nm. As a result a very large frequency band may be sampled at a time. The system takes readings with the two sensors sequentially - first silicon then InGaAs. Readings in the overlap range of the two sensors are linearly interpolated. Slight mismatches between readings from each sensor are common and show up as sudden deviation across the 900-950nm spectral range.

The microscope may be set up in either transmission or reflection modes. In both cases the sample is illuminated using a halogen bulb with a 3200 K black body emission spectrum, with a linear polariser inserted before the condensing lens. Reflectivity readings are calibrated to a silver mirror reference and a Vantablack (low-reflectivity carbon nanotube ’carpet’ surface) sample zero-point. The true reflectivity from a sample is calculated by mapping the experimental reading to a Drude-model derived fit of the reflectivity of pure silver. Transmission readings use an unobstructed beam as a reference and an optically thick aluminium plate in the place of the sample as a zero-point.

3.3 FEM simulation

Unless stated otherwise, all simulations in this thesis were conducted using the radio-frequency module of commercial finite element modelling (FEM) software COMSOL multiphysics™. COMSOL in particular was chosen for its capacity to simulate interconnected physical systems should the need arise. For each tested geometry, a single ‘meta-atom’ element was constructed and periodic boundary conditions were used to simulate an infinite array. Incident light was simulated as a time-harmonic $1\,\mathrm{V\,m^{-1}}$ electric field incident normal to the interface in the desired linear polarisation from a boundary approximately 1.2 wavelengths away from the surface, to separate it from the boundary for sampling transmitted power B which must be at least one wavelength from the surface to remove the contribution of near field effects. The reflectivity R of the various tested metamaterials was determined by integrating the time-averaged power P passing through boundary B. This was compared with the expected value for an unobstructed plane wave propagating through the incident medium, depending on the refractive index of that medium n and the area A of a single unit cell in the plane of the sample. R is given by

$$R = 1 - F \tag{3.5}$$

where F is the fractional absorbed power. The total power of the incident plane wave is calculated from the definition of the Poynting vector:

$$S = \frac{1}{\mu_0} E \times B \tag{3.6}$$

Where μ_0 is the magnetic permeability of free space. Taking the time average we obtain:

$$\langle S \rangle = \frac{1}{2\mu_0} |E||B| \tag{3.7}$$

and knowing that for a plane wave $|B| = |E|/c$ (c is the speed of light) and that the electric and magnetic fields are perpendicular:

$$\langle S \rangle = \frac{1}{2c\mu_0} E^2 \tag{3.8}$$

Accounting for the area of the sample A and the increase in transmitted power due to the refractive index n of the incident medium, the power input into the sample area P_{in} is then defined as:

$$P_{in} = \frac{An}{2c\mu_0} E^2 \tag{3.9}$$

Knowing that the electic field in the simulations is $1\,\mathrm{V\,m^{-1}}$ and the fractional absorbed power $F = P/P_{in}$, we can obtain the reflectivity of the metamaterial:

$$R = 1 - \frac{2c\mu_0 P}{An} \tag{3.10}$$

An analogous method was used when simulating 2D structures such as gratings. Where multiple simulations of similar geometries were required, COMSOL functions were called from scripts written in commercial scientific computing software MATLAB. This way multiple simulations could be specified in advance, run and presented together, greatly facilitating the process of testing and optimisation.

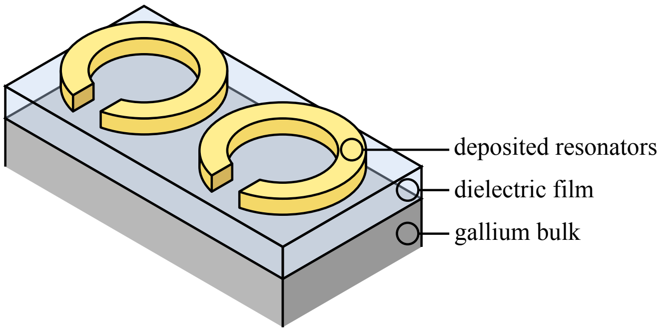

(a) Absorber-type geometry

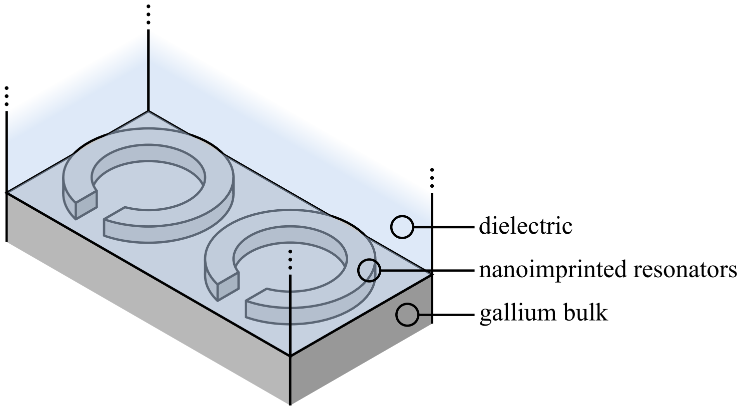

(b) Nanoimprint geometry

Figure 3.1: Practical metamaterial geometries incorporating gallium.

3.4 Manufacturing methods

Two main metamaterial geometries were chosen and developed, one involving the production of a structured gallium surface, the other a plane film, shown diagramatically in fig. 3.1.

Absorber geometry The trilayer absorber (fig. 3.1a) is a relatively well-understood and flexible class of metasurface that may be conveniently manufactured with gallium as a component. Maintaining a barrier between gallium and other metals to be structured allows both to be usefully harnassed without the possibility of gallium infiltrating and damaging the additional metal (see section 2.4). The gallium surface is also planar so the surface melt dynamics studied in the past remain unperturbed.

Structured gallium The preparation of structured gallium is more challenging. The metal would need to maintain its structure over multiple phase switching cycles. To achieve this, the primary method used is the application of a dielectric 'mould' to structure the liquid gallium surface and to maintain the mould's contact with the gallium during characterisation, so even the otherwise unstable liquid phase is tightly controlled. This type of manufacturing was previously deployed successfully on gallium to produce a shallow 30 nm grating of sub-micron period,[49] which forms a useful basis for investigation.

3.5 Gallium film deposition

Thin film deposition of pure gallium metal is not a routine operation and as such there is no standard process. To determine the most effective process for this task, several options were considered. All are ways to deposit films of varying thicknesses onto a prepared substrate. They are all additionally suitable to the application of gallium to a structured substrate in a ’nanoimprint’ type setup to varying degrees. These methods are as follows:

- Thermal evaporation. This standard method uses high temperatures (around 1000K) induced by either an electron beam or electrical resistance to evaporate a gallium sample onto the surface of interest, taking special precautions to protect the deposition system from gallium percolation. This method has the dual advantages of a high deposition rate relative to other thin film deposition techniques and relatively accessible requisite hardware. However, the resulting film quality is likely to be inferior to epitaxial processes.

- Ultrafast PLD(pulsed laser deposition). Femtosecond pulse lasers may be used to ablate and deposit gallium droplets on a surface in vacuum. This method has been employed successfully by researchers at the Australian National University in the past but is not currently accessible to this project as that collaboration has long since ended. Nanosecond pulse PLD equipment is available at the University of Southampton. Unfortunately, nanosecond PLD fails to correctly deposit gallium and that equipment is hence not of use here. Femtosecond (ultrafast) PLD, however, has the benefit of successful prior testing and has otherwise similar advantages and disadvantages to thermal evaporation.

- Droplet compression. This means simply the compression of a filtered liquid gallium droplet onto a cleaned substrate surface such that it spreads across to produce a high-quality interface. While this allows deposition at lower temperatures and is quick, simple and conveniently low-tech, it presents some disadvantages. Primarily, it is not possible to control the thickness of such a layer on the relevant scale (that of the optical skin depth). Additionally, adhesion and other film properties are highly dependent on both the atmospheric conditions under which the deposition is performed and the speed of droplet spread. The extent of wetting, relevant to nanoimprint deposition of gallium on structured surfaces, is also dependent on the level of oxidation of the gallium's surface. A sparse oxide layer is detremental to wetting, as is one that is very thick.[65]

- Molecular beam epitaxy. This industrial PVD process is in essence a more highly controlled implementation of thermal evaporation. This high quality CMOS (complementary metal oxide semiconductor) thin film deposition method appears to be as yet untested for gallium, but may produce highly repeatable results. Difficulties may arise because any such CMOS process must be run in collaboration with an external provider and would require specialist preparation and transport arrangements, a highly impractical proposition. In addition, the deposition rate is much slower than other thin film deposition methods such as thermal evaporation. Chamber contamination and damage by gallium grain boundary penetration is also more of a concern in such high-value equipment.

- Chemical vapour deposition. CVD is a chemical process involving the placement of a substrate in a gaseous medium containing a volatile precursor which disassociates at the substrate surface, hence depositing the intended compound. The primary benefit of this process is that it may function at lower temperatures than the other deposition methods listed here, changing and potentially improving the quality of the deposited film.

3.5.1 Chemical vapour deposition trials

CVD of gallium was tested in collaboration with my colleague Kevin Huang of the Soft Glass & Fibre Group, ORC, including deposition and characterisation of properties on silica and silicon. SEM imagery and an EDX (energy dispersive X-ray) spectrum for a sample deposited on silica may be seen in fig. 3.2, confirming the exclusive presence of the expected elements gallium, silicon and oxygen.

Spectrometry and spectrophotometry tests implied the film was an amalgam of gallium and gallium oxide (Ga_2O_3). This was the result of the thin pure gallium film reacting with oxygen after deposition due to contamination of the nitrogen supply with H_2O. Remedial action was taken against this by my colleagues over a long period, during which trials of other deposition methods continued, so this method was discontinued to focus on those. Further trials with thicker deposited films are required to gauge the effectiveness of this technique, but the results are tentatively positive and CVD could potentially be used for deposition of pure gallium.

3.5.2 Thermal evaporation trials

Trials of gallium deposition were run using a resistance evaporator available to the ORC. The method was tested on various dielectric substrates:

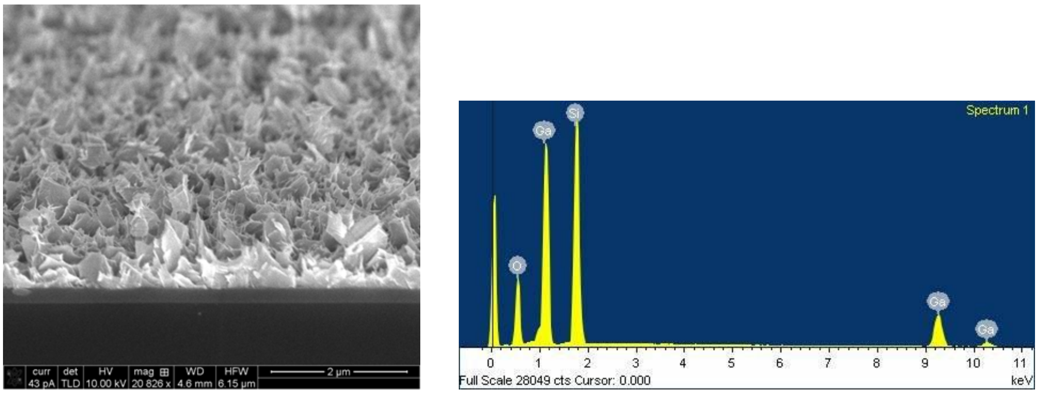

Figure 3.2: Left: SEM image of the CVD gallium polycrystalline film. The film was deposited on a 200nm-SiO_2-on-Si substrate; the silica and silicon are visible as light and dark bands at the edge of the sustrate. Right: Energy-dispersive X-ray spectroscopy measurement of the film. Results taken by Kevin Huang of the Soft Glass & Fibre Group, ORC.

- Borosilicate glass
- Fused quartz
- Sapphire
- Silicon nitride

Dielectrics specifically were used since both varieties of metamaterial to be tested contain a gallium-dielectric interface. The test was initially run on all substrates at a thickness of 440nm liquid gallium. In all cases interfaces were produced which displayed qualitatively correct reflective properties for a metallic mirror. Microscopy and spectroscopy analysis conducted through the dielectric substrates revealed the liquid gallium produced a discontinuous surface, as seen in fig. 3.3. The deposited film consisted of many separate microscale islands of liquid gallium (of diameter up to 5 microns). The spectral reflectivity was reduced relative to that of squeezed liquid gallium across a wide spectrum, consistent with a film consisting of a gallium bulk with low-index dielectric inclusions . It is therefore thought that the visible structure is the result of partial oxidation of the gallium, forming dielectric gallium oxide Ga_2O_3. This conclusion is arrived at based on the knowledge that glass-adhesion effects from gallium's oxide layer can persist up to considerable levels of vacuum[64] and the knowledge that noble metals, which deposit in the same Volmer-Weber mode and do not form oxide layer so readily, form continuous films at much lower deposited thicknesses. This hypothesis was later made stronger by SEM imaging; during deposition the gallium forms droplets which may press against one another and deform when they appear to be in mutual contact. An oxide layer preventing coalescence is the likely culprit. See section 7 for the relevant SEM imagery.

Thermal evaporation tests were run with thicknesses of approx. 600 nm and 1.2 and 2.4 µm. Analysis of these films under the microscope revealed that the

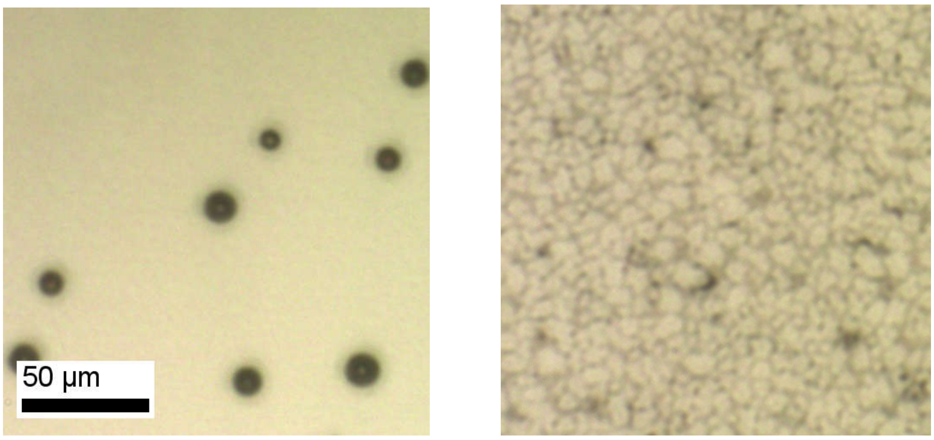

(a) ’Droplet compression’ liquid gallium mirror on borosilicate glass

(b) Deposited gallium mirror (600 nm) on borosilicate glass

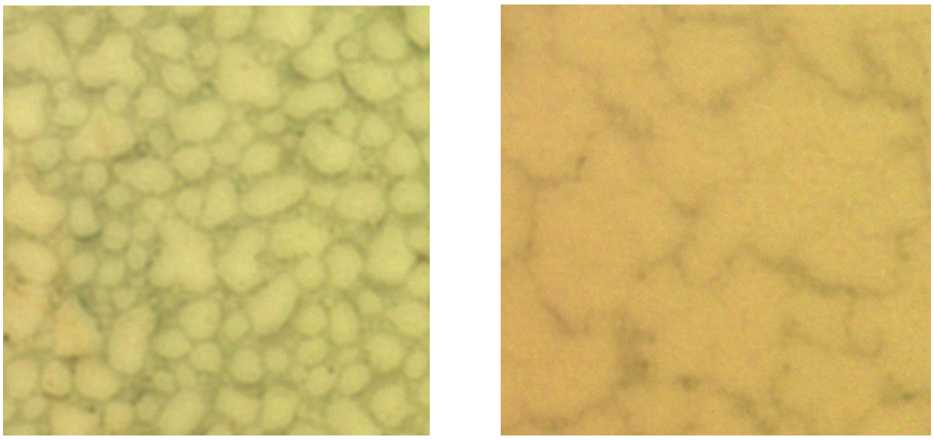

(c) Deposited gallium mirror (1.2 µm) on 200nm silicon nitride

(d) Deposited gallium mirror (2.4 µm) on borosilicate glass

Figure 3.3: Liquid gallium mirrors produced by (a) droplet compression application and (b-d) thermal evaporation. The images are reflection-domain, taken of the deposited films through borosilicate glass or silicon nitride using an optical microscope and CCD sensor. The visible ’dots’ in (a) are presumed to be microscopic trapped air bubbles. In (b) the film can be seen to consist of many islands of varying size and shape. The overall reflectivity of the sample is visibly reduced relative to (a); both images were taken at identical incident light intensity and imaging settings. (c) and (d) demonstrate the effect of deposited thickness on the size of the microscale ’islands’ formed by the gallium. All images are taken at the same magnification (with digital zoom applied close to the limit of the resolving power of the microscope).

characteristic size of the 'micro-islands' visible on the gallium surface is strongly dependent on the thickness of the deposition: see fig. 3.3. A 600 nm mass-thickness film deposited on silica contains islands of up to 10 microns across, while a 1.2 µm film contains islands up to around 30 µm across. A 2.4 µm film on glass appears semi-continuous in nature. Based on the small variations in contact angle of gallium against differing dielectrics[56] it was not expected that choice of dielecric substrate would significantly affect the quality of the resulting film.

Gallium has a well-known tendency to supercool (remain in liquid state below its freezing point) and this tendency increases for gallium that is confined to small areas and is very pure. Hence it was investigated to what extent this is the case for these discontinuous films of high purity gallium. The 1.2 µm sample was cooled (via use of a cryogenic control stage) to progressively low temperatures in order to ascertain the effect of the formation of islands on temperature of freezing. The gallium did not freeze on passing below 29.8 °C, its bulk freezing point. This was expected as a consequence of its supercooling tendency. The gallium partially froze at −30 °C with the freezing being confined to individual islands or groups, as observed through visible-spectrum changes in reflectivity in portions of the film. Minimal optical changes were observed down to a highly cryogenic temperature of −165 °C (108K), approaching the low-temperature limit of the cryogenic stage - see fig. 3.4. This implies that the film is semi-continuous in nature, since groups of neigbouring islands froze at the same time. Furthermore it implies that certain islands were sufficiently separated that they did not freeze even at extremely cryogenic temperatures. This observation is attributed to the very high purity of the gallium used in the deposition - 6N or 99.9999 %. Spectra were taken throughout the experiment, but a tendency for the film to 'wrinkle' upon freezing, attributed to the lower density of solid gallium relative to the liquid phase, made spectral acquisition unreliable and hence the spectra are not presented. An increase in this wrinkling is the only change observed below −30 °C.

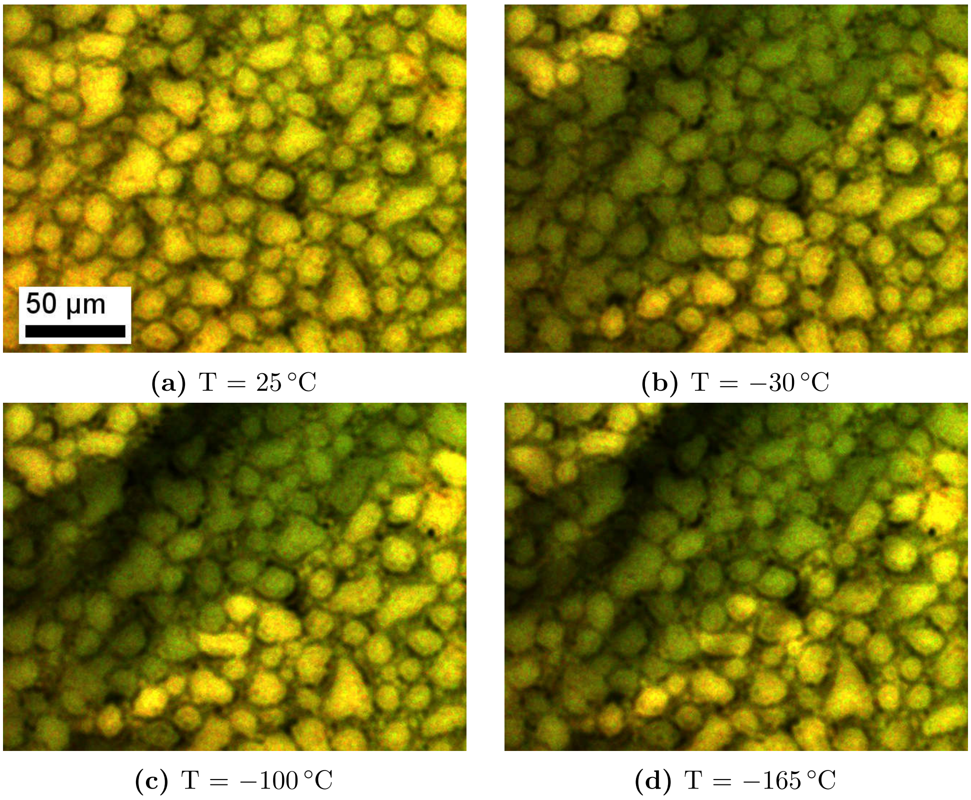

(a) T = 25 °C **(b)** T = −30 °C

(c) T = −100 °C **(d)** T = −165 °C

Figure 3.4: Partial freezing of a deposited liquid gallium mirror under a broad temperature range. Darker areas correspond to frozen gallium. The images are optical microscopy of a 1.2 µm gallium mirror under 50 nm silicon nitride membrane. The images are taken of the deposited films on the underside of the silicon nitride membrane in the reflection domain using a CCD sensor at differing temperatures T during cryogenic thermal cycling. The images are taken at the same position on the sample under the same lighting conditions and sensor settings and presented with enhanced contrast for viewing convenience.

3.6 Gallium-aluminium nanocomposite

As discussed in the opening chapters, liquid gallium may infiltrate into the bulk of other metals via the process of grain boundary penetration (GBP). This process was previously investigated in thin films where it was discovered that it becomes possible to thermally switch the optical properties of the film as viewed through the substrate. This composite may hence be used as a basis for nonlinear optics.[61] I hence undertook an experiment to recreate this observation with a more pure 6N sample of gallium.

3.6.1 Grain boundary penetration

For this experiment I chose to observe how and whether the GBP (infiltration) process proceeded in varying thicknesses of aluminium. Aluminium thicknesses of 20, 60, 100 and 250 nm were deposited onto silica slides by resistance evaporation. The samples were transferred to a nitrogen atmosphere glove box. One portion of the deposited area on each slide was prepared for infiltration by exposure of the surface to 0.1 molar potassium hydroxide solution in order to remove its oxide layer. After a 10 second exposure the surface was dried with a non-shedding wipe. An approx. 0.2 ml bead of room temperature overcooled liquid gallium was then applied to the exposed surface and contact between the film and bead was ensured by piercing the bead with a ceramic fibre cleaver and scratching the deposited surface under it. The subsequent evolution of the surface during infiltration was then observed by eye.

The applied gallium infiltrated into the aluminium thin films in all cases over the course of several hours, including the film of just 20 nm thickness, thin enough to be semi-transparent. Hence it seems likely that gallium is capable of infiltrating aluminium films of any thickness above the threshold required for a continuous film. The infiltration process caused the physical cohesion of the films to reduce significantly; the films became easily scratched by contact with soft materials and capable of delamination from the substrate.

3.6.2 Cryogenic microspectrophotometry

In order to recreate the thermal switching seen previously I chose a sample of gallium-aluminium nanocomposite produced by gallium infiltration of a 100 nm film of aluminium deposited on silica, using the process described above. Infiltration of the gallium into the aluminium was confirmed by visual inspection of the spread of discoloration during the process. Using a Linkam THMS350V vacuum cryo stage for thermal control, I took microspectrophotometric readings of the composite film at intervals beginning at 25 °C down to −150 °C and up to 60 °C, all under vacuum. The readings at the extremes of this range are given in fig. 3.5. The results appear in total contrast to those in the Krasavin et al experiment,.[61] In that experiment a

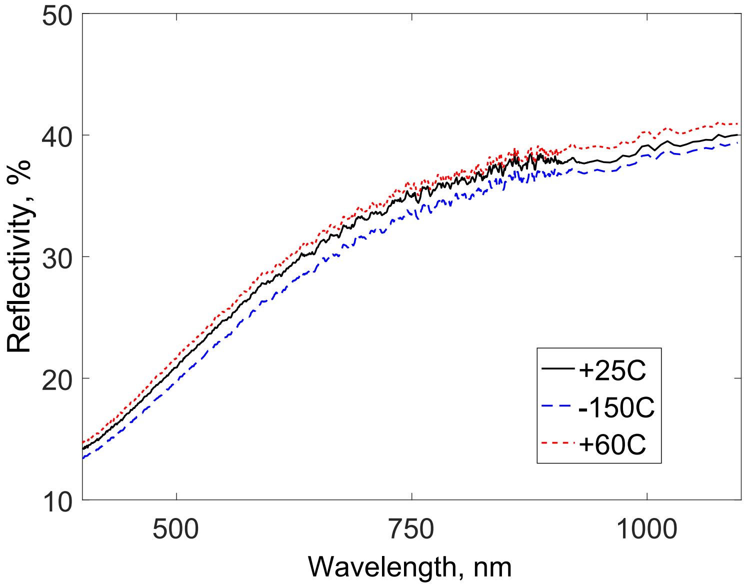

Figure 3.5: Variation of spectral reflectivity of 100 nm gallium-aluminium composite film with temperature.

reflectivity reduction of 40% was demonstrated on solidification at a wavelength of 550 nm. This solidification occurred at 3 °C below gallium's melting point. It is clear by comparison of the presented experimental spectra with this previous result that solidification did not occur at all, despite the much larger range tested. The small change in spectral reflectivity seen is very likely due to thermal drift of the stage (the microspectrophotometer needed to be refocussed prior to taking each reading) and deposition of any gases still present in the chamber onto the stage and sample area.

Due to this unexpected result I undertook to test much lower temperatures to find the level at which freezing actually occurs. To this end I harnessed a cyrogenic microspectrophotometry stage with a base temperature of approx. 7 K. I thermally cycled a newly prepared sample of 150 nm thickness up to 310 K and down to the minimum temperature of the stage, refocusing the microspectrophotometer before each reading was taken using the near infrared InGaAs sensor. I subsequently ran the same process again from room temperature to 125 K at a different area of the sample, to test the consistency of the results. The variation in spectral reflectivity during both experiments is presented in fig. 3.6. For ease of viewing the variation is presented at three different wavelengths. These particular wavelengths were chosen for their exhibition of greater variation with temperature.

From mutual comparison of the results of the two experiments it appears likely that the changes in reflectivity, which vary within around a 1% window, are not caused by changes in structural phase but instead due to thermal motion of the stage. This may be concluded both because the changes are small relative to the results by Krasavin et al and because they arise at different temperatures upon re-running the experiment.

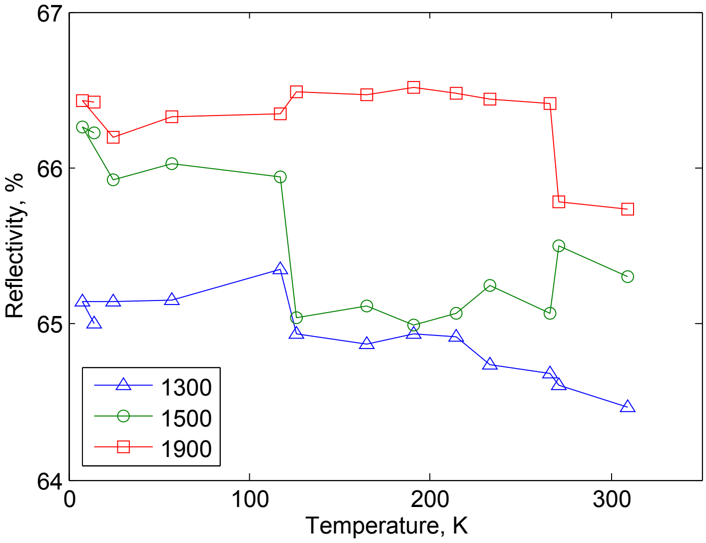

(a) Initial experiment

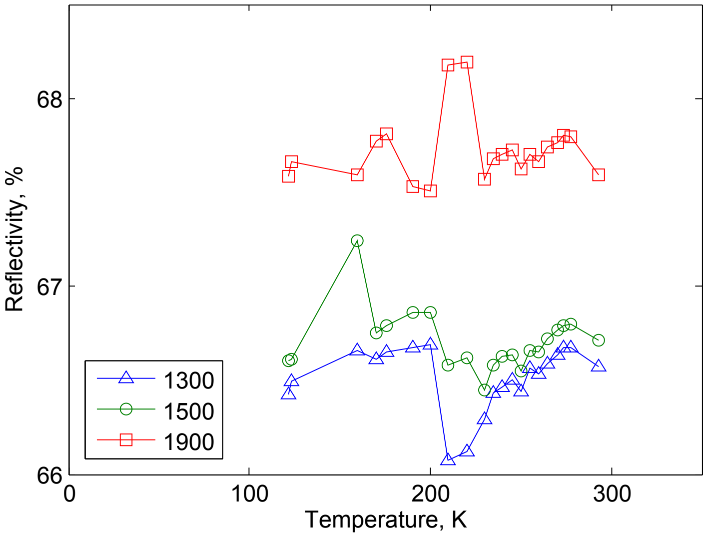

(b) Confirmation experiment

Figure 3.6: Variation of reflectivity of a 150 nm gallium-aluminium composite film with temperature at three target wavelengths.

Thus I must conclude that this sample of gallium/aluminium composite may be supercooled to an extraordinary degree, and it appears very likely that in these experimental conditions it is not energetically favourable for gallium to crystallise into the solid α phase at any temperature. This is not entirely unexpected given that gallium has previously been shown to display supercooling down to 150 K in an analogous experiment.[66] Had the experimental setup the capacity to cool below 7 K, we might have expected to see a change in reflectivity due to the superconducting transition, but as the setup was not quite sufficient for this, no significant change was seen down to the base temperature reached. The reason for this is likely threefold: first, the sample of gallium used was extremely pure, which naturally increases the capacity for supercooling. Secondly, it is well understood that nano-confined liquid gallium has a tendency to supercool to lower temperatures than a bulk sample. Gallium that has undergone GBP into another metal is necessarily highly confined, such that it may remain in between grain boundaries of that metal. Thirdly, infiltration into a very thin film will result in an extremely small volume of gallium being present. This further reduces the probability that sufficient impurities will be present in the gallium for solid phase crystals to nucleate, leading to the observed behaviour. This hypothesis stands for the time being, though further experiments are necessary to determine in what limits solidification may begin to occur.

As an aside it is worth noting that it was possible to initiate freezing in a GBP sample produced from a 250 nm aluminium film on silica. This was achieved by direct immersion of the sample in liquid nitrogen for a few seconds and immediately scratching it with a solid gallium crystal. Even this method was haphazard, however, and required multiple attempts.

3.7 Gallium-silicon nitride bilayer

Due to both its relative simplicity of manufacture and its consistency in thermal cycling, the ‘droplet compression’ method was chosen as the most promising candidate for the construction of a gallium-based metamaterial. In order to facilitate the production of a multilayer metamaterial in useful proximity to the gallium bulk using this method, a thin (< 200 nm) silicon nitride membrane, embedded in a window in a silicon wafer, was chosen as the surface onto which the gallium would be deposited - see fig. 3.7.

Before metamaterial manufacture, it is desirable to first test the viability of the technique. Hence an experimental test was performed of gallium droplet compression application onto low-stress silicon nitride membranes of varying thicknesses. The normal incidence reflectivity spectra of the resulting bilayer samples were then characterised. Finally, thermal cycling of the samples was conducted thorugh the use of a cryogenic thermal stage before obtaining new

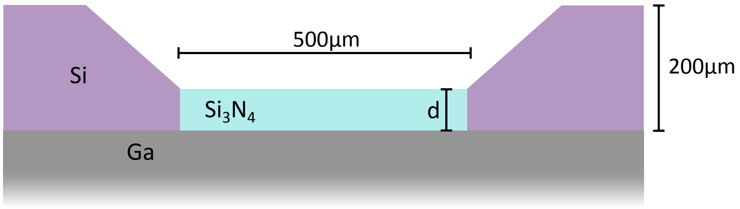

Figure 3.7: 'Gallium-silicon nitride bilayer' in cross section. Thickness 'd' of the membrane is varied between 50 nm and 200 nm for this experiment.

spectra for the solid phase. These results were then compared with predictions obtained using transfer-matrix method numerical modelling. The first bilayer tested (incorporating a 100 nm silicon nitride membrane) did not survive the freezing process due to sudden flash freezing of the gallium damaging the membrane. The experimental method was then adapted for subsequent testing of 50 and 200 nm thick membranes. Instead of freezing the squeezed liquid gallium while it was in contact with the membranes, pre-frozen sqeezed samples of gallium were prepared by pressing gallium droplets between silica slides and then freezing them using cryogenic nitrogen vapour. Contact between the membranes and the squeezed planes was then achieved by placing the membranes on top of the solid gallium and allowing the temperature to slowly rise above the melting point, at which point the transition to the liquid phase allows conformal contact with the membrane. The results for the 50 nm and 200 nm membranes are given in figs 3.8a and 3.8b respectively.

Several resonant dips may be seen, all characteristic of this type of simple planar setup. Such a planar system can introduce only metal-enhanced FP type interference resonances. For instance, given a refractive index of silicon nitride of close to 2 in the relevant optical range,[157] the 1600 nm dip in the 200 nm membrane case corresponds approximately to a $\lambda/4$ antireflection coating. It may be noted, in particular for the 50 nm membrane case, that the dispersion of the liquid phase reflectivity retains a short-wavelength dip more characteristic of the solid phase than is suggested by numerical modelling. This could be due to the presence of the membrane affecting atomic layering within the liquid gallium surface. As discussed in section 2.3.2, gallium's optical contrast upon melting may relate to layering of dimer molecules in proximity to the planar surface.[40] Physical contact with the silicon nitride membrane may disrupt this ordering to a degree, reducing the liquid's effective reflectivity relative to that in air. If this is so, it is possible this effect may be harnessed to actually improve the contrast by the application of an appropriate crystalline structure in the dielectric to optimise layering within the surface. Disruption of atomic ordering in the surface could also account for the smaller deviation from theoretical predictions that is seen in the solid phase case. To determine the extent of the effect of this disruption of ordering on optical properties, the optical constants of gallium under silicon nitride would need to be

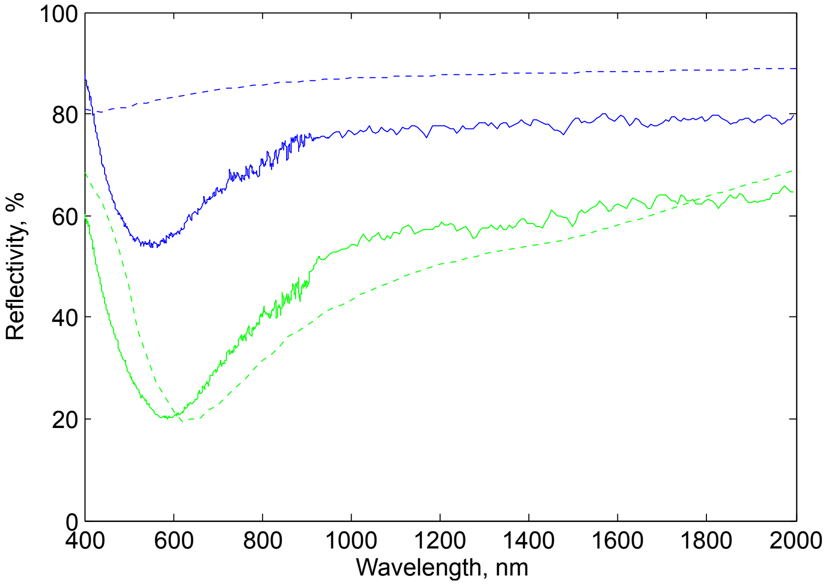

(a) Reflectivity for 50 nm silicon nitride membrane on gallium.

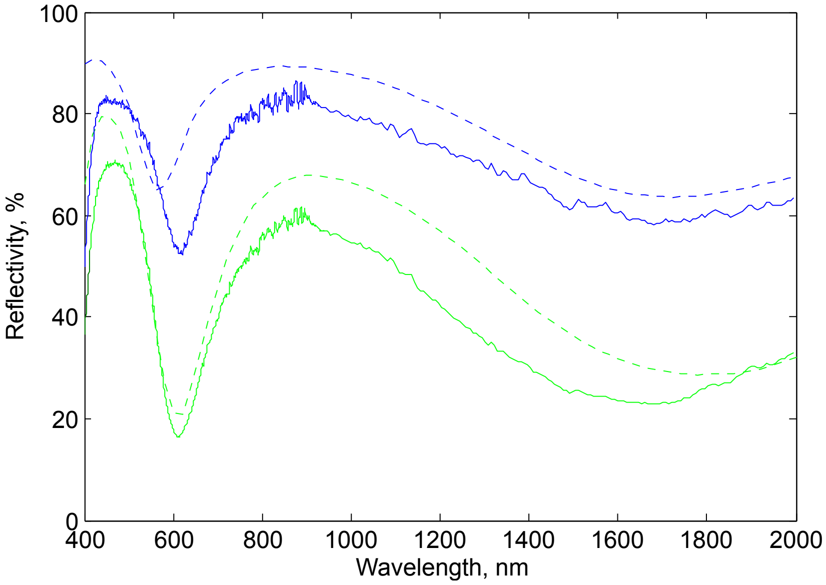

(b) Reflectivity for 200 nm silicon nitride membrane on gallium.

Figure 3.8: Optical switching of gallium under silicon nitride films under normally incident illumination. Solid lines are experimental data and dashed lines are predictions; blue, upper sets are for liquid phase and green, lower sets for solid phase gallium backplanes.

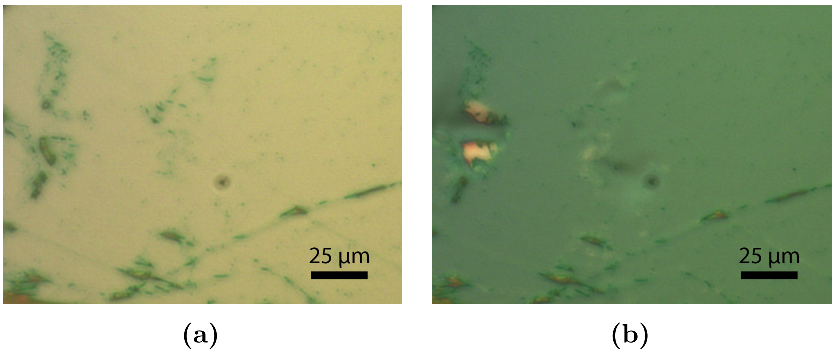

(a) (b)

Figure 3.9: Optical microscope images of liquid gallium compressed onto the underside of a 200nm-thick membrane of silicon nitride in (a) liquid and (b) polycrystalline solid thermodynamic phases.

investigated using ellipsometry. Unfortunately this was found to be impractical; due to the geometry of the samples (see fig. 3.7) the sample area was obscured by the silicon in which it was embedded for the purposes of the angled incidence necessary for this technique.

One of the more arresting results obtained during this portion of investigation is the discovery that for a membrane thickness of 200 nm, a very large visible-spectrum switching effect may be observed: from a bright, near-colourless mirror in liquid phase to dark green in solid phase. This is due to a large increase in absorption at the red extreme of the visible spectrum in the solid case and may be seen in fig. 3.9. Since the membrane has a thickness of 200 nm and a refractive index of close to 2 across the optical range, it effectively behaves as a $3\lambda/4$ antireflection coating within the visible spectrum, inducing the absorption resonance seen in fig. 3.8b and thereby enabling colour switching though variation in the depth of this resonance. Further resonances would be expected at higher frequencies ($5\lambda/4$, $7\lambda/4$ and so on).

3.8 Gallium-silicon nitride-gold absorber

To approach the construction of an absorber-type metamaterial, a numerical investigation into a planar multilayer absorber with gallium as the backplane was conducted. This simple absorber consisted of a silicon nitride membrane with liquid gallium pressed onto one side and a thin gold film deposited onto the other via thermal evaporation. The simulated thicknesses of the silicon nitride and gold films were varied in order to optimise the position and depth of FP absorption resonance. One such parameterisation test on a 200 nm membrane is shown in fig. 3.10. Two resonance peaks may be seen for the full breadth of gold thicknesses tested; one at approx 500 nm that varies primarily in depth and another that varies in spectral position from around 1700 to 1000 nm with increasing gold thickness. These are harmonics of FP resonant reflection[158] and both are present for zero thicknesses of

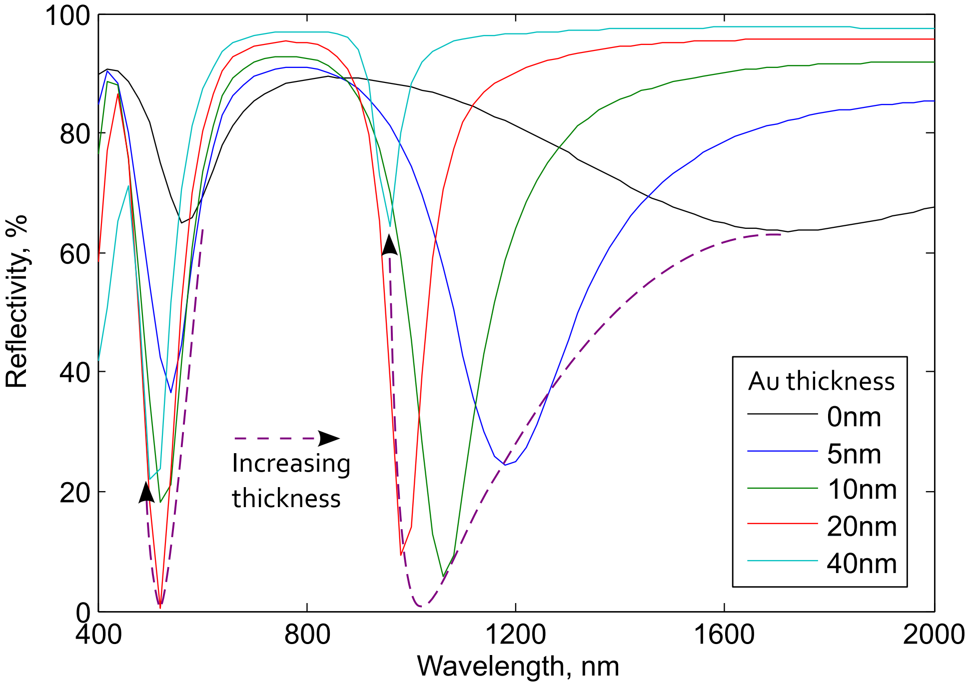

Figure 3.10: Numerically simulated normal incidence reflectivity spectra for a three layer structure of liquid gallium, 200 nm of Si_3N_4 and a thin gold film of varying thickness (as labelled). Motion and evolution of absorption resonances with changes in gold thickness are highlighted by the dashed line.

gold, but may be deepened to 'perfect' (total) absorption resonance by application of particular thicknesses of gold. The tendency of each resonance to vary greatly in depth for small variations in gold thickness implies that phase change switching of the gallium backplane may have an amplified effect on resonance depth in this case. From fig. 3.10 the optimal gold thickness for mazimising absorption would be between 10 and 20 nm. However it was found experimentally that gold films of thickness below 30 nm produced on our resistance evaporator had extremely poor film cohesion, which would lead to poor nanolithography results when the films were patterned at a later stage. Hence the miniumum practical thickness of 30 nm was chosen for experimentally tested films. Such gold/silicon nitride/gallium multilayers were tested numerically and experimentally and the results may be seen in fig. 3.11. Observe that the reflectivity contrast at the 1050 nm resonance is greatly magnified relative to the rest of the spectrum. In addition bulk gallium's reflectivity contrast in air is up to 40% at 650 nm, but in experiment this sample displays contrast of 85% at 1050 nm.

These results are promising, but only limited control of the nature of the resonances is possible by varying gold thickness. By introducing nanolithographic patterns to the surface much greater control may be afforded and this idea will form the basis of the next chapter on the development of a metamaterial trilayer absorber. Other investigated methods and findings observed in this chapter

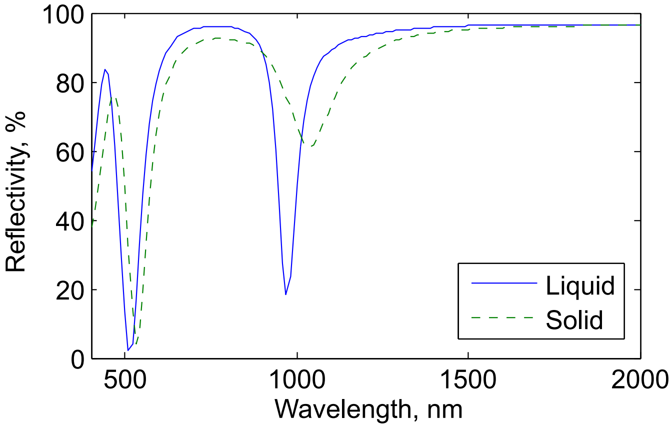

(a) Simulation

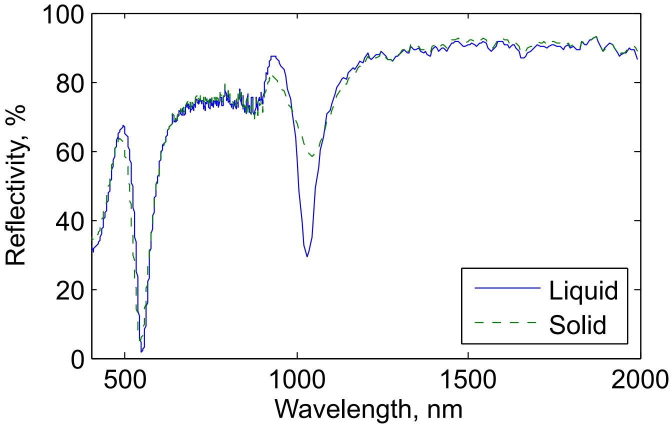

(b) Experiment

Figure 3.11: Simulated and experimental normal incidence reflectivity spectra for a planar trilayer absorber consisting of 30 nm gold on 200 nm silicon nitride on a gallium backplane. The spectra are changed significantly on thermal phase change switching of the backplane in both simulation and experiment, notably at the 1 µm resonance. Note also the $3\lambda/4$ thin film antireflection resonance at 550 nm.

underpin key components that and of subsequent experiments. The manufacture technique for gallium/silicon nitride/gold multilayers developed here is requisite to the experiments discussed in chapters 4 and 5 and the experiments with resistance evaporated gallium films described here led to the implementation of templated assembly of gallium nanoparticle films in chapter 7.

Chapter 4

Optically reconfigurable gallium phase change metamaterial absorber

Gallium's surface-mediated phase change nonlinearity can readily be harnessed and resonantly enhanced in a photonic metamaterial 'perfect absorber'. Such structures, realized over recent years at progressively higher frequencies from the microwave[159] to near-infrared[1,160] and visual domains,[161] generically comprise a planar array of sub-wavelength plasmonic metal resonators and a continuous metallic (mirror) backplane, separated by a thin dielectric spacer - the resonant absorption frequency being set by the relative permittivities of the constituent media, the geometry of the nanostructured metal layer and thickness of the spacer.[162] For clarity an example of such a metamaterial by Liu, Starr, et al.[163] may be seen in fig. 4.1 along with its absorption spectra, both simulated and experimental. The figure also gives the results of a simulation produced as a verification of the 3D FEM modelling techniques used in this work. Subtle deviation between simulations may be expected due to differences in meshing and the source of material data. In this case my simulation almost exactly matches the experimental results in the paper. Overall the comparison serves as a validation of the computational modelling methods to be used for gallium-based metamaterial absorbers.

Incorporating a gallium backplane mirror in place of a noble metal with static optical properties in such structures creates a mechanism for dynamically controlling the resonant response of the plasmonic metasurface with light and provides a platform for enhancement of the metal's optical nonlinearity.

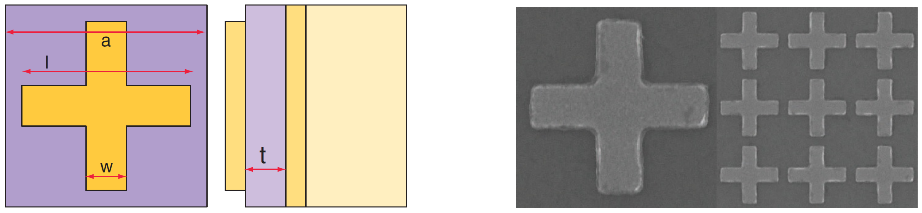

(a) Schematic

(b) SEM images

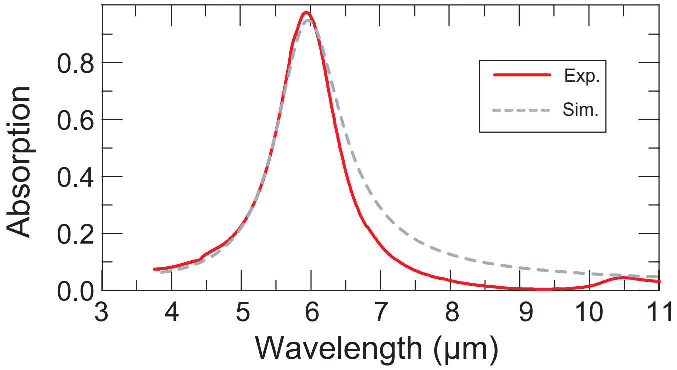

(c) Simulated and experimental absorptivity

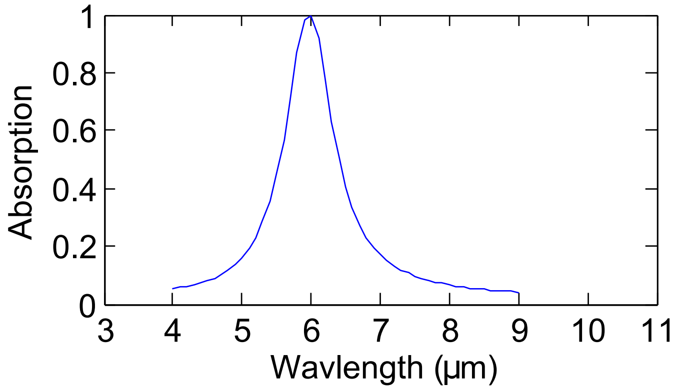

(d) Simulation for verification

Figure 4.1: Metamaterial infrared perfect absorber. (a): Schematic of the material from above and the side, dimensions a = 2, l = 1.7, w = 0.4, t = 0.185 in micrometres, both upper and lower Au films 100 nm thick. (b): Plan view SEM imagery of the same. The left SEM is at the same scale as the schematic. (c) Simulated and experimental results of experimental samples by Liu, Starr, et al showing a normal incidence absorptivity spectrum with Lorentzian-like resonance at 6 µm infrared wavelength.[163] (d) Simulated absorption spectrum for verification of simulation methods, in agreement with the paper's results.

4.1 Prototyping

In order to have a starting point for optimisation, the metamaterial design was based on Liu, Mesch, et al.,[1] but replacing the MgF_2 dielectric spacer with silicon nitride and the backplane with gallium, using the squeeze method developed as described in section 3 - see fig. 4.2. Two variations on this paradigm were developed, based on differing thicknesses of silicon nitride spacer.

- A disc design for perfect absorption and absorption resonance switching between 1.8 and 2 µm based on structural parameters silicon nitride membrane thickness m = 50 nm, gold thickness t = 20 nm, period s = 380 nm and diameter d = 255 nm. Numerically modelled and experimental results for this material may be seen in fig. 4.3b and c.
- A disc design for absorption resonance switching at 1 µm based on a 200 nm silicon nitride membrane and 20 nm gold film. The disc pattern was 380 nm in period and 255 nm in diameter. Simulated and experimental results for this material may be seen in fig. 4.3d and e.

These results emulate but do not precisely reproduce the ideal results of the simulations. For example, the resonance at 1050 nm for the 200 nm membrane metamaterial, while found to arise at the predicted position, was predicted to have a many-to-one contrast ratio, but the observed contrast is only around 20 %. In addition the 1650 nm resonance for the 50 nm membrane case displayed both inferior depth and inferior wavelength tuning than predicted. The discrepancies may be due to several issues, the foremost being:

- The original simulations produced prior to running the experiment were optimised for deep absorption resonances at 1610 nm (fig. 4.3a) and 1050 nm (fig. 4.3e). Hence any parameter variation will cause the real spectra to diverge from these optimised cases.
- Both optimised simulations use 20 nm gold films, while the deposited thickness in experiment is 30 nm, as previously discussed. This change is incorporated into simulation (f) of fig. 4.3.

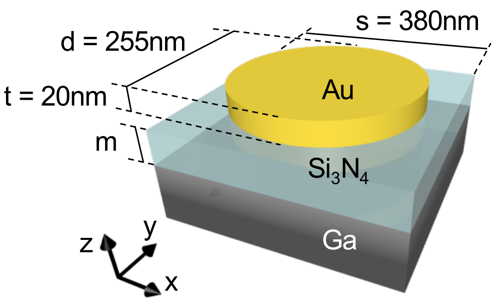

Figure 4.2: Disc absorber metamaterial schematic.

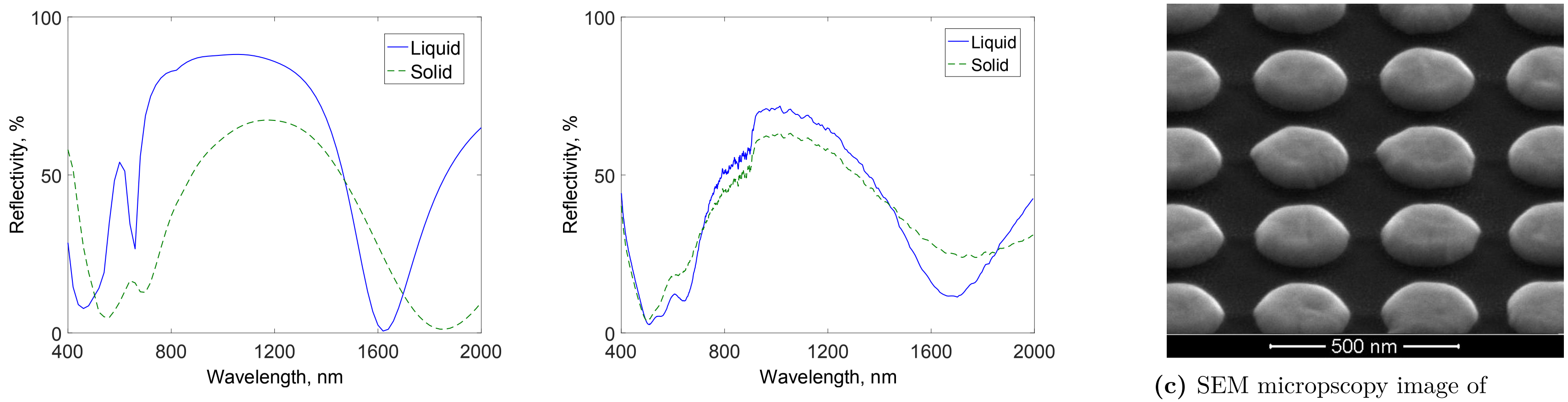

(a) Simulation, 50 nm membrane metamaterial **(b)** Experiment, 50 nm membrane metamaterial **(c)** SEM micropscopy image of manufactured metamaterial

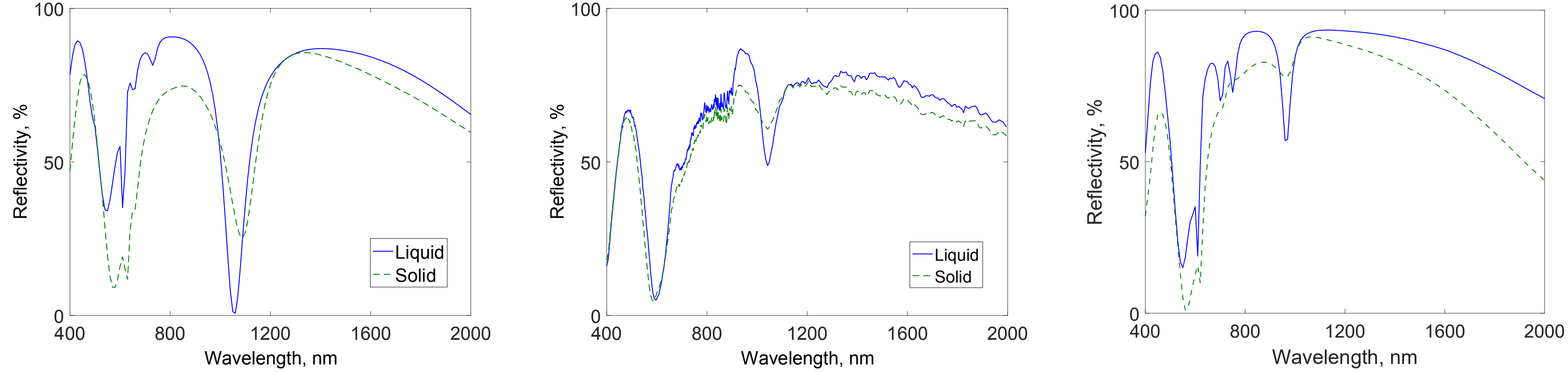

(d) Simulation, 200 nm membrane metamaterial **(e)** Experiment, 200 nm membrane metamaterial **(f)** Simulation, 200 nm, modified for accuracy

Figure 4.3: Experimentally characterised gallium-membrane-metamaterials: SEM imagery and simulated and experimental optical reflectivity spectra for normal incidence. Metamaterials are of the construction shown in fig. 4.2 with varying thicknesses of Si_3N_4. (a-c) correspond to a thickness of 50 nm and (d-f) to a thickness of 200 nm. Line colours correspond to solid and liquid phases of gallium. Simulations (a) and (d) are optimised predictions for maximum absorption and (f) introduces additional features increasing the accuracy of simulation, more accuratly predicting experiment. The simulations display the ideal case of thin (20 nm) gold films; the experimental results use thicker real films as discussed in section 4. The longer - wavelength (above 800 nm) absorption resonances were designed and may be tuned in wavelength. The origins of the resonances are discussed in section 4.2.

- There may have been a significant distance of surface melt into the bulk α phase in the experimental case of a solid backplane. This change is introduced into simulation (f) of fig. 4.3 by the addition of a 5 nm thickness of liquid phase gallium at the surface of the bulk.
- There may have been significant extra losses due to either or both of surface oxidation of the gallium and gallium ion implantation into the gold and silicon nitride during FIB patterning. These may explain the reduction in overall reflectivity seen in experiment (figs 4.3b and 4.3e) relative to simulations (figs 4.3a and 4.3d). Unfortunately insufficient data is available to accurately simulate the effect these issues would have.

Taking into account only the real deposited thickness of gold and an expected 5 nm surface melt in simulation as seen in fig. 4.3f, we see much better agreement with experiment.

Based on the results in fig. 4.3 and the knowledge of a minimum practical gold thickness of 30 nm (due to manufacturing issues at thicknesses lower than this as discussed in section 3.7), a gold thickness of 30 nm, a silicon nitride thickness of 50 nm, a disc diameter of around 250 nm and a periodicity of around 380 nm were chosen for subsequent study. Variation of these parameters became the basis of optimisation for the pump-probe experiment described in section 4.3.

4.2 Resonances

Simulations highlight the existence of absorption resonances in the optical region, which also appear in experimental data. Here, through the use of simulated maps of physical fields, I will discuss and identify the type of the resonances in question. In a particular variation on the structural parameters of the metamaterial (period = 380 nm, disc diameter = 255 nm, disc thickness = 20 nm, silicon nitride depth = 50 nm) four resonances may be identified as seen in fig. 4.4:

- 1600 nm absorption resonance. This arises through coupling of a localised surface plasmon resonant mode (LSPR) within the gold disc with the gallium surface. This LSPR is the fundamental mode of a surface plasmon standing wave on the disc, with antinodes at the centre and either end of the disc and a surface plasmon wavelength of approx. 275 nm. Fig. 4.4e is a local charge density map of the metallic surfaces for this resonance.
- 650nm absorption resonance. This is the first harmonic of the LSPR mode previously identified, as may be identified from the electric field maps of each (compare figures 4.4b and 4.4c) with a total of five standing wave antinodes across the diameter of the disc.
- Absorption resonances at 450 nm and 530 nm. These are simple FP-type multiple reflection resonances, with a much lower level of coupling to the disc,

as evidenced by the reduced levels of field confinement in fig. 4.4d. The field maps of the two are near-identical, with subtle differences in the excited mode on the disc visible in the surface charge density distribution. At up to two orders of magnitude smaller than that seen in the LSPR harmonics, the surface charge density maxima are insignificant and hence the mode is FP-dominant.

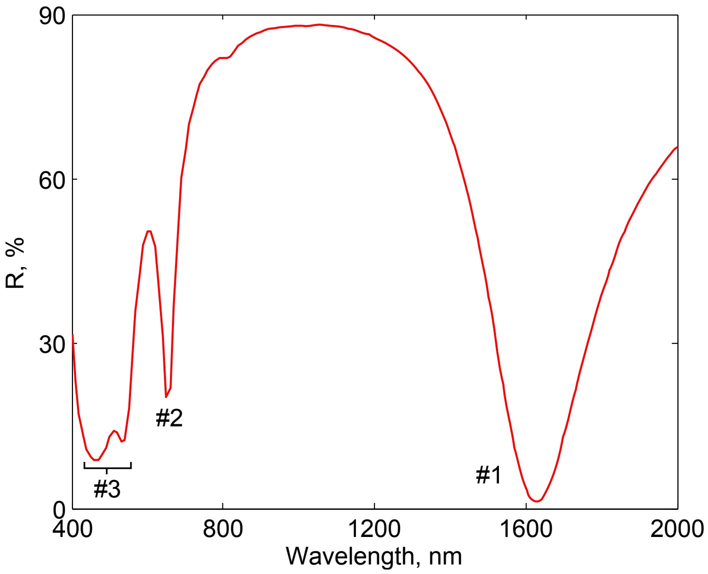

(a) Reflectivity spectrum.

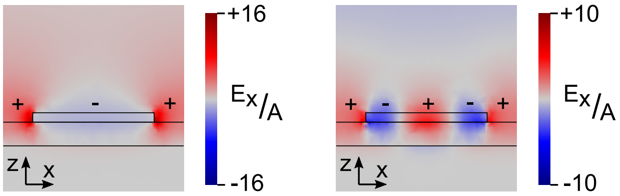

(b) Electric field map for resonance #1.

(c) Electric field map for resonance #2.

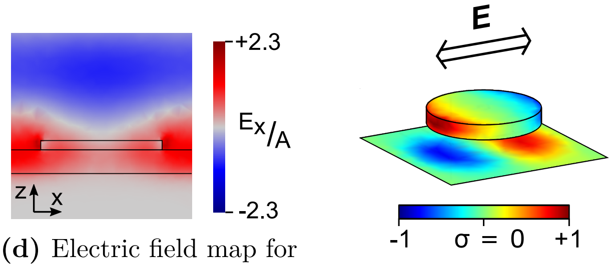

(d) Electric field map for resonance #3 (higher frequency component).

(e) Surface charge density map for resonance #1.

Figure 4.4: Simulation detail. Simulation method is as described in section 3, with x-polarised incident wave propagating along -z. All electric field maps are for the x component of the field $\mathbf{E_x}$ relative to the incident field amplitude $\mathbf{A}$. Each is an x-z cross section across the disc centre and obtained at the phase of maximum field localisation. A single electric field map is given for the dual resonances (#3) as the maps of the two are almost identical. Structure parameters: period = 380 nm, disc diameter = 255 nm, disc thickness = 20 nm, silicon nitride depth = 50 nm.

4.3 Near Infrared Pump-Probe Experiment

Following the work on understanding and optimising for various wavelengths, a near infrared pump-probe experiment was chosen for the investigation of the enhancement of nonlinear properties introduced by the metamaterial.

4.3.1 Design

A long-pulse pump-probe experiment operates on a simple principle: a high-intensity pump laser is used to excite a response from an experimental sample and a low-intensity probe laser is used to monitor changes in the surface without itself inducing a response. To facilitate the design of a practical experiment a series of requirements were taken into account:

- A sample design is required that provides a resonant response compatible with pump and probe wavelengths within the 400 nm to 2 µm range.
- The periodicity of the metamaterial array must be significantly smaller than the laser wavelengths, while being sufficiently large to be manufactured within reasonable tolerance. The latter requirement produces a minimum periodicity of around 200-300 nm.
- The pump wavelength should be targeted for maximum absorptivity ($A = 1 - R$, R being reflectivity) at high surface melt thickness and the probe for maximum change in reflectivity with surface melt thickness. Referring to modelling (fig. 4.3a) there should be a resonant absorption peak at a certain wavelength for a liquid backplane and a maximum in reflectivity contrast at a somewhat longer wavelength due to a blue shift brought on by the phase change.

Taking these constraints into account, readily available telecom laser wavelengths of 1310 nm (pump) and 1550 nm (probe) were chosen and the reflectivity spectra of a simulated metamaterial were optimised for absorption and reflectivity contrast ($C = (R_{max} - R_{min})/R_{min}$) at these respective wavelengths. An array of metasurfaces with variations on the simulated structural parameters were manufactured, varying period (s) through 340, 380 and 420 nm and diameter (d) through 205, 215, 240 and 265 nm. These were inspected via microspectrophotometry and one with optimal characteristics was chosen (see fig. 4.5).

The reflectivity of the metamaterial was simulated in the manner described in section 3 using the material data given in appendix A - see fig. 4.6. Let us first consider the variation between theory and experiment for a liquid phase gallium backplane. There is good quantitative agreement in both depth and spectral position of the resonance. None of the parameters of the theoretical prediction were varied to fit the experimental data; instead the structural parameters were obtained

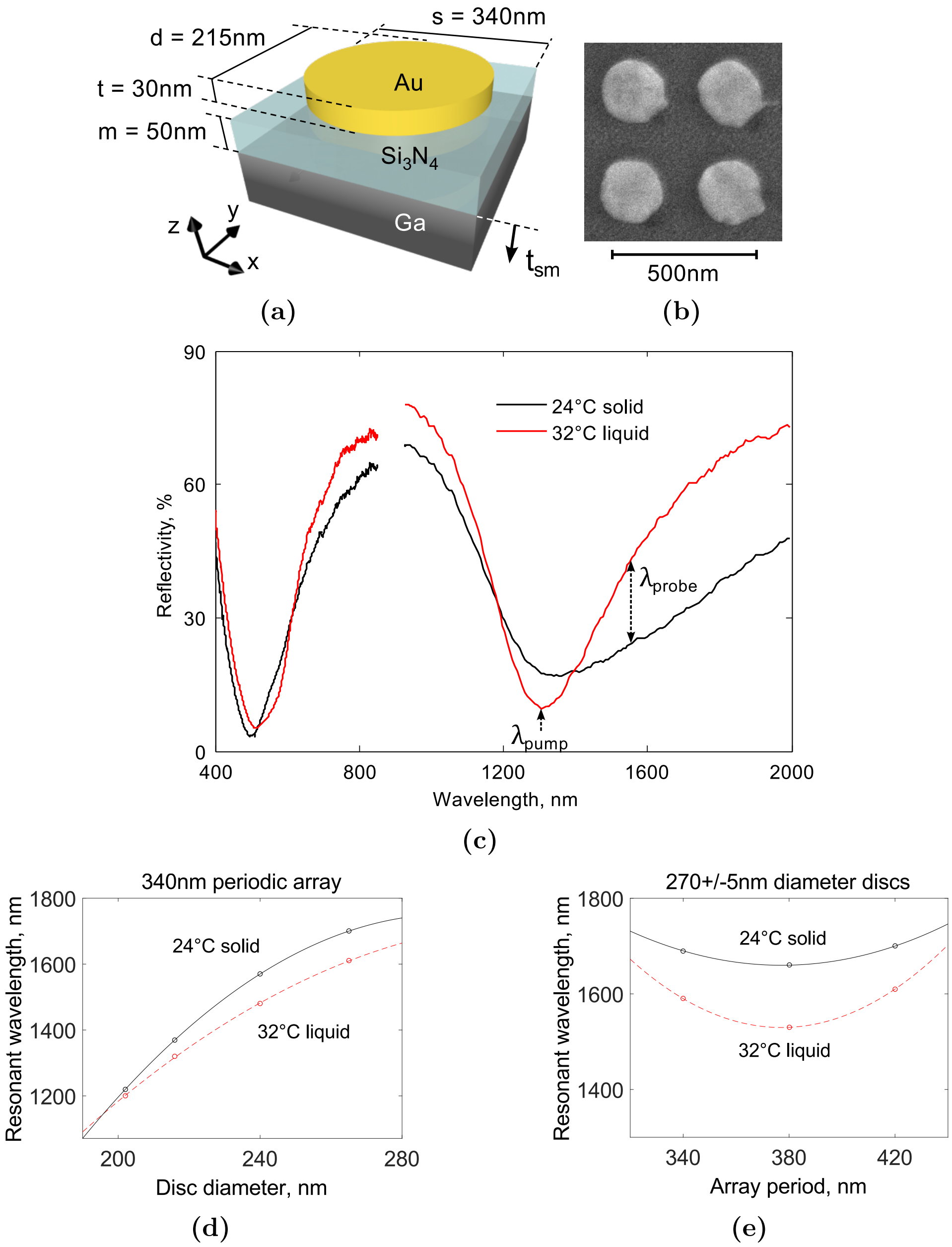

Figure 4.5: (a) Schematic and dimensions of the metamaterial. (b) Plan-view SEM image of 4 unit cells of the material. (c) Microspectrophotometry reflectivity spectra for the given parameters. (d) and (e): Experimentally observed dependence of absorption resonance wavelength on gold nano-disc diameter and array period respectively. The lines are quadratic fits and included as a guide to the eye only. Other dimensions are as given in (a).

from the known deposited thickness of gold and measurement of the mean disc diameters in SEM. In this circumstance the agreement is very good.

There is a small blue shift observed in experiment. This may be due to the approximation of the disc as a perfect cylinder in simulation, while the real structure has rounded edges. This would reduce the effective length of the disc along its surface, thus reducing the wavelength of the LSPR that propagates around it. Outside of the resonance, the maximum level of reflectivity obtained in experiment is somewhat smaller than simulation. Here there are two contributing factors. FIB nanolithography deposits gallium ions within the materials being patterned (in this case gold and silicon nitride) which is known to increase optical losses. In addition, the presence of the silicon nitride in contact with the liquid gallium may disrupt atomic layering within the surface, somewhat reducing the very high reflectivity understood to be produced by such layering. Disruption of atomic order in the gallium may also account for the *increase* in reflectivity seen in the solid phase in experiment relative to simulation, thus causing the low-reflectivity α phase to behave more like the liquid. This may also explain the considerable deviation in spectral position of the solid phase resonance relative to the simulation; the actual position of the resonance is much closer to the liquid phase resonance than expected, which is again consistent with the hypothesis that disruption in atomic ordering causes the crystal to behave more like the liquid. Combined with the fact that no fitting of theoretical parameters was done and the expectation that rounding of the edges of the disc would blue shift the resonance, an explanation for the considerable spectral shift between experiment and simulation emerges. The solid phase graph in simulation should hence be considered a limiting case in the total absence of any surface disorder / melt.

Prior studies have inferred a preferred orientation for the orthorhombic gallium crystal at a silica interface,[41, 42, 164] however, in the present case modelling shows that variations in crystal orientation are almost inconsequential to the spectral position or magnitude of the metasurface absorption resonance - see fig. 4.7. Due to this and the indeterminate preferred crystalline orientation against silicon nitride (as opposed to the previous experiments with glass), the solid phase is here represented via a simple ‘polycrystalline’ numerical average over the complex refractive indices for the three primary axes of α-gallium.

4.3.2 Method

The metasurface sample was mounted in a low pressure thermostatic stage (Linkam THMS350V) at the focal plane of an inverted microscope (Nikon AR1+) - see fig. 4.8. A reflective condenser was used to minimise focal issues with the use of differing laser wavelengths. Sample temperature T was controlled and calibrated against the bulk melting point of gallium $T_m = 29.8$°C. Both lasers were ThorLabs ‘butterfly’ configuration single mode fibre-integrated diode lasers, with their respective beams

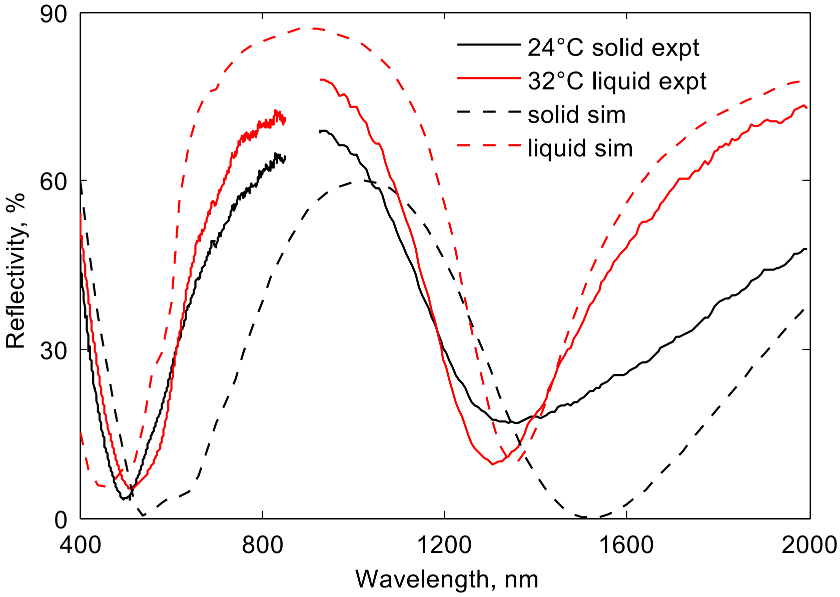

Figure 4.6: Experimental and numerically simulated reflectivity spectra for the gallium-backplane/Si_3N_4/gold-disc metasurface absorber tested in the pump-probe experiment, for the solid [sample temperature $T = 23.5°C$] and liquid [$T = 31.5°C$] phase states of the gallium.

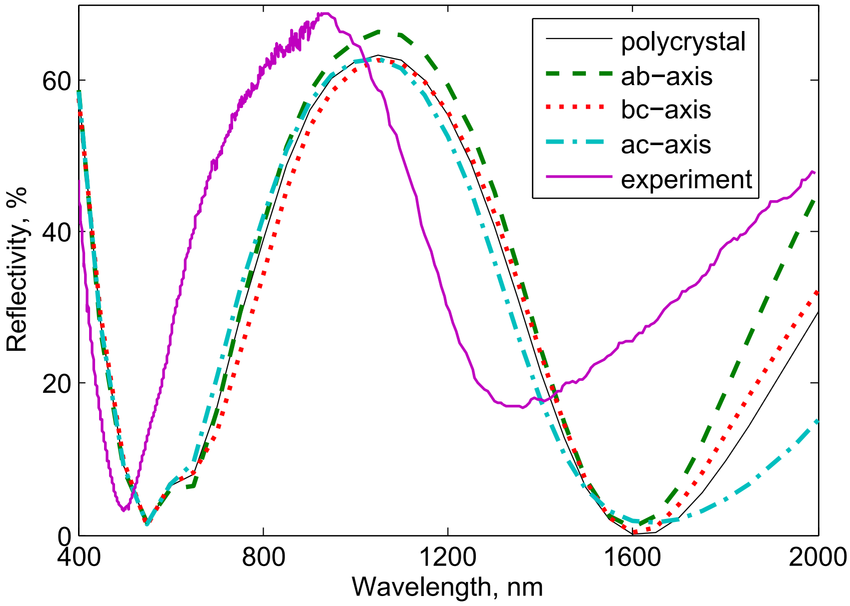

Figure 4.7: Numerically calculated reflectivity spectra for the experimentally characterised metasurface with differing gallium backplane crystalline orientations, alongside the experimentally determined reflectivity. The axes 'ab', 'bc' and 'ac' are chosen on the assumption that a third axis (generally the c-axis[164]) is considered more likely to align perpendicular to the interface. The real alignment relative to the metamaterial is indeterminate and possibly polycrystalline and hence numerical averages of the refractive indices of the two surface-aligned axes are used.

coupled into a free space beamsplitter before entering the microscope.

The two input beams were focused to concentric spots with Gaussian intensity FWHM dimensions of 15.7 µm for the 1310 nm pump and 6.6 µm for the 1550 nm probe, as determined by focusing onto an InGaAs CCD sensor at low intensity and comparing the gaussian beam distribution with known pixel dimensions. The sample location was determined with precision by switching the microscope input to a lamp with which the sample area could be imaged on the CCD. The lamp was then deactivated and CCD protected from the lasers via a shutter. The output probe beam was focussed onto a high-speed InGaAs photodetector, the signal from which was output to a digital oscilloscope. The beam intensities were determined using known beam power determined by a free space power meter in tandem with the known gaussian beamspot dimesions, at the peak of the gaussian distribution. The pump intensity was controlled by coupling its laser driver to the voltage output of a MHz signal generator.

For the duration of the experiment the probe was maintained at a fixed continuous wave (CW) intensity of 1.0 µW μm^{-2}, optimising signal-to-noise ratio while minimising direct heating by the probe laser. The pump was modulated at 500 Hz with 25% duty cycle (rise/fall times <1 µs confirmed by directly illuminating the photodetector with the pump laser) at peak intensities up to 16.8 µW μm^{-2}. This maximum intensity was determined by the limited output power of the available 1310 nm pump laser. After an initial experiment the pump periodicity and duty cycle were selected for optimal data display such that the pulse duration is somewhat larger than the rise time of the reflectivity and the delay between pulses is similarly longer than the relaxation time - refer to fig. 4.9 for an illustration of this.

For a selection of fixed pump peak intensities, the time dynamics of the metasurface's nonlinear 1550 nm reflective response were recorded while ramping the sample temperature, at a rate of 0.5 °C $\min^{-1}$, from 0 to 32°C.

4.3.3 Results

The reflectivity dynamics at a pump intensity of 9.5 µW μm^{-2} may be seen in fig. 4.9a. Under pump illumination the nanoscale layer of metallic gallium at the metal's interface with silicon nitride grows to an effective thickness t_s that increases with light intensity and with the proximity of sample temperature T to gallium's bulk melting temperature T_m.[41,42] The metasurface reflectivity increases as a result, towards a maximum intensity-dependent saturation level equal to its bulk liquid gallium backplane reflectivity level (a relative change of over 50% [Fig. 4.9b]), which is achieved when the excitation-enhanced surface melt layer becomes optically thick (the skin depth of liquid gallium at 1550 nm being ∼19 nm). At lower intensities and sample temperatures the induced reflectivity change accumulates throughout the 500 µs duration of the pump pulse as the illuminated

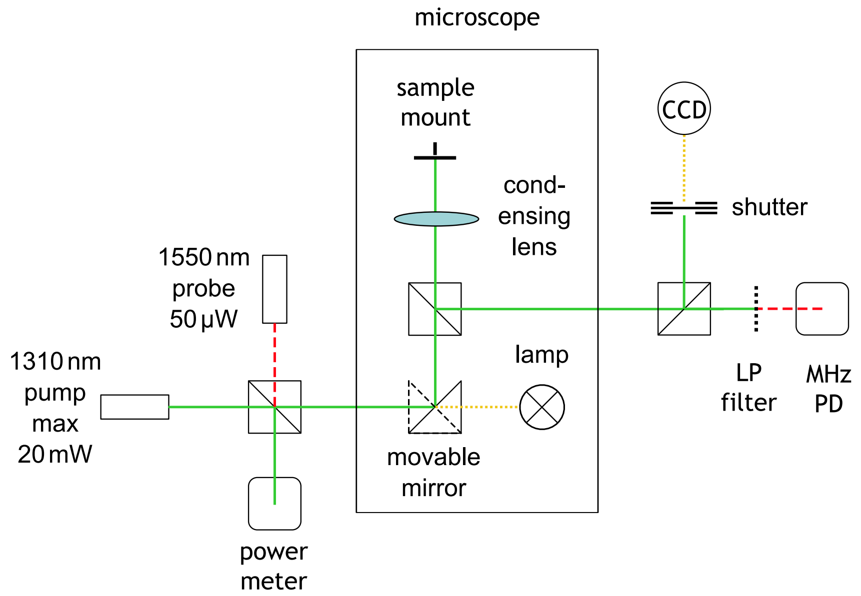

Figure 4.8: Experimental setup diagram. LP = long pass, PD = photodetector, CCD = InGaAs imaging sensor. The symbol ⍁ denotes a NIR beam splitter.

sample area moves towards an equilibrium state balancing the effects of light-induced heating within the skin depth of gallium, and heating via absorption in the gold disc array against the conductive removal of heat from the skin layer into the gallium bulk. At higher intensities and temperatures close to T_m, the surface metallization observable as a change in 1550 nm reflectivity proceeds more rapidly and the reflectivity level saturates within the pump pulse duration. Relaxation time, defined as the interval between withdrawal of the pump excitation and recovery of the photoinduced reflectivity change to below $1/e$ of its maximum value, as the metallized surface layer of gallium reverts to the α-phase, increases critically towards T_m as shown in the inset to Fig. 4.9b.

The phase transition-mediated nonlinear dependence of gallium metasurface reflectivity on incident light intensity cannot be quantified in terms of a conventional $\chi^{(3)}$ nonlinear susceptibility value (as discussed in section 2.6), nor indeed can one readily be approximated on the basis of the induced change in the metal's relative permittivity. However, a meaningful figure of merit γ may be obtained by considering the induced change in reflectivity per unit of illumination intensity:

$$\gamma = \frac{dR/R_0}{dI} \tag{4.1}$$

where R_0 and R are the probe wavelength reflectivities at pump illumination intensity levels of zero and I respectively. The value of γ across the tested range of temperatures and laser intensities may be seen in fig. 4.10 for the metamaterial as well as the silicon nitride/gallium bilayer. Results are presented for the bilayer at the maximum intensity only as obtaining detectable reflectivity switching in the 0.5 ms experimental timeframe proved challenging at intensities significantly lower

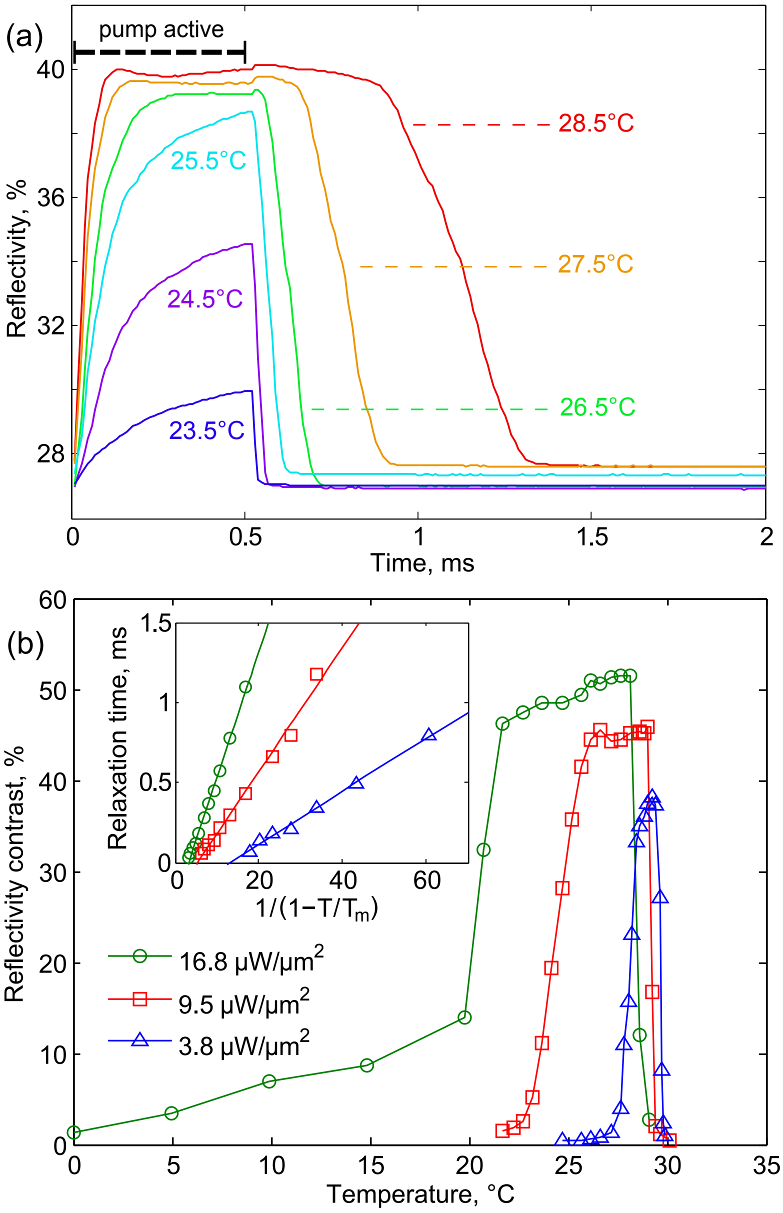

Figure 4.9: (a) Absolute 1550 nm reflectivity of the gallium metasurface as a function of time during and after excitation with a 500 µs, 9.5 µW µm^{-2} pump pulse at 1310 nm, for a selection of sample temperatures (as labelled) approaching the metal's bulk melting point. [Pump modulation frequency 500 Hz; traces averaged over 32 cycles.] (b) Maximum induced 1550 nm reflectivity change for a selection of 1310 nm pump intensities (as labelled) as a function of sample temperature. The inset shows reflectivity relaxation time as a function of temperature and pump intensity.

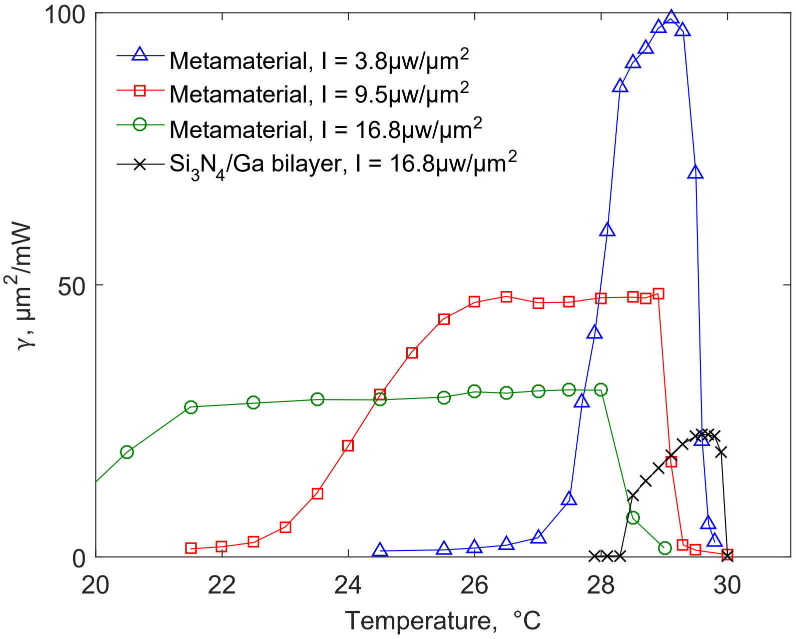

Figure 4.10: Enhancement of nonlinear figure of merit γ and functional temperature range of the metamaterial relative to a 50 nm membrane on gallium.

than this. This graph clearly expresses the enhancement of both the value of the nonlinear figure of merit γ and the temperature range over which nonlinear effects arise. γ reaches a peak value of 99 µm^2 mW^{-1} (a relative reflectivity change of 38% at an incident intensity of 3.8 µW µm^{-2}) for the gallium metasurface at a temperature of 28.8 °C, 1 °C below T_m. This should be compared with values of 17 µm^2 mW^{-1} for a simple planar mirror interface between gallium and a 50 nm silicon nitride membrane (obtained as part of the present study) and a value of 24 µm^2 mW^{-1} for a planar gallium/silica interface at a wavelength of 810 nm,[41] both again evaluated at $T = 28.8\,°\mathrm{C}$, $T_m - 1$.

It is also instructive to compare the temperature range at which significant photonic switching is observed for the membrane only sample with that for the complete metamaterial. The separation ΔT between the minimum temperature at which significant (> 50% of maximum) switching is observed and the observed bulk melting point is considerably enhanced by the metamaterial as compared to the 50 nm silicon nitride/gallium case. For the largest 16.8 µW µm^{-2} intensity case this value is increased from 1.5 K for the membrane to 9.5 K for the complete metamaterial. Hence the metamaterial enables switching at much lower temperatures. The reasons for this enhancement are explored in chapter 5.

4.4 Conclusions

The essential contribution of this work is in the development and successful deployment of an optically switchable photonic metasurface based on the phase switching of gallium. The primary aim was to use metamaterial technology to improve the nonlinear characteristics of the gallium surface melting phenomenon, but even in the absence of optical excitation, the metamaterial behaves as a self-adaptive absorber with a reversible, hysteretic response to changes in ambient thermal conditions. The developed metamaterial delivered a considerable improvement in the effective nonlinear response of the surface, as demonstrated by the $>50\%$ change in 1550 nm reflectivity under $<20\,\mu\mathrm{W}\,\mu\mathrm{m}^{-2}$ illumination at 1310 nm and significant nonlinear reflectivity up to 9.5 °C below the melting point. The metamaterial-enhanced gallium surface displays a nonlinear figure of merit γ (developed in this chapter) over fourfold higher than the case of an experimental test of a silicon nitride/gallium bilayer structure similar to the metamaterial, which displayed significant nonlinear properties only 1.5 °C below the melting point at the same intensity. The enhancement of these properties is expected to be greater still relative to an elemental gallium surface. These results must however be considered with the caveat that the experiment was conducted using a single metasurface sample, so repeatability has not been thoroughly tested. I will clarify that the pulsed experiment was repeated cyclically at 500 Hz over the course of several days, so repeatability with the sample that was tested is not in question.

The methods used are viable on surfaces up to scales of a few hundred microns but if larger-scale metamaterials are desired, due to the inherent difficulty of scaling the nanolithographic techniques used other methods must be harnessed instead. One possibility is the use of a similar lithographic technique to that seen in the work of Valentine,[165] which may enable the same type of structures to be manufactured on a larger scale. This highly scalable technique sees the natural hexagonal ordering of polystyrene nanospheres at a liquid interface used as a basis for the patterning of a regular disc structure in a metamaterial. By implementing this process in combination with a multilayer including a thick gallium film it is possible to construct this form of metamaterial on a large scale. Such metamaterials could find application in sensors, saturable absorbers or reflective spatial light modulators operated on a light-by-light control basis.

Chapter 5

Modelling gallium phase change dynamics

For the end goal of a full description of the physics behind the metamaterials developed in this work, an understanding of the physics of surface melting of gallium is required. Unfortunately no complete microscopic description of the surface melting phenomenon in the context of this or any other metal, or even of ice, exists, but rather phenomenological models which are a useful heuristic in the absence of an *a priori* understanding. This section summarises the available models and covers methods to extend the known theory.

A theoretical understanding of premelting necessarily includes an understanding of the melting of the bulk. Bulk melting cannot be understood exclusively by looking at the properties of each phase individually as the process of melting is inextricably tied up with the unique properties of the interface; the thermodynamic requirements for melting within a bulk are very different and rarely encountered.

Bulk melting is traditionally understood using the classical theories of phase transitions in the first and second order. First order phase transitions, of which gallium's melting transition is one, are characterised by a latent heat and described as arising at a precise temperature. They are named 'first order' as there is a discontinuity in the free energy of the medium in the first derivative with respect to the thermodynamic variable being changed. This first derivative is otherwise known as the 'order parameter' and is understood to correspond to the symmetry of the system, with a value of zero corresponding to completely broken symmetry. Many phase transitions are 'second order' under the same naming scheme and these are understood using what is commonly known as Landau theory. Landau theory is based on the idea that the free energy may be expanded using a power law in the order parameter.[166] While this is not mathematically completely sound in the case of a first order phase transition such as the melting of a metal, Landau theory has nevertheless been successfully extended to this case to predict the surface melting phenomenon.[167] All classical theories of phase transitions are necessarily based on measured macroscopic thermodynamic properties and hence have limited predictive power and nothing to say about the functioning of each mechanism on the molecular scale.[168] There have been recent efforts toward a true molecular level computational modelling of liquid phase nucleation in the metals copper and aluminium.[169] Using rare-event sampling techniques, the authors were able to predict the melting of these metals from simulated point defects and dislocations, finding that nonlocal behaviour was important for the initiation of the melting process. Unfortunately in the absence of the necessary data to take advantage of this or the equipment to obtain it I must rely on the classical theory. With this in mind the next section discusses some modelling methods for surface melting.

5.1 The system to be modelled

In order to obtain an accurate model of the surface melting observed in the previous chapter, at minimum the following effects must be taken into account:

- Interfacial reflectivity
- Laser-induced heating
- The first order phase transition
- Conductive thermal dissipation into the gallium and the glass slide beneath

See fig. 5.1 for a diagram describing this situation. It is not inaccurate to describe the first three of these using one-dimensional models. This is due to the volume in question being much smaller into the plane of the gallium mirror (10s of nm) than across it; the pump beamspot FWHM is 15.7 µm and hence the model may be viewed as semi-infinite in this axis. However, the characteristic length of thermal diffusion d is $\approx 50\,\mu\text{m}$ for polycrystalline gallium on the $\tau = 2\,\text{ms}$ timescale ($d = \sqrt{\chi\tau}$, χ = thermal diffusivity[170]), considerably larger than the beam spot dimensions. Hence heat dissipation must be modelled in three dimensions to obtain an accurate result for the timescales in question. Radiative losses are discounted as negligible relative to conductive dissipation (due to both the high thermal conductivity of gallium and radiative losses only being possible in the out-of-plane direction). The gallium depth is unknown but is assumed to be in the range of at least tens of microns. This is a result of the manufacturing method (as described more thoroughly in section 3.7) involving mechanical squeezing of the gallium by hand, making the thickness of the gallium under the membrane more difficult to gauge.

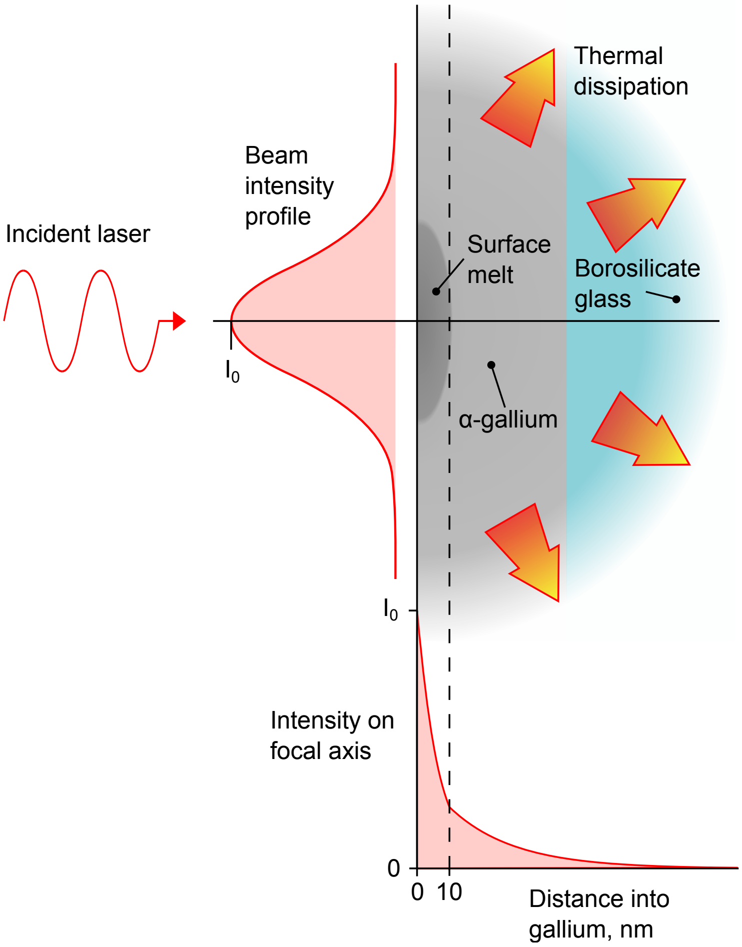

Figure 5.1: Schematic of the system to be modelled. The shown intensity distribution in the metal is based on an arbitrarily chosen 10nm surface melt at a laser wavelength of 1310nm. The vertical scale in the diagram is dependent on the beam width (FWHM = 15.7 µm at the pump wavelength for the experiment in the previous chapter).

5.2 Analytic heat transfer model

Although a complete physical model of laser-induced melting is inherently nonlinear and must be approached computationally, each of the physical processes involved may be individually analytically modelled. By considering only laser heating and thermal diffusion, for example, it is possible to obtain a piecewise expression for the transient change in temperature at the interface in the absence of melting. For this I collaborated by my colleague Dr. Vassili Fedotov who derived the following relation:

$$\begin{aligned}
&\Delta T(t) = \xi(t), t \leq \tau \\
&\Delta T(t) = \xi(t) - \xi(t-\tau), t > \tau \\
&\quad \xi = \frac{Ar_0}{\lambda\sqrt{\pi}}\left\{\arctan\left(\frac{2\sqrt{k_1 t}}{r_0}\right) + \frac{\lambda_1\sqrt{k_2} - \lambda_2\sqrt{k_1}}{\lambda_l\sqrt{k_2} + \lambda_2\sqrt{k_1}}\frac{r_0\sqrt{\pi}}{2L}\left[1 - \mathrm{erf}\left(\frac{L}{\sqrt{k_1 t}}\right)\right]\right\}
\end{aligned} \tag{5.1}$$

Here A is the intensity at focus, r_0 is the radius of $1/e$ intensity, L is the thickness of the gallium and τ is the duration of the pulse. λ and k are the thermal conductivity and thermal diffusivity respectively of gallium (λ_1, k_1) and borosilicate glass (λ_2, k_2). Consistent with the experiment described in section 4.3, I choose a radius $r_0 = 9.44\,\mu\mathrm{m}$. The function 'erf' is the error function. Gallium thickness L is treated as a free parameter due to the imprecise manufacture method as previously discussed, though variation of this parameter has a minimal effect on the resulting reflectivity as we shall see shortly. The pulse is taken to be a square wave of 500 µs duration. The gallium is considered to be polycrystalline and as a result obtains an isotropic thermal conductivity, taking the numerical average of the three axes (a-axis = 0.406, b = 0.883 c = 0.159, polycrystal = $0.482\,\mathrm{W\,m^{-1}\,K^{-1}}$) The expression is derived from known results in laser heating[171] using the assumptions that $L \gg r_0$, the laser fluence is applied onto a zero-thickness layer at the interface and insignificant heat is lost via radiation. This result may be used to determine the time-dependent temperature change at the beam focus due to application of a pulse - see fig. 5.2. It may be determined from this plot that the vast majority of the heat input during a pulse is dissipated before the following cycle and hence it is valid to consider each pulse in isolation. On the basis of this model it is possible to estimate the laser intensity threshold required to induce melting at a given temperature, or conversely estimate the sample temperature required to induce melting at a given laser intensity.

The predicted values may be compared with the experimental results, as derived from the data in fig. 4.9b. Fig. 5.3a compares the predicted temperature change at the end of a laser pulse ($t = \tau$) with the experimentallly determined equivalent of the maximum difference between sample temperature and the observed melting point for significant melting ($> 50\%$ of maximum reflectivity change - see fig. 5.3b) to be detected. Shown are the simulated results for very

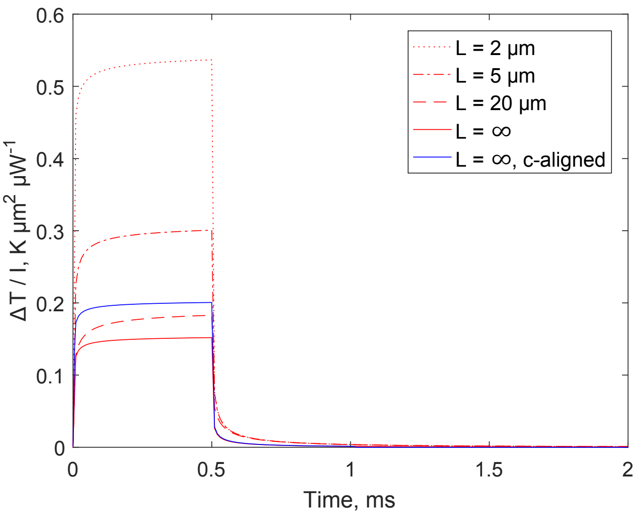

Figure 5.2: Predicted dynamics in temperature per unit intensity due to a square-wave pulse of 500 µs duration beginning at $t = 0$ and ending after a single cycle (500 Hz repetition rate).

thick gallium ($L >> d$) and thin gallium of several thicknesses along with experimental data. It is understood that α-gallium may preferentially form with dimers aligned along the interface such that thermal conductivity (and hence also diffusivity) perpendicular to the interface is minimised to correspond to that of the c-axis.[170] This possibility is included in the figure as values with appropriately aligned anisotropic conductivity. From these results it may be concluded that the model, given the known absorptivity of the metamaterial at the pump wavelength, predicts a laser-induced temperature rise insufficient to arrive at the melting point, anywhere between a very small 2 µm gallium thickness and the asymptotic case of a semi-infinite domain. Taken at face value, the result would indicate that a surprisingly small thickness of gallium is present (in the <2 micron range). As the real thickness is expected to be of the order of 100 to several hundred microns, this seems unlikely. In any case, concusions based on very thin gallium should be treated with caution as the equation assumes a gallium thickness larger than the spot size. An alternative and more convincing explanation has been previously posited by other authors: that the photonic excitation of metallisation in gallium is partially non-thermal in nature.[42,109,172,173] The laser excitation may instead excite the solid-liquid transition directly in a manner analogous to excitation between electron energy levels.[41,174] This would enable the transition to liquid phase to be photoexcited even at significantly below the melting point, consistent with the result of this experiment. This possibility is developed in section 5.4.

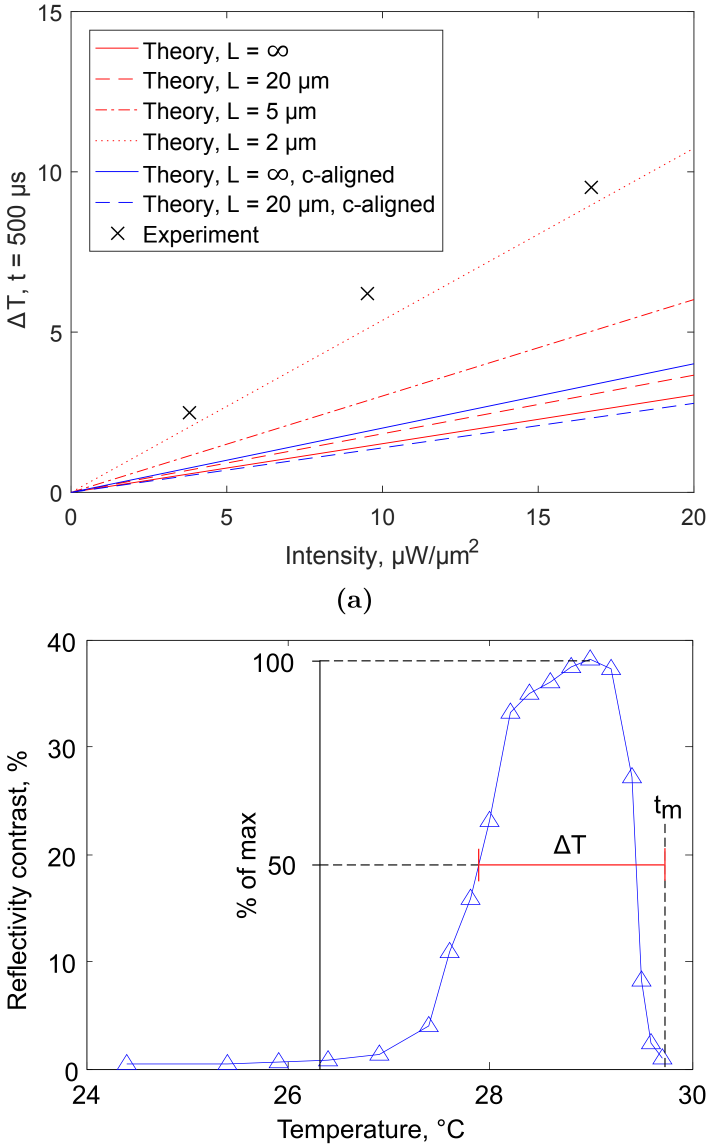

(a)

(b)

Figure 5.3: (a) Comparison of analytical and experimental results for laser-induced temperature change prior to significant laser excitation of surface melt. (b) Derivation of experimental values in (a) from source data, using the experimental curve for an intensity of 3.8 µW µm^{-2} as an example.

5.3 Steady state reflectivity model

By using a generalisation of the thermal model for the laser-induced temperature rise, I prepared a model of the laser heating induced reflectivity change in the steady state. Dr. Vassili Fedotov's thermal model, generalised to produce the temperature distribution including radial and depth dependence, is as follows.

$$\Delta T(t) = \frac{Ar_0^2}{\lambda c\sqrt{\pi}} \int_0^t \frac{e^{-\frac{r^2}{4k(t-t')+r_0^2}}}{4k\left(t-t'\right)+r_0^2} \frac{e^{-\frac{z^2}{4k(t-t')}}}{\sqrt{k\left(t-t'\right)}} dt' \tag{5.2}$$

A is the intensity at focus, c is the specific heat capacity of α-gallium, r_0 is the radius of $1/e$ intensity and λ and k are the thermal conductivity and thermal diffusivity respectively of polycrystalline alpha gallium. r and z are radial and depth positions in this cylindrically symmetric model and t is the time since application of the pulse, which is taken as arbitrarily large in the time-independent domain. For simplicity this model assumes a pulse of infinite duration and gallium of semi-infinite thickness. The extent of melting of gallium is determined by finding the volume which is above the melting point. This approximation, valid in the time-independent regime, is based on the known temperature distribution outside a volume heat source:

$$\Delta T = \frac{\dot{q}}{4\pi k r^2} \tag{5.3}$$

where ΔT is the temperature change due to the presence of the heat source, $\dot{q}$ is the thermal emission power, k is thermal conductivity and r is the radial distance from the centre of thermal emission. This equation is valid for $r > r_{source}$, the source radius. Hence the temperature outside the heat source is determined only by the position and local conductivity; a differing thermal conductivity introduced by melting near to the heat source does not affect the temperature at radially greater distances.

The reflectivity is determined from the calculated radial distribution of melt thickness, modulated by the radial intensity distribution of the beam. This enables the calculation of the reflectivity change due to the laser as a function of intensity and sample temperature for the experimental conditions; the results of this calculation may be seen alongside their experimental counterparts in figure 5.4. Part (a) of the figure shows the experimentally determined reflectivity contrast, defined as the percentage increase in reflectivity between the sample at no excitation and the maximum reflectivity that arises at the end of each 500 µs pulse. Part (b) shows the numerically determined equivalent change in the steady state reflectivity between zero excitation and continuous irradiation. Three key observations may be made here. First, in experiment there is a maximum temperature level, below the melting point, above which the reflectivity contrast begins to decrease. This is not seen in the simulation. This arises not because of a decrease in the maximum reflectivity, but because the sample temperature is

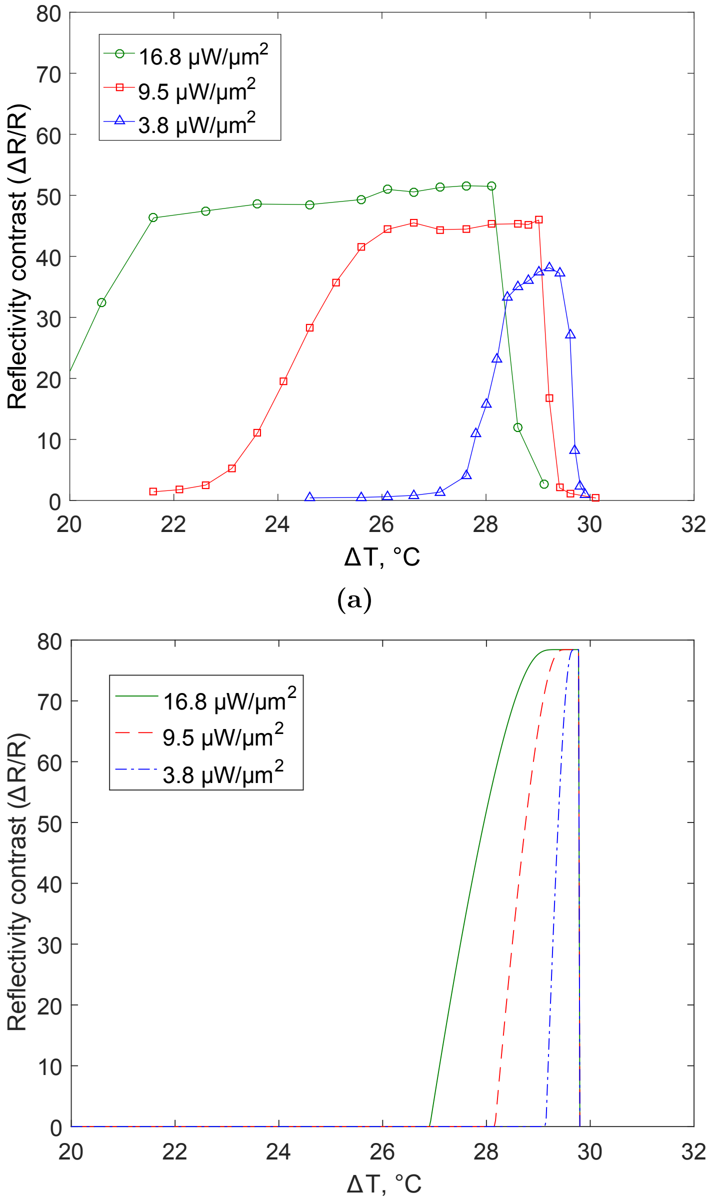

(a)

(b)

Figure 5.4: Comparison of experimental and simulated results for laser-induced reflectivity contrast. (a) Experimental reflectivity contrast across temperature for the three tested laser intensities. (b) Simulated maximum steady-state reflectivity contrast between zero excitation and steady state excitation at the three experimentally tested laser intensities. ΔR corresponds to the maximum change in reflectivity at 1550 nm, R to the base reflectivity in the absence of excitation.

sufficiently close to the melting point that the reflectivity does not have time to return to its base level before the arrival of the following laser pulse. The second key observation is that the maximum reflectivity contrast is significantly higher in simulation. The contrast seen in the simulation is the result of mapping the reflectivity variation of a simulated composite air-liquid gallium-α gallium interface with the appropriate liquid gallium thickness 1:1 with the reflectivity contrast seen in the reflectivity spectrum of the metamaterial at the 1550 nm probe wavelength (fig. 4.5c in chapter 4). The laser excitation experiment showed contrast significantly below this level. The model assumes the light arriving at the sensor is directly proportional to that reflected from the sample. This is the case in focus, but a localised reduction in gallium volume due to melting at the beamspot will cause a level of lensing of the probe laser. This could affect the focus at the sensor, reducing (or increasing) collection efficiency. This likely accounts for the discrepancy in reflectivity contrast between steady state total melting and the localised melting in the pump probe experiment. The final and potentially most interesting observation is that the laser-induced changes in reflectivity are seen at much lower temperatures in experiment than a laser-heating based Stefan problem model would suggest. As mentioned in the previous section, it has previously been hypothesised that this is due to a mechanism of direct light induced metallisation that is not explicitly thermal in nature. In order to test this theory, I applied a non-thermal reflectivity enhancement theory previously developed for gallium to the metamaterial, as discussed in the following section.

5.4 Non-thermal light induced transition

Much of the literature describes the laser-induced reflectivity switching in gallium as a non-thermal mechanism,[42] or otherwise as induced by direct excitation of covalent bonds within the gallium crystal in the manner of the pumping of a laser.[41] This is justified through the consideration that it is observed even when the temperature reached during laser excitation is significantly below the melting point, hence the transition seen is not directly analogous to bulk melting. It is notable that the result in fig. 5.3a shows experimenal observation of laser-induced melting at temperatures significantly below the level predicted by a purely thermal treatment, in line with this hypothesis.

One model for determining the dynamics of the metallisation of a gallium surface is derived from laser physics.[41, 174] The model consists of two components. The first is an experimentally determined dependence of apparent melt depth (determined from reflectivity) on laser intensity and temperature.

$$d = d_0 + \Delta \exp\left[-\mu \left(T_m - T\right)\right] \tag{5.4}$$

Here d is the melt depth, d_0 is the base melt depth (for low temperature and no

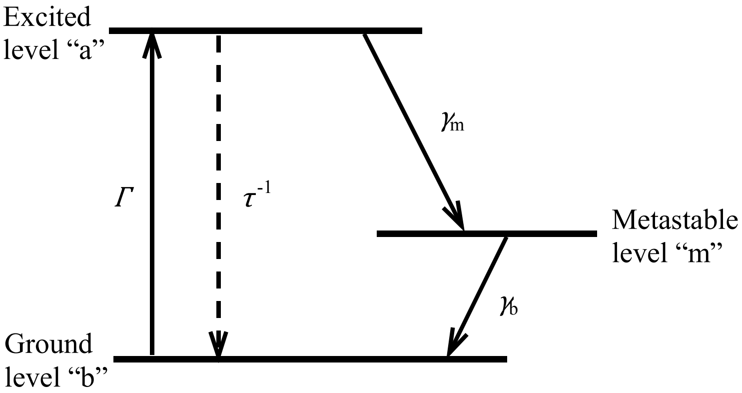

Figure 5.5: Three-level diagram of excitation of a unit cell of gallium, reproduced from the thesis of Dr. Vassili Fedotov of the ORC.[170] Γ is the excitation rate due to the laser, γ_m is the relaxation rate into the metastable phase and γ_b is the relaxation rate into the ground state from the metastable state. τ is the excited state lifetime.

laser radiation, taken as 2 nm), Δ and μ are fitting parameters and T_m and T are the melting point and sample temperature respectively. The second component of the model is a description of the excitation of gallium unit cells between states of ground state alpha gallium, a short-lived excited antibonding state and a metastable metallic liquid-like state in a form analogous to a three-level laser as seen in fig. 5.5. Assuming a CW laser (and therefore the stationary regime), we may arrive at an expression for the fraction of crystal cells within the skin depth of gallium that are maintained in the metastable metallic state (n_m/n), as derived in the thesis of Vassili Fedotov.[170]

$$\frac{n_m}{n} = \frac{\gamma_m}{\gamma_b} \frac{\Gamma}{2\Gamma + \tau^{-1} + \gamma_m\left(1 + \frac{\Gamma}{\gamma_b}\right)} \tag{5.5}$$

Here Γ is the excitation rate due to the laser, γ_m and γ_b are the relaxation rates into the metastable phase from the excited state and into the ground state from the metastable state respectively and τ is the excited state lifetime. Γ is defined by

$$\Gamma = (1 - R)\frac{I\alpha}{hvn} \tag{5.6}$$

where R is the reflectivity coefficient of the material at the pump wavelength, α is the absorption coefficient of alpha gallium at this wavelength, n is the number density of α-gallium crystal cells and I and v are the intensity and frequency of incident radiation. Using the above results the value n_m/n then determines the fitting parameter μ in equation 5.4 by way of the relation

$$\mu = \mu_0\left(1 - \frac{n_m}{n}\right). \tag{5.7}$$

This allows prediction of the value μ, based on relaxation and excitation rates derived from prior data, that has produced very good experimental agreement, with

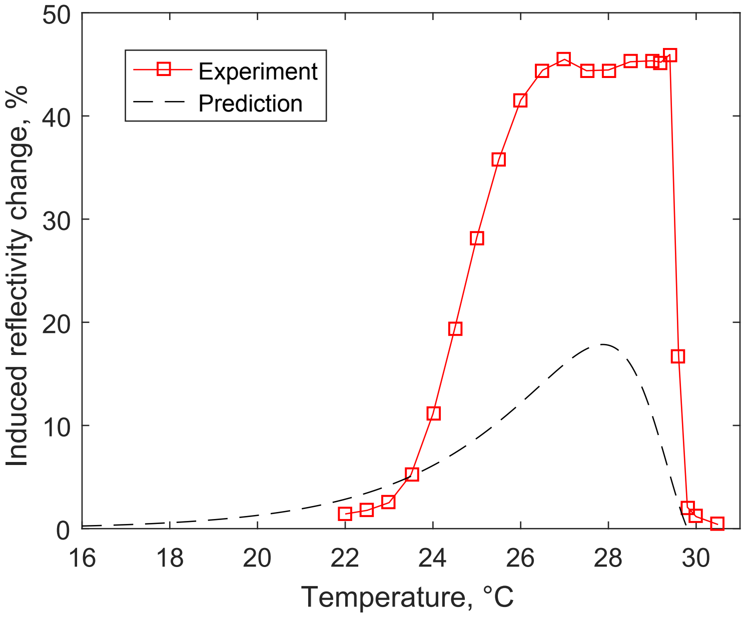

Figure 5.6: Comparison of theoretical and experimental results for laser-induced temperature change prior to significant laser excitation of surface melt for a pump intensity of 9.5 µW µm^{-2} and a probe intensity of 1 µW µm^{-2}. The experimental results are as given in figure 4.9b. The theoretical results are derived using predicted reflectivity for a gallium surface in air using the transfer-matrix method, with the reflectivity contrast normalised such that saturation occurs at the same level as in experiment.

only the parameter γ_b defined by the experimental data on which the model was originally used.[41] On this basis we applied this theory to the present experiment. Values for the constants are chosen as $n = 6.5 \times 10^{21}\,\mathrm{cm}^{-2}$, $R = 17.5$ (the room temperature pump-wavelength reflectivity), $\alpha = 4 \times 10^5\,\mathrm{cm}^{-1}$, $\tau = 1 \times 10^9\,\mathrm{s}$, $\gamma_m = 3.3 \times 10^{10}\,\mathrm{s}^{-1}$, $\gamma_b = 5 \times 10^3\,\mathrm{s}^{-1}$, $\Delta = 18.4\,\mathrm{nm}$ and $\mu_0 = 16.5$, as in the prior work. A useful comparison may be drawn in fig. 5.6. This figure compares the maximum reflectivity change reached by the end of the pulse in the experimental case with the predicted reflectivity change, applying the non-thermal melting model with the experimental parameters.Both theoretical and experimental curves grow to a maximum as the melt point is approached before a fast falloff to zero at the melt point itself. However, the nature of the rise is significantly different, with the experimental curve reaching a higher level. This is presumed to arise because the effective intensity in this experiment (taking into account the increased absorption of the metamaterial) is significantly higher than in the experiment on which the model was based and hence applicability is reduced. Consistent with this observation is that the experimental result shows signs of reaching saturation at its apex, such that there is a flattening of reflectivity at its apex. This is due to the melt thickness increasing to greater than the skin depth of gallium, so that an increase in intensity will no longer increase reflectivity. The model cannot account for this situation and instead predicts the reflectivity to asymptotically approach saturation as intensity tends to infinity. Hence the model appears to be more applicable only in the considerably sub-saturation regime, defined as $\Delta T_{max}/(T_m - T_0) \ll 1$ where ΔT_{max} is the maximum change in temperature reached at focus due to laser heating, T_m is the melting point of gallium and T_0 is the substrate temperature. It may be possible to improve the accuracy of the model by considering that the lifetimes of the excited and metastable phases could depend on the local temperature of the gallium. It should be noted that the increased absorption coefficient of the metasurface relative to plane gallium is taken into account in this model by increasing the effective absorbed intensity (I in equation 5.6) proportionally to the increase in the size of the absorption coefficient of the metasurface relative to the plane element.

5.5 Finite element models

As it is not possible to analytically model a phase change of this complexity, the finite element method is ideally required instead. Conceptually, there are a number of ways to approach this, with different assumptions possible depending on the timescale considered. As previously mentioned, the system may be modelled in one dimension if the characteristic diffusion length d is much smaller than the beam spot radius r. By $\tau = r^2/\chi$ (τ is the characteristic timescale of the experiment, χ is the thermal diffusivity of polycrystalline α-gallium) we can arrive at a timescale $\tau \ll 1 \times 10^{-4}\,\mathrm{s}$ for which this assumption is accurate. Hence on the microsecond timescale or below, a one-dimensional model is sufficient; a 1D model has previously been used to reproduce melting dynamics for nanosecond pulses.[175] However on the timescale of this experiment, such a treatment is not sufficient. Hence, higher dimensionality is required.

As the system is axially symmetric about the centre of the beam, a three dimensional model is not necessary: the system may be completely modelled as 2D axisymmetric. There are then two possible methods of modelling the melting:

- For elements that have reached the melting point, considering each element to be a mixture of solid and liquid gallium and defining optical properties of that element using the Maxwell-Garnett approximation. The fraction of liquid by volume is then defined by the heat energy that has entered the element as a fraction of the latent heat of the element.[175] This method is implemented in the FEM software (COMSOL), but requires sub-nanometre element sizes for the model to converge to a result. By von Neumann stability analysis this gives a maximum timestep of $\Delta t = \Delta x^2/(2\chi) = 40\,\mathrm{fs}$. Hence more than 10^9 iterations on a single-threaded process would be required to cover a millisecond timescale, which would take weeks to process on available hardware.
- Considering precisely defined regions of solid and liquid gallium with a

moving boundary between them. This approach, a simplified version of which is applied in the previous section, is known as solving the Stefan problem. The assumption of a single boundary is known to be accurate at long timescales as it is energetically favourable to minimise the surface area of the solid-liquid interface. This method is potentially useful, but requires the initial condition of the simulation to include a volume of liquid - it cannot simulate the heating process prior to a melt. Using equation 5.1 as a guide, this timescale is of the order of hundreds of microseconds, significant on the scale of the experiment. It is possible to simulate this using the assumption that the latent heat far exceeds the specific heat and hence the heat flow is quasistatic, but the accuracy of this approximation (outside of a fully time independent model such as that in the previous section) is a matter of debate.

With the above considerations, it must unfortunately be concluded that accurate simulation of this system using currently available computational resources appears impractical.

5.6 Cellular automaton

The non-thermal model discussed in section 5.4 is only accurately predictive for a relatively narrow range of phenomena. In light of this and the continuing computational intractability of full finite element models it is pertinent to consider other possibilities. With these considerations I have been working with a visiting researcher Dr. Liwei Zhang of Henan Polytechnic University, China, on an extension of the non-thermal model using a cellular automaton. As a brief introduction, a cellular automaton is a system consisting of (1) a grid of cells, each of which is allowed to be in a set of possible states, and (2) a set of transition rules. The rules allow the cells to transition between states during a series of discrete timesteps. The state a given cell will transition to over a timestep depends on both its own state and the states of its neighbours. By integrating the light-induced metallization model (section 5.4) into a cellular automaton the phase transition is allowed to have a more complex structure than the two domains of the original model, constituting a more general description.

A cellular automaton lends itself well to this kind of model as it intrinsically describes the dynamics of a set of discrete states which may be mapped to the states of excitation of the model. The automaton is hence defined to include three states mirroring the model's (see fig. 5.5) with transition into the excited state enabled by optical excitation and decay allowed from the excited state to the metastable state and from the metastable state back to alpha-gallium. Individual cell sizes are defined based on the (axial mean) α-gallium bravais lattice side length of 0.55 nm.[176] In order to accommodate the necessary physics, the automaton is expanded to allow probabilistic transition - a standard cellular automaton has

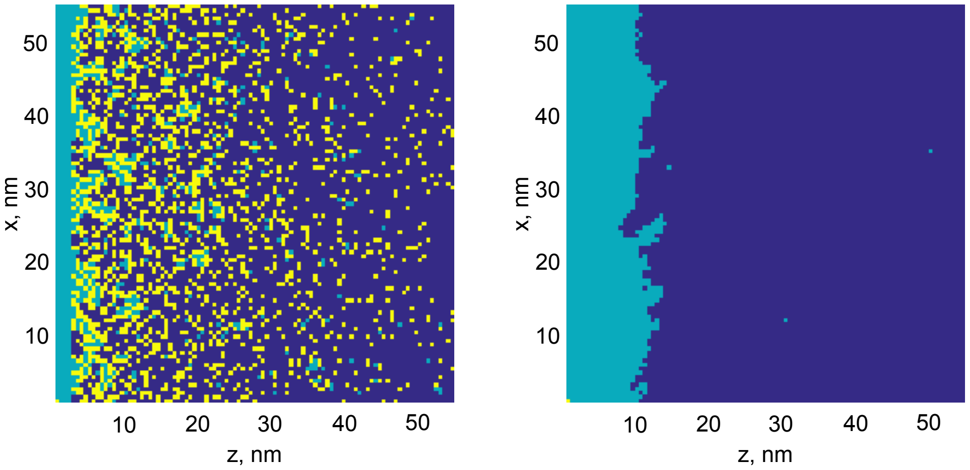

(a) (b)

Figure 5.7: Cellular automaton during simulation of differing pulses. (a) Snapshot of a 100 femtosecond pulse. (b) Snapshot of a 100 microsecond pulse. Blue cells correspond to alpha gallium, yellow to excited gallium and cyan to the metastable state. In both cases the snapshot is taken at the midpoint of the gaussian pulse. Axis x is defined along the interface, while axis z defines distance into the bulk from the interface at z = 0.

proscriptive immutable rules defining the required conditions for a transition, an insufficient condition for realistic physical description. One example of this expansion is probabilistic decay. Once the timestep τ is defined, for a cell in an excited state the probability of decay is given by $1 - \exp(-\gamma\tau)$, where gamma is the appropriate relaxation rate. Similarly, the probability of absorption of a photon across a cell of side d and refractive index $n = n' + in''$ is $1 - \exp(-n''d)$. A thermal mechanism is included with the addition of a further excitation path from alpha gallium to the metastable state directly, mirroring thermal melting. This transition is again defined probabilistically, with the probability of transition increasing as the number of nearest-neighbour cells in the metastable state increases. Finally an additional rule is included to ensure that a minimum natural surface melt layer of 3 nm thickness is maintained at the interface, in line with experimental observations.

The model itself is defined as a two-dimensional slice into a 3D gallium bulk under laser irradiation of a spatially invariant gaussian pulse. Some early tests suggest that the model will eventually have the capacity to accurately reproduce the reflectivity rise during and following pulses from the femtosecond to the submillisecond regimes - see figure 5.7 for a visualisation of the automaton at the midpoint of 100 femtosecond and 100 microsecond pulses. Note that in the case of the 100 femtosecond pulse a large proportion of excited cells remain in the short-lived excited state (relaxation rate $\gamma_m = 3.3 \times 10^{10}\,\mathrm{s}^{-1}$) while at the same point in a 100 microsecond pulse photoexcited cells have largely passed through both this decay and the much slower decay of the metastable state ($\gamma_b = 5 \times 10^{3}\,\mathrm{s}^{-1}$) back into the ground state and the dynamics are dominated by the thermal mechanism governing transition from the ground state to the metastable.

Further discussion of the results so far is possible, but premature. The transition rates, nearest neighbour interaction strengths and balance of thermal and non-thermal contributions remain under evaluation and are subject to change. It is hoped that a more accurate description of the thermal mechanism behind the ground to metastable transition will allow these values to be precisely defined.

5.7 Conclusions

Gallium's light induced reflectivity change is an interesting phenomenon that has been the subject of considerable research. The magnitude of the effect and the timescale over which it arises imply that both thermal and non-thermal mechanisms are in play. Accurately modelling this system on a millisecond timescale is a hard problem: many prior experiments have been conducted in this regime, but the system has not yet been fully simulated. One prior simulation in the nanosecond regime indicates a fully thermal mechanism.[175] From analytical and numerical thermal models of laser heating in the submillisecond regime it appears likely that the system of gallium interfaced with silicon nitride in a metamaterial absorber is only partially governed by a thermal process. It would appear that the presence of optical radiation causes the first order phase transition of gallium melting to behave in a manner consistent with a second-order phase transition, with the breadth of the transition dependent on the intensity of the irradiation. This is evidenced by metallisation arising at temperatures predicted to be several degrees below the melting point. An initial examination of a previously developed non-thermal theory of gallium metallisation determined the theory to be insufficient to describe the metamaterial. Full finite element modelling of this system was investigated and remains impractical. With the aim of modelling the system on a more reasonable timescale, I have begun an investigation of a new non-thermal model incorporating a cellular automaton in collaboration with a visiting colleague. The results so far show qualitative agreement with prior experiments, but further development is necessary to fully implement the method. The model remains under development following my departure as that project is now entirely under the control of my colleague.

Chapter 6

Nanoimprint-based patterning for phase change plasmonic metamaterials

Prior work in the area of metamaterials produced by patterning metals with ‘bas relief’ and ‘intaglio’ type structured surfaces has shown this type of manufacture to be useful for control of visual spectral reflectivity - or colour[177] (’Bas relief’ and ’intaglio’ refer to raising and indentation of structures relative to the surface respectively). Designed to mimic the structural colour phenomen observed in many biological materials,[178] this type of structured surface has been suggested for potential application in jewellery making and security, as the colour of such a material would not degrade over time and it would be extremely difficult to produce forgeries. If it is possible to implement this in gallium metal, the accessibility of control of optical properties via phase switching could enable such exotic possibilities as phase change based visualisation and ‘chamelion’-like optical camouflage, a highly sought-after application of metamaterials.[179, 180]

By structuring a dielectric material surface and bringing it into contact with liquid gallium, the nanostructure may be imposed onto the gallium surface. The thermodynamic phase of the gallium may then be freely cycled with the dielectric in place and the structure will be maintained throughout. Through this methodology resonant structures may be produced which consist entirely of phase-change metals. This chapter discusses progress toward the realisation of such a material.

6.1 Computational modelling

Several varieties of nanoimprint metamaterial were simulated numerically including intaglio ring structures, anisotropric arrays of bas relief cuboids and square gratings. ’Bas relief’ and ’intaglio’ refer to raising and indentation of structures relative to the surface plane respectively.

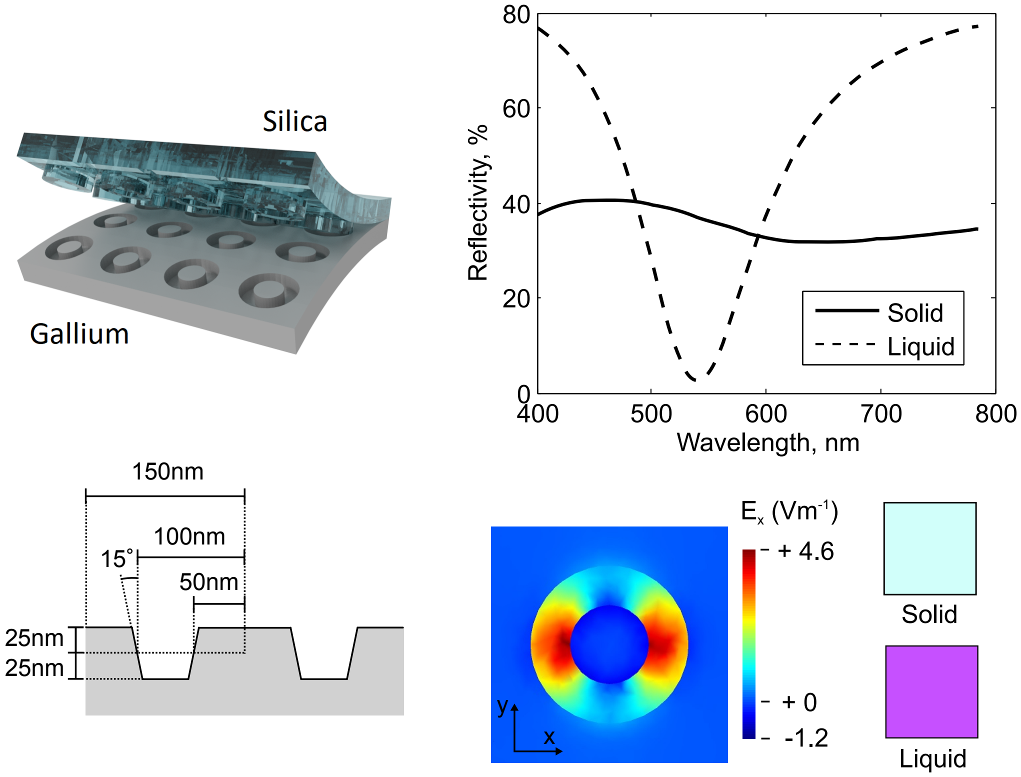

(a) (b)

Figure 6.1: 'Intaglio' nanoimprint gallium metamaterial. (a): Exploded visualisation of manufacture process and dimensions of simulated metamaterial. (b): Simulated normal incidence reflectivity for each structural phase, electric field map at liquid phase resonance at a depth of 25nm and perceived colours in reflection at normal incidence.

6.1.1 Intaglio ring absorber

This ring-shaped structure, produced by indentation of gallium with raised areas on a glass surface, was designed based on previous work on similar structures in gold by Zhang et al (which did, of course, have optical properties fixed at the point of manufacture).[177] A diagram of the unit cell (or meta-atom) of this material is presented in fig. 6.1a. The design displays a tuneable visible band reflectivity spectrum (and hence colour) through variation of its structural parameters. The result shown by the simulation was a switching of the colour of the material on phase transition to its liquid state, as can be seen in fig. 6.1b. It was assumed that the solid phase case was purely α gallium, ignoring the likely presence of a few-nanometre interfacial layer of surface melt. The electric field map illustrates that the absorption is produced by a slot mode of the ring structure.[181] The theoretical colours produced by the material (as Red/Green/Blue coordinates) were derived from simulated normal incidence reflectivity spectra as related to the Judd-Vos modified International Committee on Illumination (CIE) 2-deg colour matching functions (for a description of the theory behind this see Appendix B).

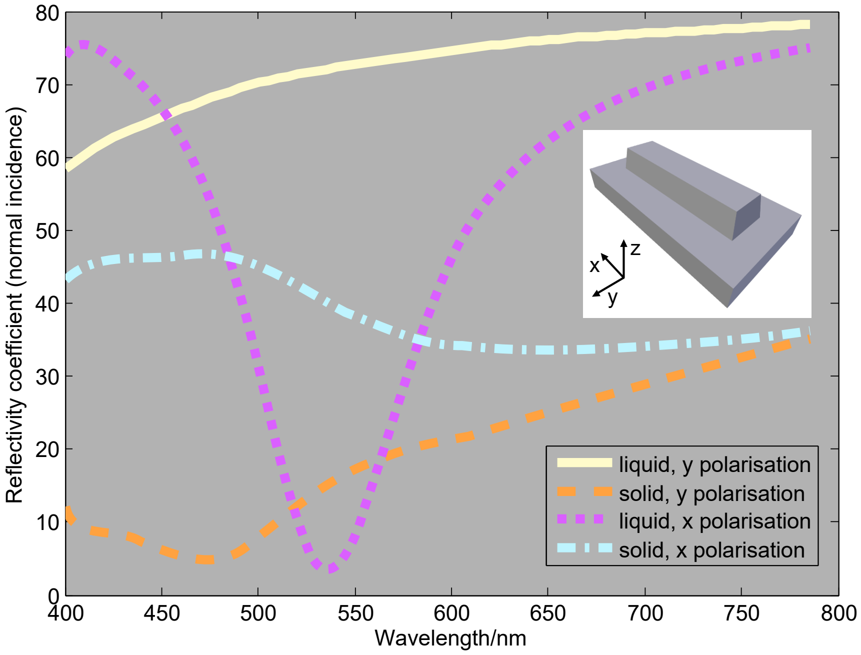

Figure 6.2: ‘Bas relief’ (embossed) ‘bar’ gallium nanoimprint metamaterial; simulated reflectivity of the metasurface in both fully α-solid and fully liquid phases for each linear electric polarisation at normal incidence. The colours of each line graph correspond to perceived colours in reflectivity at normal incidence. Inset: the metamaterial unit cell. Dimensions: periodicity x 270 nm, y 140 nm, relief bar 200 × 50 × 40 nm (x,y,z).

The physical dimensions of the meta-atom are given in fig. 6.1a.

6.1.2 Anisotropic bas relief cuboid metamaterial

Further to the investigation of colour-controlled metamaterials a polarisation dependent relief gallium metamaterial was simulated. This cuboid structure is produced in much the same way as the ring absorber by indentation of liquid gallium with a structured glass surface. By tuning its structural parameters it was optimised to display four contrasting colours; one for each orthogonal linear polarisation in the solid state and one for each polarisation in the liquid state. A schematic of the metamaterial, its spectra in each case and the resulting perceived reflected colour, displayed in the lines themselves, may be seen in fig. 6.2.

6.2 Grating structure proof of concept

As previously noted, an experiment was published in 2012 describing the production of gallium diffraction gratings with sub-micron pitch and a depth of 30 nm.[49] To extend this, I chose to prepare a subwavelength grating with much greater aspect ratio. Aspect ratio is here defined as the ratio of the depth of the grating (from peak to trough normal to the plane of the surface) to the greatest

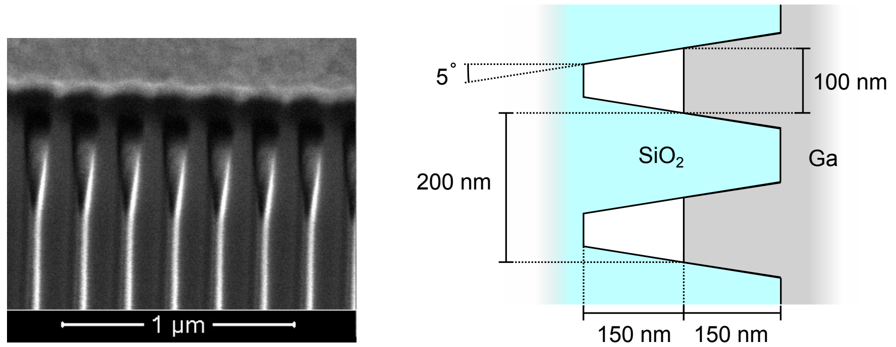

(a) SEM image **(b)** Schematic

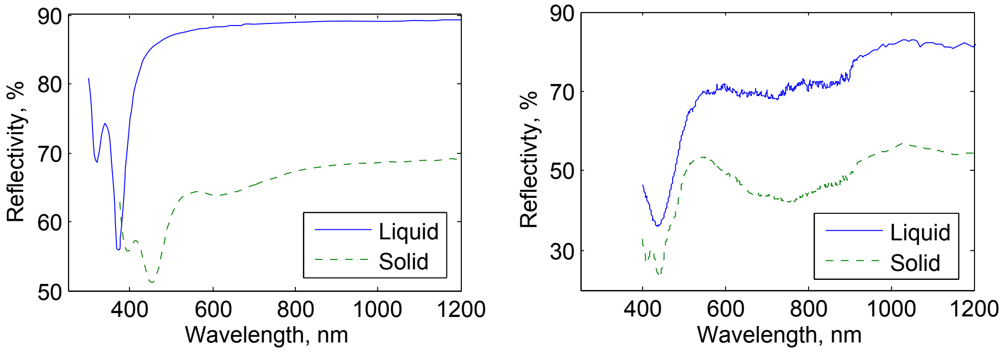

(c) Numerical prediction **(d)** Experimental results

Figure 6.3: SEM image of exposed borosilicate grating and schematic and reflectivity spectra (simulated and experimental) of gallium nanoimprinted grating, taken at normal incidence and polarised parallel to the grating's periodic axis.

width of the milled depression. Hence a grating structure was prepared in a silica wafer with a 200 nm pitch and 300 nm depth using FIB milling.

Due to the fine pitch of the gratings, area (raster array covering a 2D domain) based milling was impractical and hence line-based (1D array of points) milling was used as an alternative. Due to this the standard method of calculating depth based on area dosage and known mill rates was inapplicable and hence the precise depth of the produced gratings is unknown; instead grating depth was estimated using SEM imagery to be of the order of 300 nm. Using line-based milling results in a grating with sloped walls as the ion beam has a gaussian intensity profile, resulting in a falling off of the milled depth on either side of the line (fig. 6.3a).

To produce the gallium grating a small sample of liquid gallium was placed onto a silica wafer substrate along with a small quantity of epoxy at the edges of the wafer. Taking advantage of a mask aligner as an *ad hoc* nanoimprint system the imprint mask in the superstrate wafer was lowered into contact with the substrate, thus compressing the gallium such that it enters the gratings. Imagery and reflectivity (both simulated and experimental) are given in fig. 6.3d.Grating coupled SPP resonances are visible for both solid and liquid phase gallium in the region of $\lambda = 400$ nm. The characteristic dual trough shape of the resonances is introduced by tapering of the gratings in both simulation and experiment. This tapering and the resulting resonance splitting may or may not be desirable, depending on application. The simulation, which was run with the gallium infiltrating 150 nm into the gratings, appears to mirror the experimental results well, albeit showing an overall reduced level of reflectivity. Hence the trial indicates that gallium is indeed able to infiltrate into deep nanoscale gratings, contrary to the suggestion of standard wetting theory: to successfully wet the gratings at all, the Young-Laplace equation (applying the surface tension of gallium[182] $\approx 700\,\mathrm{mJ\,m^{-2}}$) requires a pressure differential of more than 14 MPa, or roughly a thousand times the pressure exterted by an elephant's foot. It should be noted that the macroscopic Young-Laplace equation is expected to still be valid at the nanoscale.[63] Despite the fact that our mask aligner certainly cannot achieve this, the gallium remains in contact with the grating walls. This appears to be the result of the oxide that naturally forms on a gallium surface, supplying it with 'non-newtonian' fluid properties, as previously noted by Dickney et al.[183] Further confirmation of this comes in SEM imagery of manufactured gallium gratings discussed later in this chapter (section 6.3.2).

In accordance with the fact that solid α phase gallium may not exist in micro-to-nanoscale droplets, it was anticipated that the solidification of gallium within the gratings may be inhibitied. As evidenced by fig. 6.3d, this appeared not to be the case. On the contrary, the gratings' optical properties appeared to be more consistent with the solid phase on the basis of numerical modelling. This may be due to the preferential existence of other metastable phases of gallium (β, γ, δ and so on) in confined geometries, as discussed in Soares et al.[184] This may be understood as the structuring of the dielectric surface affecting the molecular ordering of the liquid gallium surface, which naturally forms dimer layers in proximity to the surface.[40] This may be the mechanism for gallium's anomalously large reflectivity contrast upon melting; if this is so then surface relief structures in general may display more complex behaviours than numerical modelling using static optical dispersions for solid and liquid phases may suggest.

Overall this initial test may be considered a success, but the manufacturing method is limited to the use of monolithic solid glass wafers. As one aim of this research was to develop methods to produce this kind of switchable surface at large scales, it is useful to consider methodologies which may be scaled up further.

6.3 Polymer gallium nanoimprint gratings

As previously pointed out, a major objective of this project was the development of optical metamaterials which may be produced on macroscopic scales. Nanoimprint materials are one route to achieving this aim, as nanoimprint-type processing may be conducted on a roll-to-roll commercial basis if used with flexible substrates. Hence it is useful to develop a process which uses this methodology.

Liquid gallium brought into contact with a dielectric surface will, as noted in section 2, behave very differently depending on the level of surface oxidation of the metal. One fascinating experiment published in 1957 demonstrated that the capillary forces exerted on liquid gallium in a progressively evacuated container vary dramatically as the container is evacuated: at 1 bar the liquid adheres strongly to the walls, but in vacuum that same interaction is strongly repulsive.[64] It is understood to be due to the dramatic change in properties afforded by gallium's oxide layer that the metal has been shown to infiltrate nanoscale features.[49] Hence it may be presumed that a reasonable atmospheric oxygen concentration is required for the production of nanoimprint structures. However, the early testing of squeezed gallium samples has shown that squeezing in atmosphere produces an interface with an inconsistent and often patchy appearance, with the apparent quality of the surface qualitatively proportional to the speed of motion of the droplet during squeezing. Conducting the experiments at atmospheric pressure could also result in air pockets trapped inside the imprinted structures. Hence in order to avoid these issues, it was decided that the squeezing process should be tested under low pressure conditions - gallium has previously been shown to develop an oxide layer at low pressures,[64] so this was expected to function. By varying the pressure, an optimum that balances the need for adhesion to the dielectric with surface quality could be found.

6.3.1 Method

To attempt this, the ability to process samples in a controlled environment is required, with control of pressure at least down to the submillibar range. This is not possible in a glove box, so without access to a commercial system a dedicated nanoimprint chamber of my own was required. Such a chamber was designed and constructed, based around a 6-port vacuum cross as pictured in fig. 6.4a and b, with ports for vision, vacuum pump connection and a single vacuum motion feedthrough with which the imprint process is conducted. An explanatory diagram of the process is given in fig. 6.4c. The imprint process is conducted as follows:

- The imprint mask is mounted on the sliding part of the nanoimprint assembly (fig. 6.4c, green component) using double-sided graphite tape. A double thickness of tape is used on one side to angle the mask such that the motion of the liquid droplet during imprint is predictable.
- A window flange is opened and the sliding part of the assembly is attached to the motion feedthrough.
- The gallium sample to be used is in molten state, overcooled down to room temperature. A single droplet of gallium (approx. 3mm diameter) is placed onto a cleanroom-prepared silica slide. The slide is placed in the substrate holder.
- The chamber is closed and evacuation begins. The duration of evacuation is

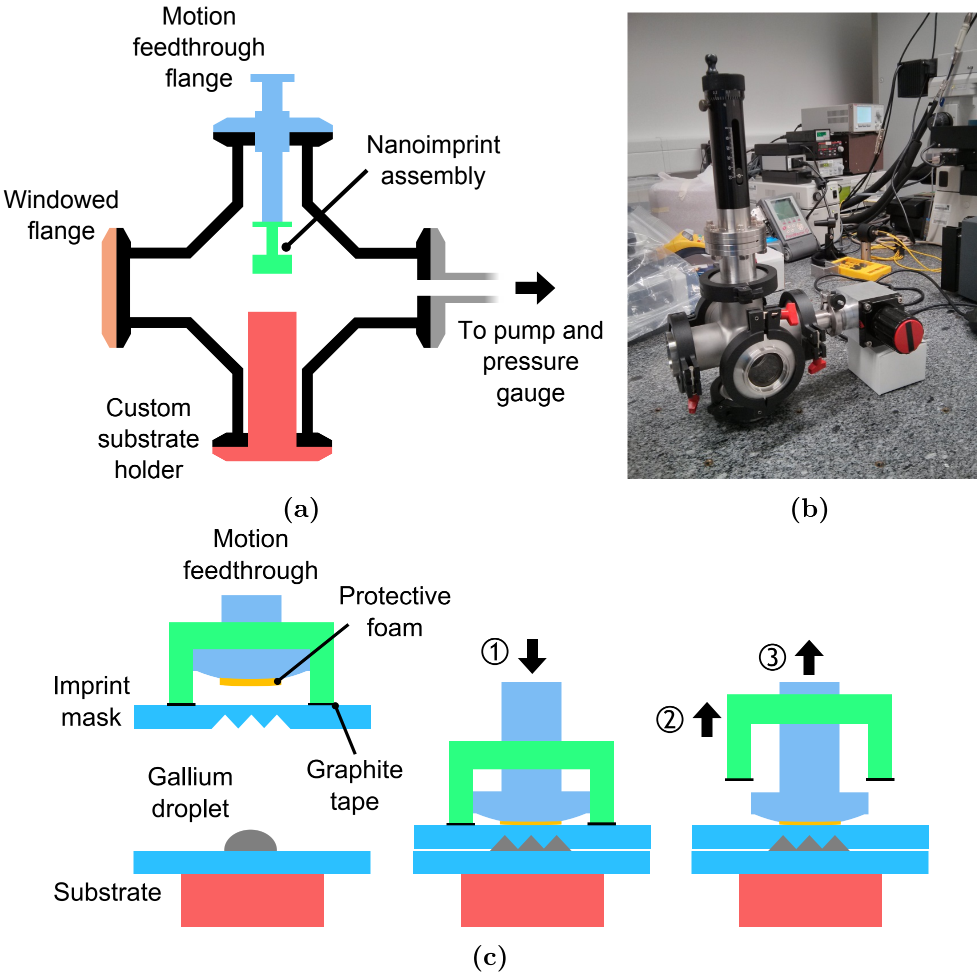

Figure 6.4: Nanoimprint chamber: (a) Chamber schematic, showing the KF (Klein Flange standard) vacuum cross and key components as listed. The chamber includes two additional windows at the front and back (not pictured). (b) Assembled chamber (c) Imprint methodology. Once the desired pressure level is attained, the motion feedthough is lowered until the feedthrough meets some resistance; the chamber is evacuated. The liquid gallium is solidified by application of a small sample of solid gallium and the removable holder (green) is lifted. The motion feedthrough is then raised.

timed in order to arrive at the desired pressure.

- The vacuum feedthrough is lowered until the fixed part of the imprint assembly comes into contact with the imprint mask.
- The chamber is vented and the window flange is opened.
- A small solid gallium crystal is pressed into the now visible bead of liquid gallium that has been expelled from between the imprint mask and the substrate. This causes the overcooled liquid droplet, along with the gallium remaining under the mask, to slowly solidify.
- After a minute, the sliding component is raised off the mask and removed from the assembly. Doing this with the motion feedthrough lowered allows the graphite tape to be removed without risking parting the mask from the gallium.
- The vacuum feedthrough is raised and the sample removed.
- The chamber is closed and evacuated.

For the superstrate (imprint mask) I chose amorphous polyethylene terephthalate polymer (or PET) of 0.25 mm thickness and 0.75 mm borosilicate glass for the substrate. A series of blank runs (tests without imprint structures) of the chamber were conducted in order to determine the ideal pressure for the imprint procedure. As a result a pressure of 1×10^2 mbar was chosen as pressures of 10 mbar and below often caused unwanted side effects such as premature solidification and total expulsion of the liquid.

Imprint masks were prepared using FIB lithography and the depths determined using an optical interferometry profiler. 25×25 µm grating patterns of pitch 400, 600, 800, 1200 and 1600 nm and depths 75, 120 and 600 nm were fabricated. Linewidths were chosen as the half-periods for each grating. The nanoimprint process was applied as above. With the gallium in solid state, the polymer superstrate was removed and the structures imprinted onto the gallium were inspected under SEM.

6.3.2 Results

It was expected that some of the grating cavities would be filled, but a limiting case would exist for which the gratings were too narrow for the gallium to enter. Instead it was found that the gallium would only enter the gratings of pitch 600 nm and below, as may be seen in fig. 6.5. This was unexpected but was considered likely to be due to implantation of gallium ions into the polymer during the FIB milling process, affecting the wetting properties of gallium in the surface. Other processes such as electron beam lithography or photolithography, which would not introduce this issue, could be harnessed instead. However, the use of gallium ion milling had an unexpected benefit. In the investigation of gallium nanoparticle growth through

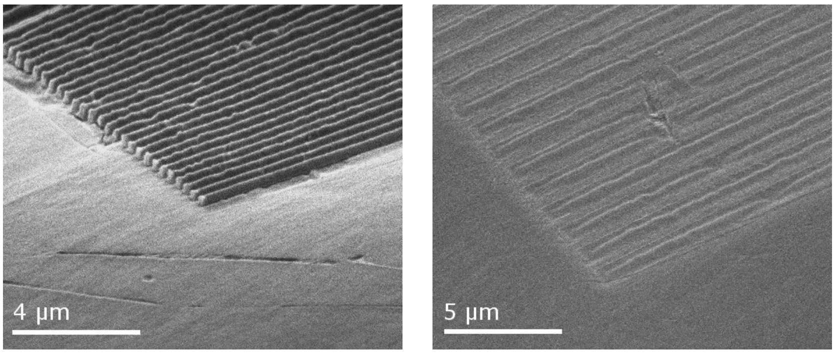

(a) **(b)**

Figure 6.5: Nanoimprinted gratings in solid gallium produced from masks of (a) 600 nm and (b) 1600 nm pitch, both of 600 nm depth.

physical vapour deposition (discussed in chapter 7) it was found that implantation of a PET surface with gallium ions improves the adhesion of gallium to the surface, as evidenced by a reduction in the wetting angle. During milling a fraction of deposited ions will be deposited outside the desired milling area due to the gaussian cross-section of the gallium ion beam. This effect would become more significant in the case that the grating pitch is comparable to the FIB spot size, improving the adhesion across the unmilled areas of the grating and improving conditions for imprinted gallium to enter the grooves.

Prior to the above SEM investigation, reflectivity spectra of the gratings were obtained with the PET in place, as seen in fig. 6.6. These were acquired in transverse electric polarisation (defined as normally incident and polarised along the periodic axis of the grating). The experimental result is significantly different from simulation. Marked divergences include overall lower reflectivity and resonance depth and position deviating considerably. The high-frequency oscillations in the simulation are a finite element artefact and are not expected to appear in experiment. It seems likely given the presence of sets of dual resonances in both experment and simulation that they have the same physical source, though in other respects they differ signficantly. This could be in part due to imperfect grating quality as can be gleaned from fig. 6.5; the gratings will necessarily not correspond precisely to the simplified simulation (of a geometry type identical to fig. 6.3) and hence the resulting spectra would be expected to differ.

The considerable overall reduction of reflectivity across a broad band is of particular concern. The effect dominates the spectra and makes resonant features related to the grating pitch difficult to discern, in addition to likely affecting the characteristics of the resonances. It is theorised that this was also caused by implantation of the PET imprint mask with gallium ions during FIB milling. To test this theory samples of PET with varying dosage of gallium were prepared and transmission spectra were obtained in each case. Using the assumption that the vertical distribution of implantation into the mask is identical in each case (not

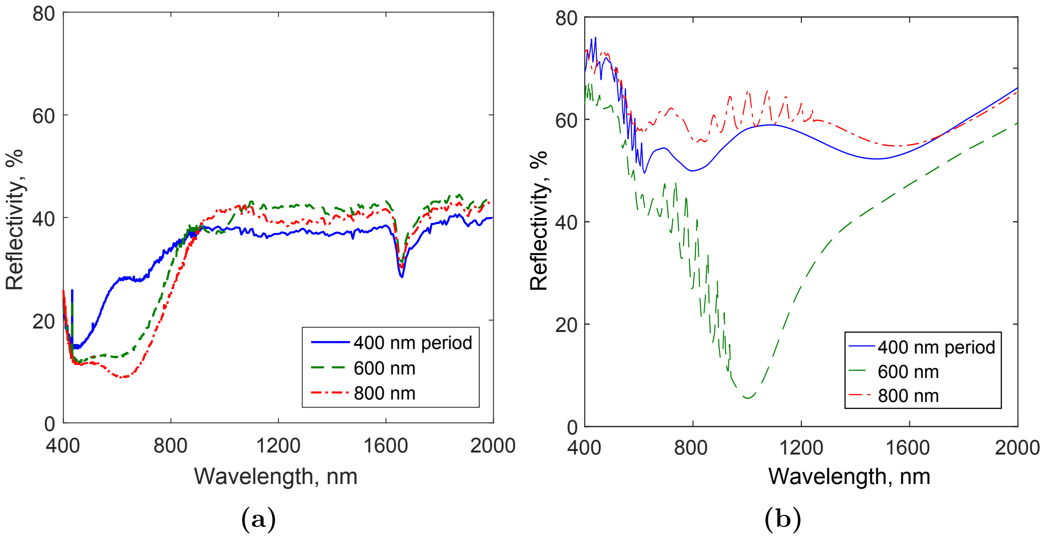

Figure 6.6: Reflectivity spectra for nanoimprinted gratings of depth 600 nm and varied pitch in (a) experiment and (b) simulation.

unreasonable given the distribution would be expected to show a consistent exponential decay into the bulk) I estimated the relative extinction coefficient introduced by the implantation and investigated the experimental variation of the relative extinction coefficient with total gallium ion beam fluence - see fig. 6.7. The relative extinction coefficient k_r is the imaginary component of the refractive index and is given by $k_r = -\lambda \log(T/T_0)/(4\pi d)$, where λ is the wavelength, T is the transmission coefficient for the sample, T_0 is the transmission coefficient in the absence of gallium implantation and $d = 10\,\mathrm{nm}$ is an arbitrary coefficient. A single relative extinction coefficient was obtained for each dosage by taking the mean across wavelength. It may be seen that the extinction coefficient increases linearly with dosage over the characterised range. Hence it is clear that the use of the FIB to pattern PET is causing a linear and predictable level of optical losses. This phenomenon is likely to extend to other dielectrics as well. Indeed, it probably accounts for the increase in losses in a borosilicate glass / gallium grating relative to simulation (fig. 6.3).

The issue of gallium ion implantation, while unfortunate, does not prevent further development of the process. Many alternative patterning processes (such as ultraviolet and electron beam lithography) are available which do not fall prey to this issue and are indeed required to scale the imprint method up. If some level of gallium implantation is desired to improve wetting this may be accomplished by applying a low dose of gallium ions after patterning, thus minimising the effect relative to what was observed here.

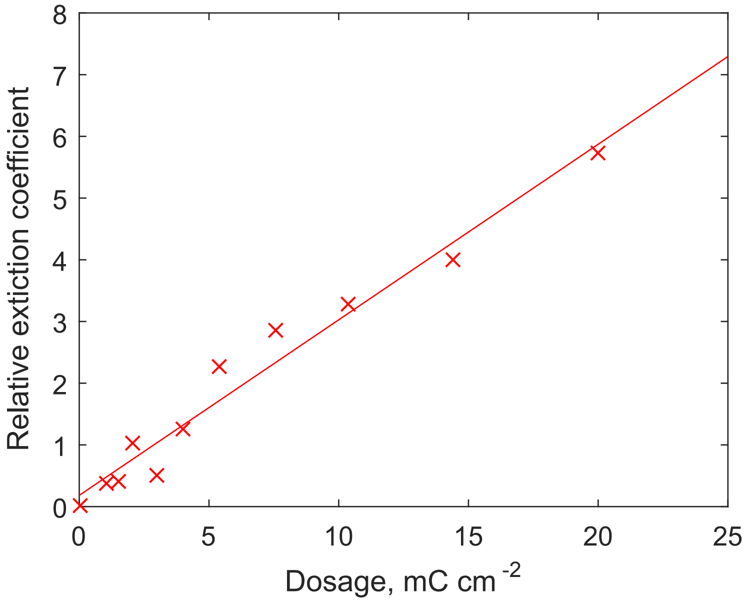

Figure 6.7: Relative extinction coefficient variation as a function of FIB dosage.

6.4 Conclusions

The possibility of producing metamaterials on an industrial scale is a major motivator in the field and a vital component to enabling real applications beyond the lab. I have arrived at some success in the development of a scalable manufacturing process that can produce structured metallic surfaces with switchable optical properties. I have demonstrated a thermally switchable gallium grating embedded in silica as a proof of concept, which showed reflective properties reasonably consistent with expected results from simulations. I further manufactured high aspect ratio gratings of gallium embedded in PET, though the level of infiltration of the liquid metal into the gratings proved to be inconsistent and experimental reflectivity spectra were hence difficult to interpret relative to simulations.

I have developed simulations showing that a variety of other achievable metamaterial structures can enable new optical surface properties in gallium. Unfortunately, contamination with gallium ions during the FIB manufacturing process presented difficulties with the characterisation of the produced structures. By taking advantage of alternative nanolithography methods, however, it should be possible to alleviate this.

Chapter 7

Templated assembly of metal nanoparticle films on polymer substrates

Metamaterials have been inarguably successful in enabling new functionality at ever shorter wavelengths. As a result of this success the functional frequencies of metamaterials are approaching metals' plasma frequencies. This has required the construction of ever smaller features, which is now testing the limitations of the current standard 'top-down' techniques. As a result the necessity of developing 'bottom-up' or self-assembled manufacture of nanoscale structures across large areas is becoming apparent.[185] Control of self-organisation is one route to this long-term aim; in combination with material properties which remain useful at high frequencies, such methods could be instrumental in driving the development of new metamaterial functionality. The plasmonic properties of gallium are consistent into the ultraviolet,[186] enabling targeting of applications using the full breadth of the visual spectrum. In this chapter I report a method of influencing the growth and self-organisation of gallium nanoparticle films as a step toward achieving both of these aims. This is particularly valuable as other self-organisation based methods, such as colloidal self-assembly[187] and self-assembly with DNA[188] are held back by their complexity and expense. Nanostructuring of substrates, by contrast, may be achieved through cost-effective and scalable nanoimprint methodology.

My templating of gallium nanoparticle growth is produced by texturing polyethylene terephthalate (PET) substrates with step grating patterns via FIB milling prior to resistance evaporation of gallium metal onto the gratings (fig. 7.1). It should be noted that my interest in PVD of gallium onto PET films was piqued by the work of Mr. Akihiko Ohtsu, a visiting researcher from Fujifilm corporation, Japan, who previously investigated deposition onto such unstructured samples.

Control over particle size and positioning is most effectively achieved (for a given mass-thickness of deposited material) when the characteristic dimensions of

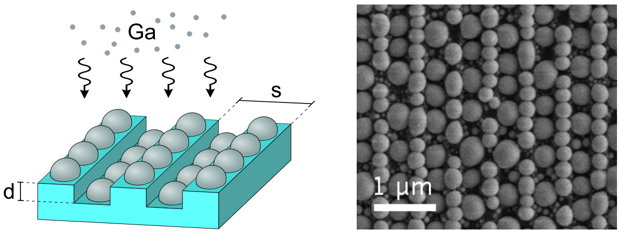

(a) Schematic diagram **(b)** SEM image

Figure 7.1: Visualisation of gallium nanoparticle ordering within a step grating structure on a PET substrate. (a) Schematic of nanoparticle formation during evaporation, denoting the depth d and period s of the grating. (b) SEM image of resulting self-assembled structure.

the substrate structure are comparable to the center-to-center separation of particles that would be produced via self-organized growth on an unstructured substrate.

7.1 Gallium physical vapor deposition

On an unstructured surface, gallium films grow in the Volmer-Weber (VW) mode, forming discrete, randomly distributed nanoparticle "islands" rather than contiguous thin films.[189, 190] This is indicative of the fact that the latent heat of evaporation for gallium from the PET surface is less than the latent heat of evaporation from the bulk metal - in consequence, the incident atoms adhere preferentially to the previously deposited gallium. The physics of VW thin film growth has been extensively studied, though typically for solid-phase deposition, i.e. substrate temperatures below the size-effect-depressed melting points T_m^* of deposited materials, though subsequent above-T_m^* annealing has been employed as a method for the production of metallic nanoparticles.[191] Gallium is peculiar in this regard: Despite the fact that its 303 K bulk melting point is already unusually low for a metal, size-effects on T_m are inconsequential to the present study because the very formation of the bulk crystalline α phase is suppressed in the confined geometry of nano/microparticles;[192] Ga remains in the liquid state to cryogenic temperatures, solidifying in one of several "metastable" crystalline forms only below ~255 K. The mobility of Ga atoms deposited on uncooled planar substrates thus enables growing particles to minimize the surface energy by adopting a truncated spherical shape.

This behavior is analogous to the micro/macroscopic condensation of water on hydrophobic surfaces and may be understood in the same terms despite the dimensional disparity of around three orders of magnitude.[190] Computational models of droplet accretion from vapor condensing on a surface as liquid[193] account for the evolution of their size and spatial distributions through consideration of three interacting regimes: First, the nucleation and growth of static droplets via the Brownian motion of small particles on the surface; Second, the coalescence of droplets as a result of individual growth bringing them into mutual contact; Third, nucleation of new droplets in voids left by coalescence. This produces a structure of larger droplets with a narrow distribution of sizes and many smaller droplets dispersed in the voids between them. As deposition progresses, mean particle radius increases linearly with time, while the surface coverage increases to a saturation level of around 55 %, at which point the mean inter-particle spacing for the larger sizes stabilizes. These generic models take no account of specific properties for any particular material, beyond the assumed growth kinetics, but results are consistent with the condensation of various vapors.

7.2 Fabrication

Grating patterns were etched into 0.25 mm thick PET substrates by focused ion beam (FIB) milling. To prevent charging during the FIB milling process, the PET was first coated by evaporation with ~30 nm of gold; A symmetric, nominally rectangular grating profile was maintained over periods ranging from $P = 200$ to 1600 nm; Gratings each covered a 25 µm × 25 µm area and were etched to a depth of 120 nm. (The FIB process inevitably produces lines with imperfectly vertical sidewalls and rounded corners but these deviations from the ideal rectilinear geometry of fig. 7.1a are ignored as they occur on lateral scales smaller than the nanoparticle diameters.) An unpatterned reference domain of the same size was prepared by rastering the focused ion beam over the entire area to replicate any (sub)nanoscale surface roughness and gallium implantation introduced by the FIB process in the grating domains. Remaining parts of the gold anti-charging layer were then removed by wet etching (in KI/I_2, followed by sonication in isopropyl alcohol, rinsing in deionized water and baking at 80 °C for 5 min) and the PET was coated with a 250 nm mass-thickness of gallium (as measured on a quartz microbalance) by resistance evaporation under high vacuum (~5×10^{-6} mbar) from a source of 6N purity.

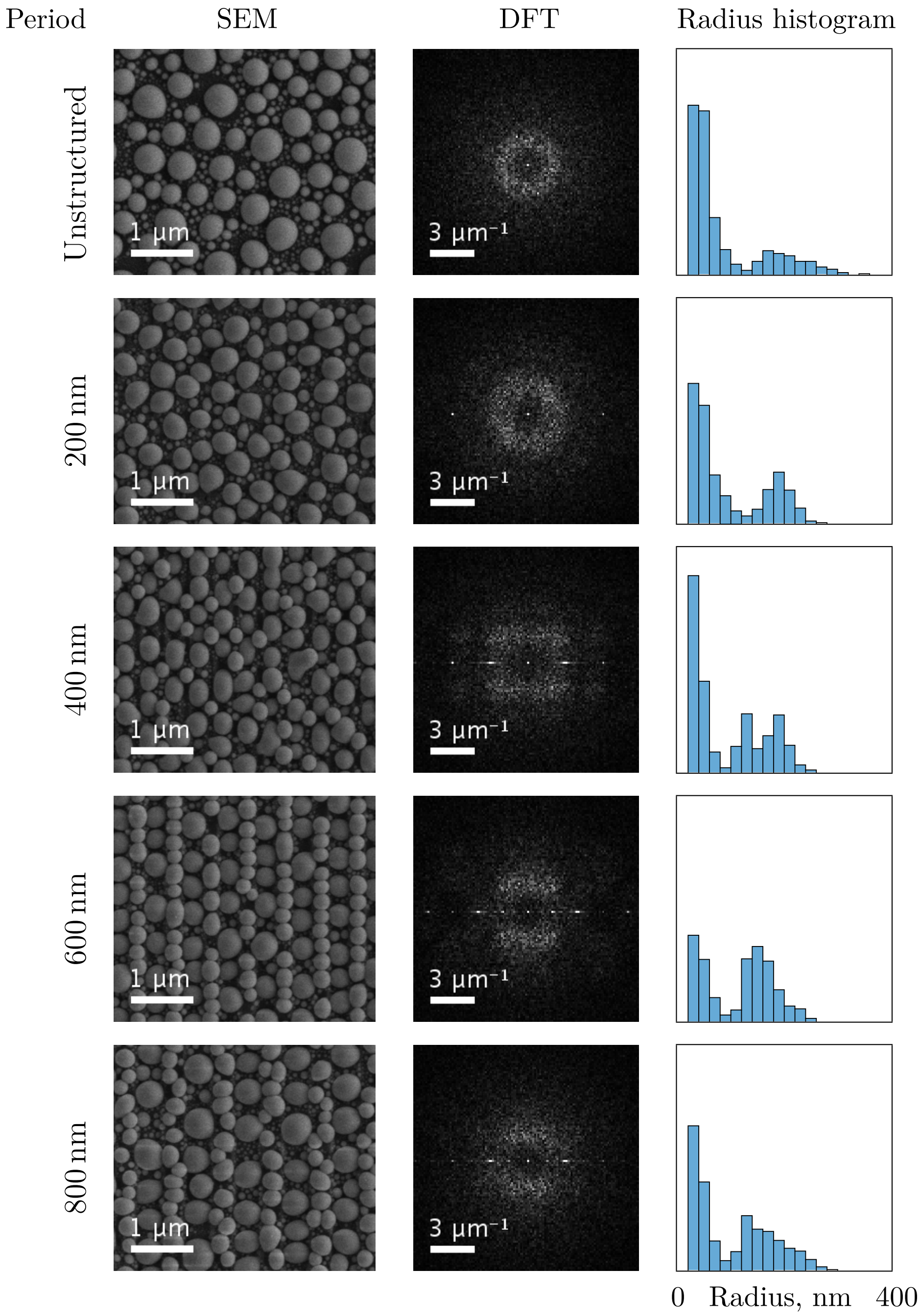

Figure 7.2: Gallium nanoparticle growth on PET grating substrates. Scanning electron microscope images (left) with corresponding DFT images (center) and particle diameter histograms (right) of Ga nanoparticles (250 nm mass-thickness deposition) grown on PET substrates patterned with symmetric, 120 nm deep rectangular gratings of varying period (as labelled), and for reference, an unstructured PET substrate (top row). DFT images and histograms are derived from SEM images encompassing 8.5 × 7.4 µm sample domains, truncated sections of which are shown; DFT images are deliberately over-saturated to reveal the diffuse features; particle diameters <30 nm are not resolved in histogram evaluations, where the vertical scale is the relative number density. Continued overleaf.

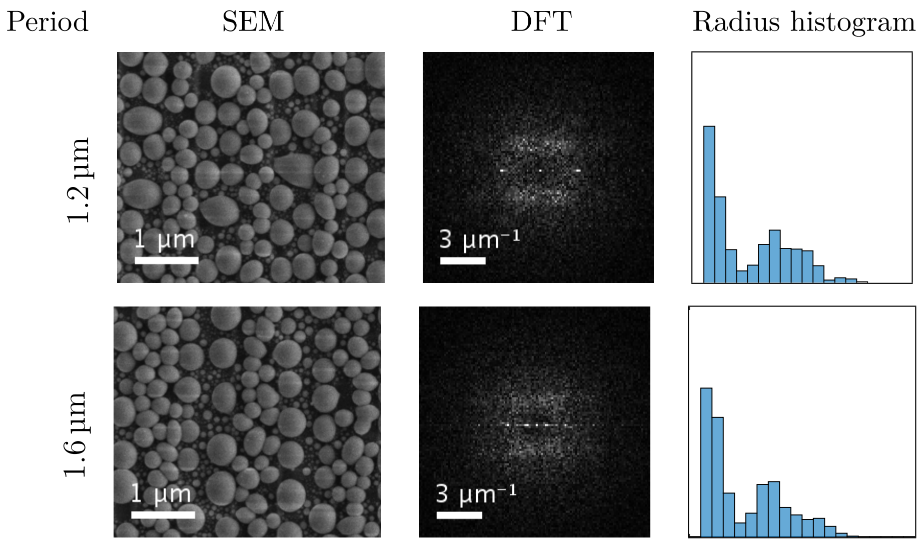

Figure 7.2: Gallium nanoparticle growth on PET grating substrates (cont.)

7.3 Results

The presence of a substrate surface relief structure has a profound effect on the distribution of gallium nanoparticles then formed, as illustrated (to the naked eye) by the sequence of scanning electron microscope (SEM) images in the left hand column of Fig. 7.2. This templated ordering of nanoparticle assembly was quantitatively characterized on the basis of these images via a Fourier decomposition: First (using the Fiji image processing package[194]), a median filter was applied to de-speckle the SEM images, and an intensity-thresholded local thickness algorithm was then employed to "flatten" them, compensating for the fact that (by the nature of the secondary electron imaging process) particles located within the slots of the grating structure appear darker than those located on the ridges. This important correction ensures that subsequent analyses of the nanoparticles' in-plane positional order are not distorted by imaging artefacts related to the out-of-plane height/depth (and aspect ratio) of substrate relief features. Binary maps of the nanoparticles are thus produced, from which discrete Fourier transform (DFT) images are obtained. These transforms, shown in the center column of fig. 7.2, generally have two major components: a set of sharp maxima arranged in a horizontal line, reflecting nanoparticle order in the direction parallel to the grating vector (perpendicular to the lines), and a diffuse "halo" representative of the particle distribution over all in-plane directions. As one would expect, only the latter halo is present when the substrate is unstructured - it has a radius corresponding to the mean center-to-center distance $\overline{\mathbf{d}}_0$ ~320 nm between large particles in the film, which have a bimodal size distribution (right hand column of fig. 7.2) characteristic of the liquid-phase growth/coalescence process.[193]

To the naked eye, the shortest period ($P = 200\,\mathrm{nm}$) grating does not obviously disrupt this random positional and bimodal size distribution. However, while the

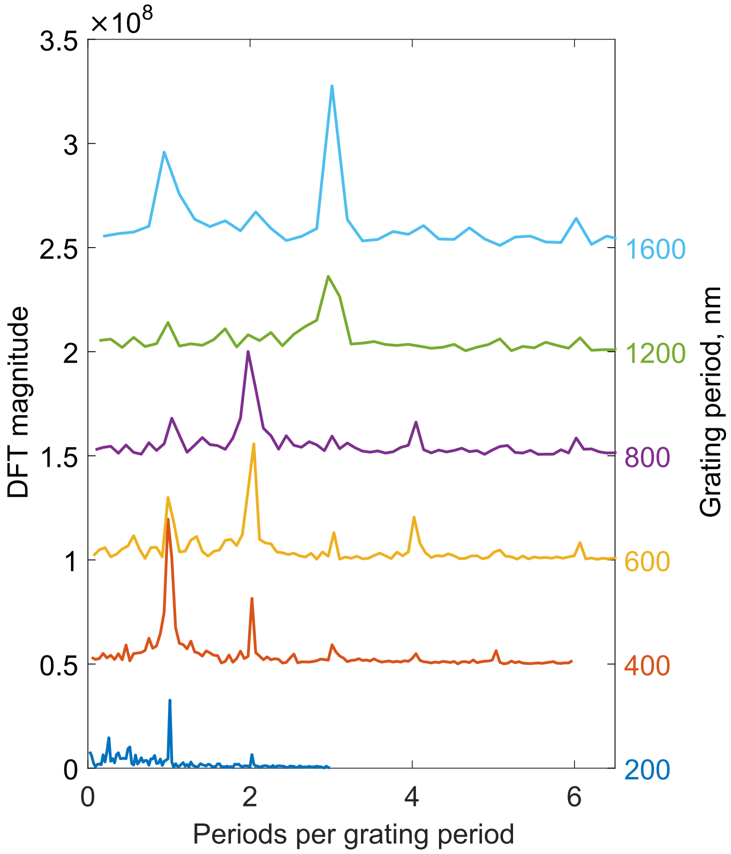

Figure 7.3: DFT magnitudes aligned with grating axis for gratings of depth 105nm and period 0.2 to 1.6 µm with nominal deposited gallium thickness of 250 nm. The values are scaled in the horizontal axis by the period of each grating for simplified comparison of DFT maxima.

DFT halos are almost indistinguishable, the transform for the grating substrate does present a pair of bright maxima on either side of the origin, indicating that some periodic order is imposed (i.e., that there is a tendency for particles to nucleate on the raised ridges of the grating), and the large diameter tail of the size distribution is truncated. The larger gratings (all having periods $P > \overline{\mathbf{d}}_0$ the mean unstructured-substrate center-to-center particle spacing, and slot/ridge widths $\geq \overline{\mathbf{r}}_0$ the mean unstructured-substrate particle diameter) have a more pronounced effect on nanoparticle distribution. At $P = 400\,\mathrm{nm}$, periodic order in the direction of the grating vector is immediately apparent in the SEM image and manifested in the DFT by axial peaks at positions corresponding to the grating period and half-period (the former being dominant, as illustrated in fig. 7.3, which presents axial cross-sections of DFT amplitude). The halo is also "squared off," indicating the imposition of the periodic order along the grating slots/ridges - this points to the emergence of some directional anisotropy in the interactions between neighboring particles during growth, i.e., some decoupling of the nucleation and coalescence kinetics between adjacent slots and ridges. These behaviors are even more

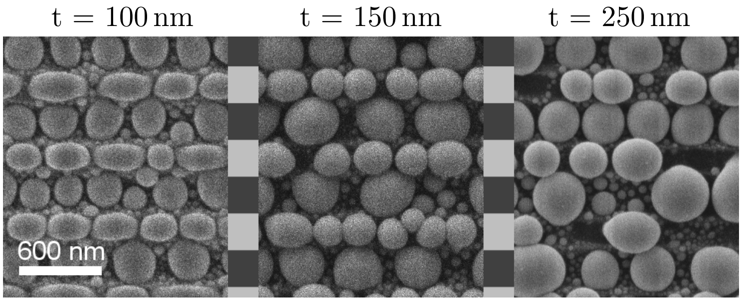

Figure 7.4: Gallium nanoparticle ordering on grating structures for varying gallium thickness. Shown are SEM images of gratings of period 600 nm and depth 120 nm (aspect ratio height:width 2:5) with varying gallium mass-thickness t. The gratings for each image are aligned according to the shaded pattern with unpatterned areas in light grey and milled areas in dark grey.

prominent for the 600 nm grating, which has a period very close to $2\overline{\mathbf{d}}_0$. As such, particles naturally coalesce either in a slot or on a ridge of the structure, as reflected by the dominance of the half-period peak in the corresponding DFT cross-section of fig. 7.3. The particle size distribution is also maximally perturbed at $P = 600\,\mathrm{nm}$, with a pronounced increase in the relative number density of larger particles having diameters around $P/2$. At still larger grating periods, apparent order (as to the naked eye from SEM images) diminishes and/or becomes more complex: The dominance of the half-period peak in the DFT cross-section is preserved at $P = 800\,\mathrm{nm}$, but disappears at 1200 and 800 nm as $P/2$ approaches and exceeds $\overline{\mathbf{d}}_0$.

I have focused on a particular combination of grating etch depth (120 nm) and gallium mass-thickness (250 nm). At lower mass-thickness $\overline{\mathbf{d}}_0$ decreases and the optimal positional templating is achieved by shorter period gratings (see fig. 7.4). For a given mass-thickness of Ga, shallower gratings exert weaker control over the positional order of particles; order is maintained by deeper gratings, but the secondary electron image brightness/contrast mismatch between particles in slots and on ridges becomes prohibitive to a meaningful DFT analysis. Hence, neither the shallower nor deeper gratings are included in the full image processed study.

The effect of a surface-relief nanostructured substrate on the arrangement of nanoparticles as they are grown may be understood through consideration of the fact that they will seek to minimize the surface free energy. For the avoidance of discontinuities in the contact angle (between gallium and PET - a function of the solid/liquid/vapor interfacial free energies[195]) and/or in the truncated spherical form of the gallium surface, particles accrete preferentially on flat areas of the substrate, rather than wrapping over the sharp edges of the slots, even when the change in substrate surface height (grating etch depth) is somewhat smaller than the particle size. (The directionality of gallium deposition largely precludes nucleation on the near-vertical sidewalls of the grating slots.) Within the confines of this surface structural template, particle growth during PVD proceeds via the self-organized nucleation and coalescence mechanisms described above to produce

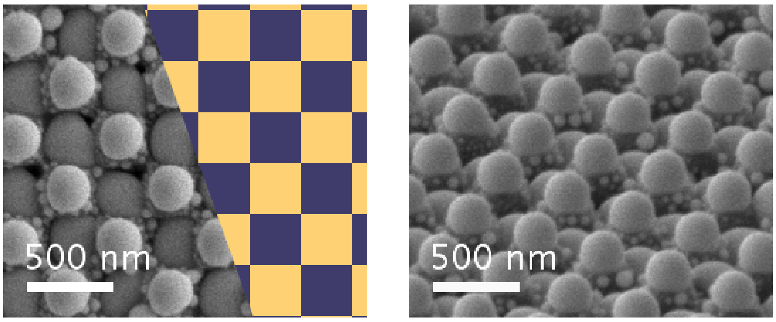

(a) Plan view with pattern overlay

(b) Oblique view

Figure 7.5: Gallium nanoparticle ordering on 'checkerboard' type structures. (a) Plan view SEM image with overlay depicting the milled patttern with raised and milled areas denoted by yellow and blue respectively. (b) Oblique SEM of the same. The pattern has a 600nm period and a depth of 120nm with a nominal gallium thickness of 150nm.

the ordered assemblies such as in fig. 7.2. Substrate surface relief patterns may of course be designed to produce a variety of particle arrangements (of interest for example, for their ensemble optical/plasmonic properties) as illustrated in fig. 7.5, where the self-organization is almost entirely suppressed by a checkerboard substrate that imposes 2D positional and close particle size control.

7.4 Effect of the oxide layer

Gallium's ability to form and sustain a thin (~3 nm) solid oxide surface coating, even on the liquid under high vacuum,[196] should be noted here. Such a layer is likely to form on the nanoparticles during PVD (by reaction between the metal and substrate-adsorbed oxygen and water vapor) and may indeed account for the observed aspherical shape of some particles and the failure of some touching particles to coalesce - the latter effect in particular, resulting in a surface coverage saturation level of ~64 % somewhat higher than the 55 % expected from vapor condensation models.[193]

7.5 Deposition on unstructured PET

When gallium is deposited on unstructured PET, nanoparticles with a diameter of around 100 nm form. This dimension is considerably lower than the 250 nm film mass-thickness. Hence the deposited nanoparticles must be stacked vertically away from the surface. This highly anomalous behaviour may be enabled by the barrier formed by the oxide layer. It is interesting to note that this occurs only in the case of the unstructured substrate; any patterning results in the formation of much larger droplets. This is understood to be caused by gallium ion implantation of the

PET. As this passes outside the scope of templated assembly, these considerations are explored in appendix C.

7.6 Conclusion

I have demonstrated the facility to guide nanoparticle self-organisation during PVD film growth via substrate patterning, for the first time to the best of my knowledge. The quality of ordering produced is strongly dependent on the relative dimensions of the substrate patterning and typical nanoparticle size, each of which may be precisely engineered. Optimum ordering was arrived at for gratings with a pitch approximately double the typical interparticle spacing. As a result this methodology may be scaled up or down considerably to meet the needs of differing applications, particularly in view of gallium's broad-band plasmonic properties. The method may be extended to function with other materials by depositing onto substrates at temperatures in excess of the evaporant melting point. Further study could include deeper investigation of two-dimensional patterns, aperiodic structures and hybridised substrate media for increased control of ordering. As the necessity of production of smaller structures across larger areas becomes ever more apparent, innovation in nanomanufacturing methods is increasingly urgent. This result may hence prove useful as an early step into the realm of self-assembled plasmonic structure engineering.

Chapter 8

Conclusion

8.1 Summary

I have demonstrated for the first time the enhancement of gallium's inherent phase-change nonlinear reflective properties using a metasurface structure. Designed and optimised with the aid of computational modelling of optical properties, the metamaterial enhances this effect in gallium considerably by two experimental metrics: First, using a nonlinear figure of merit based on reflectivity contrast and the intensity required to excite it, an enhancement of a factor of > 4 is seen relative to an experimental test with a similar, but unstructured, geometry. The enhacement would be greater still relative to a plane gallium surface. Second, the difference between the minimum temperature at which significant excitation is seen and the melting point is enhanced by a factor > 6. These results should however be viewed with the caveat that the experiment was conducted using a single sample (though it was thoroughly repeated with that sample) and as such repeatability is yet to be fully tested. The specific structure used, a 'gap plasmon' based trilayer absorber type geometry, produces increased absorption of incident light at target wavelengths. The composite surface retains these characteristics and allows deliberate, illumination based switching of the absorption for enhanced reflectivity contrast. The metamaterial also has the capacity to display optical properties with a hysteretic response to ambient temperature in the absence of a pump laser.

I investigated multiple methods of modelling the phase dynamics of the gallium component of the composite surface. The laser heating of the metamaterial absorber was analytically modelled, predicting the threshold at which the nonlinear effect arises using thermodynamic flow considerations only and concluding that direct heating may be insufficient to cause the observed nonlinear effects alone and another mechanism, such as a direct photonic excitation mechanism posited by other authors, could contribute. I tested a previously presented photonic excitation based model and a finite element method, concluding the former is insufficient to describe our system while full finite element treatment is prohibitively computationally expensive. Hence in collaboration with a colleague I begin development of a novel technique integrating the photoexcitation based treatment into a cellular automaton. This method combines a previously tested excitation model with a phenomenological model of the propagation of excited states within a gallium surface. Subsequent to my departure, development of that model has been left to my colleague.

I investigated a nanoimprint process based on the mechanical compression of a liquid metal such that it will flow into indentations in an imprint mask. Despite wetting theory predicting that the metal would be excluded from nanoscale indentations, using a custom-built nanoimprint system I have shown for the first time that elemental gallium may enter sub-micron pitch indentations in a polymer with a high depth to width ratio. I gave a first demonstration of the thermal switching of the optical properties of a nanoimprinted gallium grating in glass, evaluating its performance by comparison with simulations. It appears to show a favourable level of reproduction of the predicted properties, though a broad-band slight depression of reflectivity was evident. I have shown computationally some of the possibilities enabled by gallium nanoimprint-based phase change metamaterials, including a colour-switching material based on indented ring slot resonators and a metasurface that develops reflectivity of different colours depending on gallium phase and incident radiation polarisation.

I have demonstrated, for the first time to the best of my knowledge, the use of substrate patterning to guide the nanoscale ordering of thin films of liquid metallic nanoparticles as they form during the process of thermal evaporation. Using Fourier analysis and other image processing techniques I have shown that for grating type patterns quality of ordering is maximised when the periodicity of patterning is close to the natural interparticle spacing on an unstructured surface. Quality of ordering is also optimised by choosing patterns of depth greater than or equal to the natural particle radius. I further show that quite precise and consistent ordering of both the relative position and the size of grown nanoparticles may be obtained by introducing periodicities in both axes of the plane.

As a part of the described studies I investigated the growth mode of vapor deposited gallium on a variety of substrates, providing new reference information for studies of this type. I additionally tested some characteristics of deposited gallium nanoparticles and of a gallium-aluminium composite formed by infiltration of liquid gallium into solid gallium via grain boundary penetration. Finally I characterised the effect of gallium ion milling on absorption in polyethylene terephthalate plastic. Whille none of these smaller investigations was broad enough to be considered for publication alone, the sum is nonetheless interesting.

8.2 Outlook

Phase change based tuning of surface properties is an increasingly popular topic in the field of metamaterials, with chalcogenide glass based phase control being behind some of the key advances in reconfigurable metamaterials in recent years. Gallium based reconfiguration offers a new take on this idea, introducing the possibility of phase change switching of metallic components of a metasurface at easily accessible temperatures, something not otherwise possible outside of extremely high or low temperatures. This presents a notable opportunity as I have only developed a few simple examples of this kind of metamaterial - much potential remains to be tapped. The particular example of the switchable absorber could be applied as a plasmonic sensor, infrared radiation sensor, temperature sensor or a saturable absorber for (for example) a free space laser. On the other hand, any mechanism harnessing the phase change nonlinearity of gallium (or, indeed, most phase change mechanisms) would be required to either be explicitly environment responsive / temperature sensing or precisely temperature controlled.

Nanoimprint manufacturing is a particularly exciting area, offering the future promise of industrial scale production of metasurface patterns. While application of this processing method is subject to the same caveats as other phase-change devices, capitalising on the successes on this front could aid the goal of lower cost fabrication of this kind. The current iteration of the manufacturing process incorporates focussed ion beam milling, which has a side effect of doping the milled area with gallium ions. This has a detrimental effect on the optical properties of resulting structures. However, observations of improvements in adhesion between gallium and structured surfaces caused by this doping show that by deliberate control of the effect we may yet apply it in a beneficial manner. Further experimental investigation is required before the extent to which doping may be applied beneficially can be determined. In the meantime other nanolithography processes not requiring the use of a gallium ion beam (such as photolithography or electron beam lithography) may be used without compromising the optical properties of the dilectric medium.

While full simulation of phase dynamics in a metamaterial structure is a hard problem, there is promise in the possibility of developing a multi-state cellular automaton model. The model has already shown some success in qualitative reproduction of observed phenomena, including low-power millisecond pulse excitation of melting as well as high-power femtosecond pulse excitation. A consequence of the model's two-dimensional nature is that it is trivial to extend to periodic structures such as gratings and could hence be used in the characterisation of such more complex geometries. The cellular automaton is not limited to functioning in two dimensions and could be extended to a fully three-dimensional treatment with the greater flexibility that provides. The next step for this work is the phenomenological reproduction of experimental results in order to gain some insight into the microscopic mechanisms behind this phase change.

In my work with the deposition of gallium onto structured substrates I have demonstrated a degee of control of the growth of metallic films, which could be very useful for the development of bottom-up manufacturing techniques. This is to the best of my knowledge the first example of such a mechanism. Development of this technique to enable finer control is a promising direction for further work, particularly if it can be shown that phase switching of optical properties is still achievable in the resulting nanoparticle distributions. The control of growth can in theory be applied to any substrate / evaporant combination which results in deposition in the Volmer-Weber mode. However this must be considered in the knowledge that any controlled nanoparticle growth cannot differ to a large extent from the natural ordering of such nanoparticles, such as inclusion of very large nanoparticles or large spaces between them.

8.3 Final word

Gallium based metamaterials are a wholly new area of research and I have only scratched the surface. My study and development of these has been rewarding in itself and has led to other discoveries related to this unusual element such as the capacity for higher than expected levels of supercooling in nanoparticles and gallium that has infiltrated other metals through grain boundary penetration and the capacity for nanoparticles to align with templated structures. The opportunity is now open to investigate these discoveries in greater depth.

Over the course of my research I have made considerable strides in the application of gallium in tunable and switchable metamaterials. This represents a foundation that can be built upon.

Appendices

Appendix A

Material parameters

Analytical and numerical models employed fixed values for the relative permittivities ϵ_r $(= i\epsilon_r' + \epsilon_r'')$ of transparent dielectric media in the visible to NIR wavelength range:

- Glass $\epsilon_r = 2.25 + 0i$
- Silicon nitride $\epsilon_r = 4.00 + 0i$

Complex parameters for gallium and gold tabulated below are taken from:

- Solid Ga: Kofman, et al., Phys. Rev. B 16, 5216 (1977)
- Liquid Ga: Teshev & Shebzukhov, Opt. Spectrosc. (USSR) 65, 693 (1988)
- Gold: Palik, "Handbook of Optical Constants of Solids" (1998)

Table A.1: Relative permittivites of liquid and solid α-phase crystalline gallium

	Liquid gallium		Solid α-crystalline gallium					
	Isotropic		a-axis		b-axis		c-axis	
λ (nm)	ϵ_r'	ϵ_r''	ϵ_r'	ϵ_r''	ϵ_r'	ϵ_r''	ϵ_r'	ϵ_r''
442.75	-30.201	9.326	-5.508	2.175	-4.578	2.175	-3.681	2.172
459.3	-31.864	10.295	-6.166	2.45	-5.08	2.478	-4.155	2.468
475.85	-33.54	11.298	-6.931	2.770	-5.692	2.866	-4.65	2.834
492.4	-35.256	12.335	-7.653	3.296	-6.194	3.394	-5.118	3.357
508.95	-36.983	13.405	-8.327	4.057	-6.577	4.101	-5.583	4.094
525.5	-38.725	14.508	-8.913	5.004	-6.796	4.717	-5.879	4.815
542.04	-40.484	15.643	-9.391	6.177	-6.825	5.182	-5.921	5.378
558.6	-42.255	16.80	-9.657	7.139	-6.86	5.471	-5.799	5.849
575.15	-44.036	18.009	-9.666	8.027	-6.761	5.575	-5.679	6.483
591.7	-45.828	19.239	-9.468	8.827	-6.581	5.525	-5.514	7.177
608.25	-47.625	20.498	-9.217	9.527	-6.484	5.456	-5.351	7.825
624.8	-49.43	21.79	-9.0591	10.128	-6.613	5.487	-5.243	8.314
641.35	-51.238	23.112	-8.958	10.663	-6.898	5.568	-5.185	8.682
657.9	-53.047	24.463	-8.887	11.202	-7.243	5.668	-5.165	9.006
674.45	-54.858	25.844	-8.852	11.761	-7.655	5.79	-5.185	9.293
691	-56.667	27.253	-8.843	12.295	-8.153	5.924	-5.243	9.528

Table A.1: Relative permittivites of liquid and solid α-phase crystalline gallium

	Liquid gallium		Solid α-crystalline gallium					
	Isotropic		a-axis		b-axis		c-axis	
λ (nm)	ϵ_r'	ϵ_r''	ϵ_r'	ϵ_r''	ϵ_r'	ϵ_r''	ϵ_r'	ϵ_r''
707.55	-58.472	28.692	-8.846	12.827	-8.665	6.078	-5.31	9.793
724.1	-60.276	30.16	-8.849	13.377	-9.137	6.254	-5.367	10.138
740.65	-62.073	31.656	-8.881	13.932	-9.637	6.463	-5.45	10.518
757.2	-63.865	33.179	-8.932	14.487	-10.164	6.695	-5.55	10.925
773.75	-65.647	34.731	-8.989	15.038	-10.702	6.947	-5.647	11.359
790.3	-67.421	36.31	-9.04	15.58	-11.239	7.211	-5.725	11.822
806.85	-69.186	37.917	-9.069	16.106	-11.758	7.477	-5.761	12.313
823.4	-70.94	39.551	-9.073	16.612	-12.250	7.751	-5.75	12.839
839.95	-72.682	41.210	-9.077	17.100	-12.733	8.047	-5.711	13.407
856.5	-74.411	42.898	-9.073	17.577	-13.211	8.355	-5.639	13.995
873.05	-76.126	44.611	-9.0591	18.044	-13.69	8.666	-5.532	14.575
889.6	-77.828	46.35	-9.032	18.504	-14.173	8.97	-5.384	15.123
906.15	-79.515	48.115	-8.997	18.952	-14.654	9.282	-5.198	15.657
922.7	-81.186	49.905	-8.955	19.39	-15.133	9.599	-4.985	16.170
939.25	-82.841	51.722	-8.906	19.815	-15.616	9.916	-4.762	16.652
955.8	-84.481	53.563	-8.846	20.227	-16.103	10.236	-4.525	17.099
972.35	-86.105	55.429	-8.781	20.618	-16.588	10.558	-4.256	17.510
988.9	-87.710	57.319	-8.708	20.993	-17.071	10.885	-3.96	17.893
1005.45	-89.3	59.234	-8.627	21.356	-17.556	11.213	-3.648	18.245
1022	-90.872	61.173	-8.54	21.715	-18.044	11.541	-3.329	18.571
1038.55	-92.426	63.137	-8.445	22.071	-18.533	11.868	-3.011	18.876
1055.0	-93.963	65.125	-8.346	22.43	-19.029	12.192	-2.702	19.161
1071.65	-95.481	67.135	-8.243	22.797	-19.53	12.512	-2.415	19.431
1088.2	-96.984	69.17	-8.141	23.173	-20.033	12.827	-2.143	19.673
1104.75	-98.468	71.227	-8.041	23.554	-20.536	13.141	-1.883	19.891
1121.3	-99.935	73.307	-7.935	23.935	-21.04	13.452	-1.63	20.085
1137.85	-101.385	75.41	-7.825	24.311	-21.544	13.762	-1.377	20.256
1154.4	-102.818	77.536	-7.703	24.678	-22.047	14.072	-1.121	20.407
1170.95	-104.233	79.683	-7.565	25.030	-22.551	14.383	-0.854	20.539
1187.5	-105.632	81.853	-7.411	25.364	-23.053	14.695	-0.574	20.655
1204.05	-107.015	84.046	-7.233	25.672	-23.555	15.01	-0.272	20.757
1220.6	-108.382	86.259	-7.041	25.965	-24.045	15.325	0.0437	20.849
1237.15	-109.733	88.494	-6.849	26.257	-24.516	15.639	0.342	20.934
1253.7	-111.069	90.75	-6.63	26.52	-25.001	15.955	0.614	21.010
1270.25	-112.39	93.027	-6.368	26.728	-25.513	16.257	0.867	21.083
1286.8	-113.697	95.325	-6.065	26.882	-26.055	16.556	1.092	21.148
1303.35	-114.989	97.643	-5.71	26.981	-26.624	16.853	1.265	21.201
1319.9	-116.268	99.981	-5.294	27.018	-27.227	17.143	1.388	21.244
1336.45	-117.534	102.341	-4.887	27.015	-27.850	17.452	1.522	21.285
1353	-118.786	104.719	-4.434	26.962	-28.528	17.786	1.675	21.327
1369.55	-120.027	107.116	-4.004	26.867	-29.21	18.125	1.823	21.361
1386.1	-121.256	109.533	-3.645	26.741	-29.852	18.459	1.951	21.371
1402.65	-122.473	111.969	-3.306	26.577	-30.481	18.8	2.068	21.37
1419.2	-123.68	114.424	-3.056	26.375	-31.118	19.134	2.181	21.382
1435.75	-124.876	116.897	-2.881	26.123	-31.754	19.46	2.293	21.417

Table A.1: Relative permittivites of liquid and solid α-phase crystalline gallium

	Liquid gallium		Solid α-crystalline gallium					
	Isotropic		a-axis		b-axis		c-axis	
λ (nm)	ϵ_r'	ϵ_r''	ϵ_r'	ϵ_r''	ϵ_r'	ϵ_r''	ϵ_r'	ϵ_r''
1452.3	-126.063	119.387	-2.774	25.84	-32.393	19.785	2.399	21.452
1468.85	-127.24	121.896	-2.754	25.529	-33.044	20.106	2.502	21.468
1485.4	-128.408	124.422	-2.821	25.164	-33.692	20.414	2.6	21.466
1501.95	-129.568	126.965	-2.948	24.794	-34.353	20.728	2.687	21.471
1518.5	-130.72	129.525	-3.115	24.459	-35.036	21.073	2.753	21.510
1535.05	-131.864	132.101	-3.351	24.129	-35.747	21.43	2.798	21.59
1551.6	-133.002	134.694	-3.617	23.804	-36.463	21.806	2.835	21.654
1568.15	-134.133	137.301	-3.919	23.489	-37.185	22.212	2.874	21.669
1584.7	-135.257	139.925	-4.259	23.178	-37.914	22.638	2.907	21.664
1601.25	-136.376	142.563	-4.602	22.87	-38.645	23.07	2.929	21.673
1617.8	-137.49	145.216	-4.942	22.557	-39.390	23.523	2.938	21.699
1634.35	-138.598	147.883	-5.3	22.247	-40.14	23.987	2.935	21.73
1650.9	-139.703	150.563	-5.695	21.949	-40.872	24.437	2.921	21.763
1667.45	-140.803	153.257	-6.132	21.645	-41.581	24.873	2.887	21.798
1684	-141.899	155.962	-6.597	21.346	-42.282	25.306	2.851	21.835
1700.55	-142.991	158.682	-7.083	21.074	-42.996	25.742	2.834	21.867
1717.1	-144.08	161.413	-7.610	20.815	-43.712	26.173	2.827	21.9
1733.65	-145.166	164.155	-8.16	20.57	-44.433	26.605	2.823	21.928
1750.2	-146.249	166.907	-8.71	20.346	-45.161	27.042	2.812	21.946
1766.75	-147.329	169.670	-9.243	20.14	-45.908	27.48	2.794	21.956
1783.3	-148.407	172.444	-9.803	19.946	-46.664	27.917	2.770	21.959
1799.85	-149.483	175.226	-10.354	19.777	-47.408	28.369	2.742	21.962
1816.4	-150.556	178.018	-10.875	19.64	-48.127	28.838	2.705	21.961
1832.95	-151.628	180.817	-11.375	19.53	-48.826	29.321	2.661	21.955
1849.5	-152.698	183.625	-11.873	19.443	-49.515	29.812	2.613	21.95
1866.05	-153.765	186.438	-12.391	19.375	-50.2	30.303	2.560	21.951
1882.6	-154.831	189.261	-12.946	19.321	-50.884	30.789	2.503	21.962
1899.15	-155.896	192.087	-13.52	19.285	-51.558	31.277	2.439	21.98
1915.7	-156.959	194.920	-14.119	19.268	-52.233	31.766	2.37	22.001
1932.25	-158.021	197.759	-14.755	19.268	-52.917	32.256	2.297	22.023
1948.8	-159.08	200.602	-15.437	19.283	-53.624	32.741	2.218	22.044
1965.35	-160.138	203.449	-16.157	19.318	-54.338	33.228	2.137	22.067
1981.9	-161.194	206.299	-16.914	19.368	-55.061	33.713	2.051	22.091
1998.45	-162.247	209.152	-17.711	19.434	-55.792	34.198	1.96	22.118
2015	-163.3	212.008	-18.552	19.516	-56.535	34.680	1.864	22.146

Table A.2: Relative permittivity of gold

λ (nm)	ϵ_r'	ϵ_r''
188	0.2271	3.0413
192	0.2952	3.1758
195	0.2925	3.2857
199	0.2039	3.3277
203	0.1382	3.3968

207	-0.0104	3.3904
212	-0.1325	3.51
216	-0.2338	3.6062
221	-0.3463	3.7102
226	-0.4155	3.8252
231	-0.551	3.8922
237	-0.6169	4.055
243	-0.7445	4.1633
249.	-0.8913	4.3384
255	-1.0804	4.4901
262	-1.2365	4.7223
269	-1.3464	4.9763
276	-1.3665	5.2824
284	-1.3323	5.4949
292	-1.3068	5.5964
301	-1.2274	5.7803
311	-1.2425	5.7926
320	-1.2308	5.8458
332	-1.3553	5.5737
343	-1.3102	5.5382
354	-1.232	5.597
368	-1.4006	5.6092
382	-1.6049	5.6444
397	-1.6494	5.7389
413	-1.7022	5.7174
431	-1.6922	5.6492
451	-1.759	5.2826
471	-1.7027	4.8444
496	-2.2783	3.8126
521	-3.9462	2.5804
549	-5.8421	2.1113
582	-8.1127	1.6605
617	-10.6619	1.3742
660	-13.6482	1.0352
705	-16.8177	1.0668
756	-20.6102	1.2718
821	-25.8113	1.6266
892	-32.0407	1.9254
984	-40.2741	2.794
1090	-51.0496	3.861
1220	-66.2185	5.7015
1390	-90.4265	8.1863
1610	-125.3505	12.5552
1940	-189.042	25.3552

Appendix B

Method for the derivation of perceived colour from reflectance spectra

For certain experimental and numerical simulation setups it is impossible to directly obtain the colour of a sample. Therefore, where RGB colour data is needed, it is necessary to derive it from measured spectrum data. A method for doing this using the CIE XYZ colour space standard[197] is described here in step-by-step format.

1. A spectral power distribution of the sample is obtained. For the purposes of this demonstration normal incidence reflectivity data for Au is utilised (data extracted from[198]).

2. To obtain a realistic visible colour, real lighting conditions must be defined. The spectrum is hence modulated by the emission spectrum of a black body 'lamp' by simple multiplication (fig. B.1). Here a 5600k photographic standard black body spectrum is used.

3. The resultant spectrum is in turn used to modulate the CIE XYZ spectra (fig. B.2). Steps 2 and 3 are described in alternate equation format in eqs. B.1 through B.3.

4. The total of each of each curve is integrated to obtain the values X, Y and Z.

5. A matrix transformation is used to convert the XYZ values into more readily utilised RGB values using Eq. B.4. Fig. B.3 shows the obtained RGB colour for the Au spectrum.

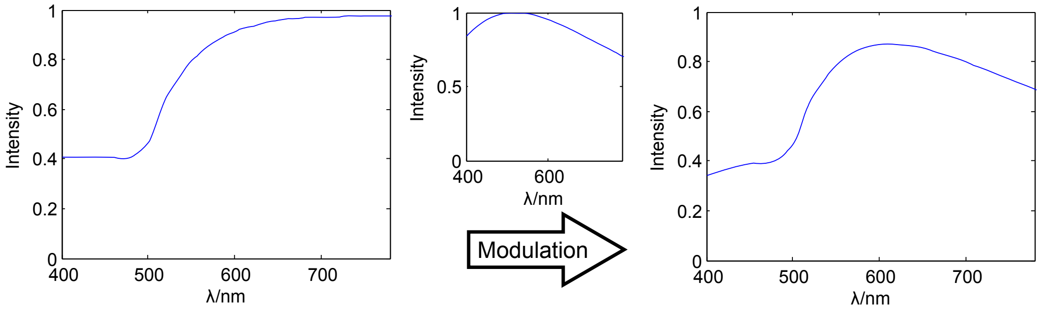

Figure B.1: Modulation of Au spectrum (left) with black body spectrum (centre) to produce lit Au spectrum.

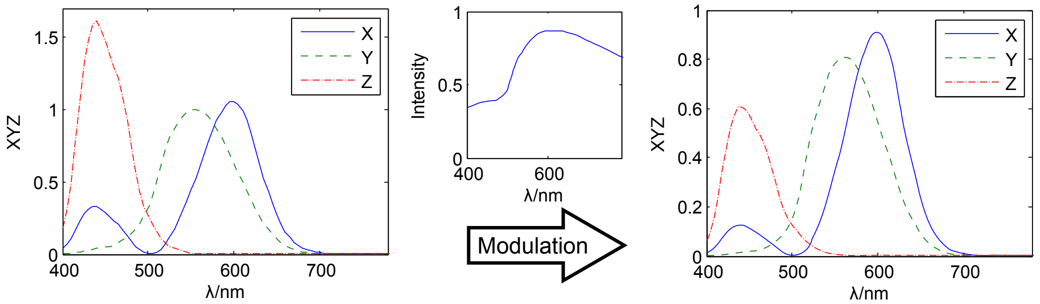

Figure B.2: Modulation of CIE XYZ standard spectra (left) with lit Au spectrum (centre) to produce lit Au XYZ spectra.

Figure B.3: RGB colour for gold reflectivity at normal incidence under 5600K standard photographic lighting. Red, green and blue values portrayed are 255, 195 and 102 respectively.

$$X = \int_{380}^{780} I(\lambda)\, B(\lambda)\, x(\lambda)\, d\lambda \tag{B.1}$$

$$Y = \int_{380}^{780} I(\lambda)\, B(\lambda)\, y(\lambda)\, d\lambda \tag{B.2}$$

$$Z = \int_{380}^{780} I(\lambda)\, B(\lambda)\, z(\lambda)\, d\lambda \tag{B.3}$$

$$\begin{bmatrix} R \\ G \\ B \end{bmatrix} = \begin{bmatrix} 0.49 & 0.31 & 0.2 \\ 0.17697 & 0.81240 & 0.01063 \\ 0.00 & 0.01 & 0.99 \end{bmatrix} \begin{bmatrix} X \\ Y \\ Z \end{bmatrix} \tag{B.4}$$

Appendix C

Effect of prior FIB milling of a PET substrate on thermal evaporation of gallium

One planned manufacturing process required the FIB milling of a PET (polyethylene terephthalate) substrate before thermal evaporation of gallium onto that substrate. During the FIB manufacturing process, the surface is roughened and gallium ions are implanted into the substrate. Hence, trials were conducted into the possible effects of this on the subsequently deposited gallium films, with interesting results. A sample of 0.25 mm thick biaxially oriented PET was prepared for FIB millling by deposition of a thin 20 nm layer of gold. An array of $30 \times 30\,\mu\text{m}$ squares was milled with exponentially increasing FIB dosages from 0.41 up to $20\,\text{mC}\,\text{cm}^{-2}$. The gold layer was then chemically etched away and a 250 nm mass-thickness of gallium was deposited onto the surface via thermal evaporation. Fig. C.1 shows in a series of selected SEM images of these areas how the perturbation varies across two orders of magnitude of gallium ion dosage.

The distribution of nanoparticles goes through three regimes in the range tested:

- At zero dosage as already noted the nanoparticles may grow in vertical stacks, which is to the best of the author's knowledge a form of nanoparticle growth not previously seen. Until such a time as a more thorough treatment of this phenomenon is brought, I must conclude that this is caused by oxidation of nanoparticle surfaces enabling separate growth of nanoparticles that appear to be in mutual contact.
- Low-level dosage ($0.41\,\text{mC}\,\text{cm}^{-2}$) results in a patchwork of regions with a small incidence of vertical stacking still observed. Based on the favourable comparison of our films with computational studies of the growth of deposited films of liquids, it would appear that our films are in liquid state. If this is the case, the interlocking patchwork is a very unexpected mode of deposition: given the very high surface tension of liquid gallium, highly regular spheres

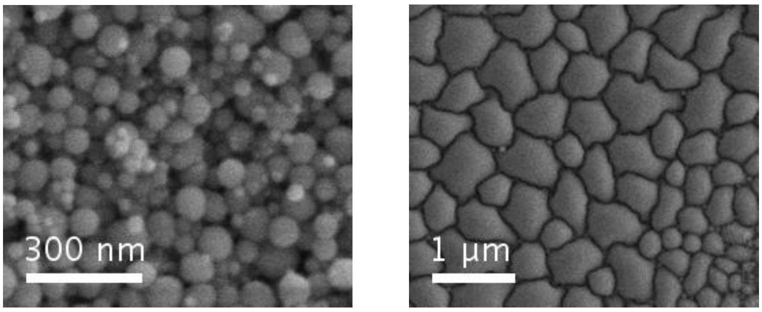

(a) Zero dosage **(b)** $0.41\,\mathrm{mC\,cm^{-2}}$

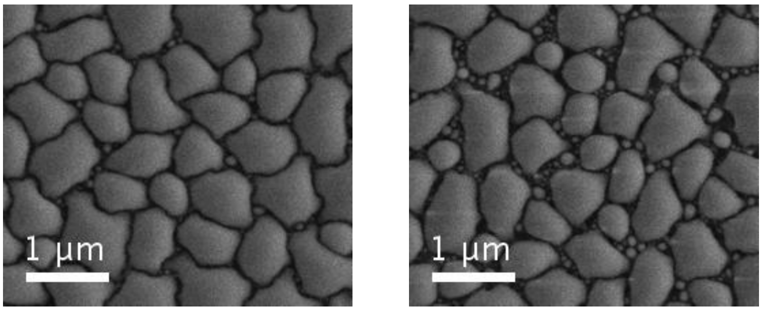

(c) $1.08\,\mathrm{mC\,cm^{-2}}$ **(d)** $1.5\,\mathrm{mC\,cm^{-2}}$

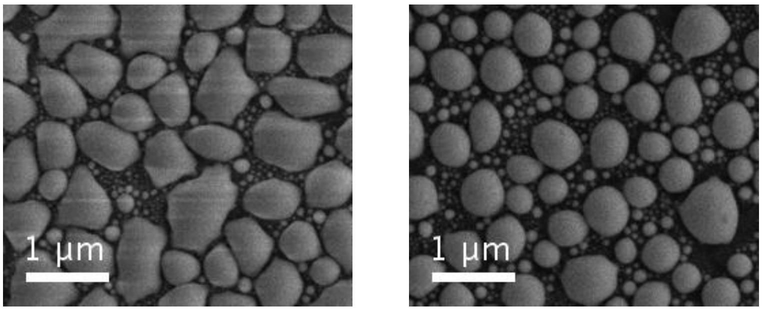

(e) $2.86\,\mathrm{mC\,cm^{-2}}$ **(f)** $5.4\,\mathrm{mC\,cm^{-2}}$

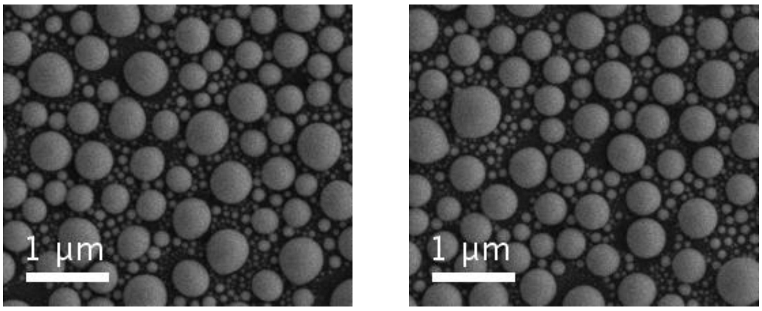

(g) $10.4\,\mathrm{mC\,cm^{-2}}$ **(h)** $20\,\mathrm{mC\,cm^{-2}}$

Figure C.1: Distribution of nanoparticles grown on PET with varying prior FIB gallium ion dosage: SEM imagery.

would be expected. The unusual surface properties introduced by gallium's oxide layer have previously explained the ability of the liquid element to enter sub-microscale grating structures with minimal pressure,[49] a situation that would be expected to require a pressure differential of several atmospheres across the gallium surface, based on a Young-Laplace treatment which is expected to be valid in the nanoscale regime.[63] It is presumed that this phenomenon is behind the unusual structures observed.

- Dosages sigificantly in excess of $1\,\mathrm{mC\,cm^{-2}}$ cause the nano-regions to begin to separate into islands with a greater tendency towards spherical particles. This tendency stabilises with highly spherical particles at around $10\,\mathrm{mC\,cm^{-2}}$ and does not appear to change beyond this point.

Without a detailed theoretical treatment it is not possible to be sure whether the observed phenomena are caused by surface roughening, ion implantation or both. Despite this, the significance of the effect is not in question and it must be taken into account in experiments requiring this combination of processes. Hence for the experiments discussed in chapter 7 involving these processes it was decided that areas otherwise not intended for structuring would receive a low $2.5\,\mathrm{mC\,cm^{-2}}$ dosage in order to normalise surface properties across both milled and unmilled areas.

Appendix D

Publications

D.1 Journal Publications

- R. Waters, P. Hobson, K. F. MacDonald, N. I. Zheludev - “Phase change nonlinearity at a gallium metasurface”, submitted for publication in Journal of Optics special issue "Low-intensity Nonlinear Optics" (reference JOPT-104413)
- R. Waters, A. Ohtsu, P. Hobson, K. F. MacDonald, N. I. Zheludev - “Templated assembly of metal nanoparticle films on polymer substrates”, Applied Physics Letters **109**, 263105 (2016)
- R. Waters, P. Hobson, K. F. MacDonald, N. I. Zheludev - “Optically switchable photonic metasurfaces”, Applied Physics Letters **107**, 081102 (2016)

D.2 Conference contributions

- (oral) R. Waters, P. Hobson, K. F. MacDonald, N. I. Zheludev - “All-optical switching of photonic metamaterials enabled by surface-mediated phase transitions in gallium” - 9th International Congress on Advanced Electromagnetic Materials in Microwaves and Optics - Metamaterials ’15 University of Oxford 7-12 Sep 2015
- (oral) R. Waters, K. F. MacDonald, P. Hobson, N. I. Zheludev - “Optically switchable gallium metasurfaces”, CLEO/Europe - EQEC Munich 21-25 Jun 2015
- (oral) R. Waters, K. F. MacDonald, P. Hobson, N. I. Zheludev - “Adaptive photonic meta-surfaces exploiting interfacial phase change in elemental gallium”, CLEO ’14 San Jose, CA 8-13 Jun 2014
- (poster) R. Waters, K. F. MacDonald, P. Hobson, N. I. Zheludev - “Adaptive Photonic Metamaterials” - DSTL MAST programme conference, 23 Oct 2013

Bibliography

[1] N. Liu, M. Mesch, T. Weiss, M. Hentschel, and H. Giessen, “Infrared perfect absorber and its application as plasmonic sensor.,” *Nano Letters*, vol. 10, pp. 2342–8, jul 2010.

[2] J. Zhao, Q. Cheng, J. Chen, M. Q. Qi, W. X. Jiang, and T. J. Cui, “A tunable metamaterial absorber using varactor diodes,” *New Journal of Physics*, vol. 15, p. 043049, apr 2013.

[3] M. A. Kats, D. Sharma, J. Lin, P. Genevet, R. Blanchard, Z. Yang, M. M. Qazilbash, D. N. Basov, S. Ramanathan, and F. Capasso, “Ultra-thin perfect absorber employing a tunable phase change material,” *Applied Physics Letters*, vol. 101, no. 22, p. 221101, 2012.

[4] F. Aieta, P. Genevet, M. A. Kats, N. Yu, R. Blanchard, Z. Gaburro, and F. Capasso, “Aberration-free ultrathin flat lenses and axicons at telecom wavelengths based on plasmonic metasurfaces.,” *Nano Letters*, vol. 12, pp. 4932–6, sep 2012.

[5] I. M. Ehrenberg, S. E. Sarma, and B.-I. Wu, “A three-dimensional self-supporting low loss microwave lens with a negative refractive index,” *Journal of Applied Physics*, vol. 112, no. 7, p. 073114, 2012.

[6] D. Schurig, J. J. Mock, B. J. Justice, S. A. Cummer, J. B. Pendry, A. F. Starr, and D. R. Smith, “Metamaterial electromagnetic cloak at microwave frequencies.,” *Science (New York, N.Y.)*, vol. 314, pp. 977–80, nov 2006.

[7] H. Hu, D. Ji, X. Zeng, K. Liu, and Q. Gan, “Rainbow trapping in hyperbolic metamaterial waveguide.,” *Scientific Reports*, vol. 3, p. 1249, jan 2013.

[8] N. Bloembergen, “Nonlinear Optics: past, present and future,” in *Guided Wave Nonlinear Optics*, pp. 1–9, Dordrecht: Springer Netherlands, 1992.

[9] E. A. Murphy, *Experimental Studies of Surface Melting and Time- Resolved Superheating of Metal Surfaces.* PhD thesis, University of Rochester, 1993.

[10] P. J. Bennett, S. Dhanjal, P. Petropoulos, D. J. Richardson, N. I. Zheludev, and V. I. Emel’yanov, “A photonic switch based on a gigantic, reversible optical nonlinearity of liquefying gallium,” *Applied Physics Letters*, vol. 73, no. 13, pp. 1787–1789, 1998.

[11] M. Lapine, I. V. Shadrivov, and Y. S. Kivshar, “Colloquium: Nonlinear metamaterials,” *Reviews of Modern Physics*, vol. 86, no. September, pp. 1093–1123, 2014.

[12] R. M. Walser, “Electromagnetic metamaterials,” pp. 1–15, International Society for Optics and Photonics, jul 2001.

[13] E. E. Narimanov and A. V. Kildishev, “Optical black hole: Broadband omnidirectional light absorber,” *Applied Physics Letters*, vol. 95, no. 4, p. 041106, 2009.

[14] D. T. Emerson, “The work of Jagadis Chandra Bose: 100 years of millimeter-wave research,” *IEEE Transactions on Microwave Theory and Techniques*, vol. 45, no. 12 PART 2, pp. 2267–2273, 1997.

[15] V. V. Georgievich, “THE ELECTRODYNAMICS OF SUBSTANCES WITH SIMULTANEOUSLY NEGATIVE VALUES OF ϵ AND μ,” *Soviet Physics USPEKI 10*, vol. 509, 1968.

[16] J. Pendry, A. Holden, D. Robbins, and W. Stewart, “Magnetism from conductors and enhanced nonlinear phenomena,” *IEEE Transactions on Microwave Theory and Techniques*, vol. 47, no. 11, pp. 2075–2084, 1999.

[17] J. B. Pendry, D. Schurig, and D. R. Smith, “Controlling electromagnetic fields.,” *Science (New York, N.Y.)*, vol. 312, pp. 1780–2, jun 2006.

[18] I. B. Vendik, O. G. Vendik, M. A. Odit, D. V. Kholodnyak, S. P. Zubko, M. F. Sitnikova, P. A. Turalchuk, K. N. Zemlyakov, I. V. Munina, D. S. Kozlov, V. M. Turgaliev, and A. B. Ustinov, “Tunable Metamaterials for Controlling THz Radiation,” *IEEE Transactions on Terahertz Science and Technology*, vol. 2, pp. 538–549, sep 2012.

[19] M. Beresna, M. Gecevicius, P. G. Kazansky, and T. Gertus, “Radially polarized optical vortex converter created by femtosecond laser nanostructuring of glass,” *Applied Physics Letters*, vol. 98, no. 20, p. 201101, 2011.

[20] H.-T. Chen, J. F. O’Hara, A. K. Azad, A. J. Taylor, R. D. Averitt, D. B. Shrekenhamer, and W. J. Padilla, “Experimental demonstration of frequency-agile terahertz metamaterials,” *Nature Photonics*, vol. 2, pp. 295–298, apr 2008.

[21] T. Driscoll, S. Palit, M. M. Qazilbash, M. Brehm, F. Keilmann, B.-G. Chae, S.-J. Yun, H.-T. Kim, S. Y. Cho, N. M. Jokerst, D. R. Smith, and D. N. Basov, “Dynamic tuning of an infrared hybrid-metamaterial resonance using vanadium dioxide,” *Applied Physics Letters*, vol. 93, no. 2, p. 024101, 2008.

[22] X. R. Jin, Y. Q. Zhang, S. Zhang, Y. Lee, and J. Y. Rhee, “Polarization-independent electromagnetically induced transparency-like effects in stacked metamaterials based on FabryâĂŞPerot resonance,” *Journal of Optics*, vol. 15, p. 125104, dec 2013.

[23] S. Zeng, K.-T. Yong, I. Roy, X.-Q. Dinh, X. Yu, and F. Luan, “A Review on Functionalized Gold Nanoparticles for Biosensing Applications,” *Plasmonics*, vol. 6, pp. 491–506, apr 2011.

[24] J. Zhang, K. F. MacDonald, and N. I. Zheludev, “Near-infrared trapped mode magnetic resonance in an all-dielectric metamaterial,” *Optics Express*, vol. 21, p. 26721, oct 2013.

[25] Y. Fu and M. Qiu, *Optical Properties of Nanostructures.* Pan Stanford, 2011.

[26] J. M. Pitarke, V. M. Silkin, E. V. Chulkov, and P. M. Echenique, “Theory of surface plasmons and surface-plasmon polaritons,” *Reports on Progress in Physics*, vol. 70, pp. 1–87, jan 2007.

[27] E. Wu, Y. Chi, B. Wu, K. Xia, Y. Yokota, K. Ueno, H. Misawa, and H. Zeng, “Spatial polarization sensitivity of single Au bowtie nanostructures,” *Journal of Luminescence*, vol. 131, pp. 1971–1974, sep 2011.

[28] T. J. Davis and E. Hendry, “Superchiral electromagnetic fields created by surface plasmons in nonchiral metallic nanostructures,” *Physical Review B*, vol. 87, p. 085405, feb 2013.

[29] B. Liedberg, C. Nylander, and I. Lunström, “Surface plasmon resonance for gas detection and biosensing,” *Sensors and Actuators*, vol. 4, pp. 299–304, jan 1983.

[30] Z. Chen, *Grating Coupled Surface Plasmons in Metallic Structures.* PhD thesis, University of Exeter, 2007.

[31] J. Parsons, E. Hendry, J. R. Sambles, and W. L. Barnes, “Localized surface-plasmon resonances and negative refractive index in nanostructured electromagnetic metamaterials,” *Physical Review B*, vol. 80, p. 245117, dec 2009.

[32] O. Nicoletti, F. de la Peña, R. K. Leary, D. J. Holland, C. Ducati, and P. a. Midgley, “Three-dimensional imaging of localized surface plasmon resonances of metal nanoparticles,” *Nature*, vol. 502, pp. 80–4, oct 2013.

[33] N. P. Johnson, A. Z. Khokhar, H. M. Chong, R. M. Rue, T. J. Antosiewicz, and S. McMeekin, “A review of size and geometrical factors influencing resonant frequencies in metamaterials,” *Opto-Electronics Review*, vol. 14, no. 3, pp. 187–191, 2006.

[34] T. Xu, A. Agrawal, M. Abashin, K. J. Chau, and H. J. Lezec, “All-angle negative refraction and active flat lensing of ultraviolet light,” *Nature*, vol. 497, pp. 470–4, may 2013.

[35] V. Heine, “Crystal structure of gallium metal,” *Journal of Physics C (Proceedings of the Physical Society)*, vol. 1, p. 222, 1968.

[36] M. Bernasconi, G. L. Chiarotti, and E. Tosatti, “Ab initio calculations of structural and electronic properties of gallium solid-state phases,” *Physical Review B*, vol. 52, no. 14, pp. 9988–9998, 1995.

[37] R. Kofman, P. Cheyssac, and J. Richard, “Optical properties of Ga monocrystal in the 0.3-5-eV range,” *Physical Review B*, vol. 16, pp. 5216–5224, dec 1977.

[38] J. C. Maxwell Garnett, “Colours in Metal Glasses and in Metallic Films,” *Philosophical Transactions of the Royal Society of London*, vol. 203, pp. 385–420, 1904.

[39] O. Hunderi and R. Ryberg, “Amorphous gallium-a free electron metal,” *Journal of Physics F: Metal Physics*, vol. 4, pp. 2096–2102, nov 1974.

[40] W. J. Huisman, J. F. Peters, M. J. Zwanenburg, S. A. de Vries, T. E. Derry, D. Abernathy, and J. Friso van der Veen, “Layering of a liquid metal in contact with a hard wall,” *Nature*, vol. 390, no. November, pp. 379–381, 1997.

[41] K. F. MacDonald, V. A. Fedotov, R. W. Eason, N. I. Zheludev, A. V. Rode, B. Luther-Davies, and V. I. Emel’yanov, “Light-induced metallization in laser-deposited gallium films,” *Journal of the Optical Society of America B*, vol. 18, no. 3, pp. 331–334, 2001.

[42] V. Albanis, S. Dhanjal, V. A. Fedotov, K. F. MacDonald, N. I. Zheludev, P. Petropoulos, D. J. Richardson, and V. I. Emel’yanov, “Nanosecond dynamics of a gallium mirror’s light-induced reflectivity change,” *Physical Review B*, vol. 63, p. 165207, 2001.

[43] J. E. E. Inglesfield, “The structure and phase changes of gallium,” *Journal of Physics C (Proceedings of the Physical Society)*, vol. 1, p. 1337, 1968.

[44] B. F. Soares, F. Jonsson, and N. I. Zheludev, “All-optical phase-change memory in a single gallium nanoparticle,” *Physical Review Letters*, vol. 98, p. 153905, 2007.

[45] B. F. Soares, K. F. MacDonald, V. A. Fedotov, and N. I. Zheludev, “Light-Induced Switching between Structural Forms with Different Optical Properties in a Single Gallium Nanoparticulate,” *Nano Letters*, vol. 5, pp. 2104–2107, oct 2005.

[46] M. Losurdo, A. Suvorova, S. Rubanov, K. Hingerl, and A. S. Brown, “Thermally stable coexistence of liquid and solid phases in gallium nanoparticles,” *Nature Materials*, vol. 15, pp. 995–1002, jul 2016.

[47] P. Petropoulos, H. L. Offerhaus, D. J. Richardson, S. Dhanjal, and N. I. Zheludev, “Passive Q-switching of fiber lasers using a broadband liquefying gallium mirror,” *Applied Physics Letters*, vol. 74, no. 24, pp. 3619–3621, 1999.

[48] A. V. Krasavin, K. F. MacDonald, N. I. Zheludev, and A. V. Zayats, “High-contrast modulation of light with light by control of surface plasmon polariton wave coupling,” *Applied Physics Letters*, vol. 85, no. 16, pp. 3369–3371, 2004.

[49] S. R. C. Vivekchand, C. J. Engel, S. M. Lubin, M. G. Blaber, W. Zhou, J. Y. Suh, G. C. Schatz, and T. W. Odom, “Liquid plasmonics: manipulating surface plasmon polaritons via phase transitions,” *Nano Letters*, vol. 12, pp. 4324–8, aug 2012.

[50] A. V. Krasavin and N. I. Zheludev, “Active plasmonics: Controlling signals in Au/Ga waveguide using nanoscale structural transformations,” *Applied Physics Letters*, vol. 84, no. 8, pp. 1416–1418, 2004.

[51] J. Wei, Z. Wang, W. Chen, and D. H. Cobden, “New aspects of the metal-insulator transition in single-domain vanadium dioxide nanobeams,” *Nature nanotechnology*, vol. 4, pp. 420–4, jul 2009.

[52] M. Lankhorst, “Modelling glass transition temperatures of chalcogenide glasses. Applied to phase-change optical recording materials,” *Journal of Non-Crystalline Solids*, vol. 297, pp. 210–219, feb 2002.

[53] J. N. Hodgson, “The optical properties of liquid indium, cadmium, bismuth and antimony,” *Philosophical Magazine*, vol. 7, no. 74, pp. 229–236, 1962.

[54] H.-T. Chen, “Interference theory of metamaterial perfect absorbers,” *Optics express*, vol. 20, pp. 7165–72, mar 2012.

[55] H. Okamoto, “Ga-Ni (Gallium-Nickel),” *Journal of Phase Equilibria and Diffusion*, vol. 29, pp. 296–296, apr 2008.

[56] M. Hida, A. Sakakibara, and H. Kamiyabu, “Surface Tension and Supercooling Phenomena of Liquid Ga,” 1988.

[57] M. K. Lee, C. Tien, E. V. Charnaya, H. S. Sheu, and Y. A. Kumzerov, “Structural variations in nanosized confined gallium,” *Physics Letters, Section A: General, Atomic and Solid State Physics*, vol. 374, no. 13-14, pp. 1570–1573, 2010.

[58] C. Tien, C. S. Wur, K. J. Lin, E. V. Charnaya, and Y. A. Kumzerov, “Freezing and melting of gallium in porous glass,” *Solid State Communications*, vol. 104, no. 12, pp. 753–757, 1997.

[59] R. C. Hugo and R. G. Hoagland, “In-situ TEM observation of aluminium embrittlement by liquid gallium,” *Scripta Materialia*, vol. 38, no. 3, pp. 523–529, 1998.

[60] R. C. Hugo and R. G. Hoagland, “The kinetics of gallium penetration into aluminium grain boundaries - in situ TEM observations and atomistic models,” *Acta Materialia*, vol. 48, pp. 1949–1957, 2000.

[61] A. V. Krasavin, K. F. MacDonald, A. S. Schwanecke, and N. I. Zheludev, “Gallium/Aluminum nano-composite material for nonlinear optics and nonlinear plasmonics,” *Applied Physics Letters*, vol. 89, no. 3, p. 31118, 2006.

[62] H. Ibach, *Physics of Surfaces and Interfaces.* Springer Berlin Heidelberg, 1 ed., 2006.

[63] H. Liu and G. Cao, “Effectiveness of the Young-Laplace equation at nanoscale,” *Scientific Reports*, vol. 6, p. 23936, 2016.

[64] L. J. Briggs, “Gallium: Thermal Conductivity; Supercooling; Negative Pressure,” *The Journal of Chemical Physics*, vol. 26, no. 4, p. 784, 1957.

[65] Q. Xu, N. Oudalov, Q. Guo, H. M. Jaeger, and E. Brown, “Effect of oxidation on the mechanical properties of liquid gallium and eutectic gallium-indium,” *Physics of Fluids*, vol. 24, p. 063101, jan 2012.

[66] A. Di Cicco, “Phase transitions in confined gallium droplets,” *Physical Review Letters*, vol. 81, no. 14, pp. 2942–2945, 1998.

[67] S. J. Vavilov and W. L. Lewschin, “Die Beziehungen zwischen Fluoreszenz und Phosphoreszenz in festen und flüssigen Medien,” *Z. Phys.*, vol. 25, p. 920, 1926.

[68] M. Göppert-Mayer, “Uber Elementarakte mit zwei Quantensprüngen,” *Annalen der Physik*, vol. 401, no. 3, pp. 273–294, 1931.

[69] P. A. Franken, A. E. Hill, C. W. Peters, and G. Weinreich, “Generation of optical harmonics,” *Physical Review Letters*, vol. 7, no. 4, pp. 118–119, 1961.

[70] G. Mayer and F. Gires, “Action of an intense light beam on the refractive index of liquids,” *Comptes Rendus, Acad. Sci. Paris*, vol. 258, p. 2039, 1964.

[71] F. J. Hsieh and W. C. Wang, “Full extraction methods to retrieve effective refractive index and parameters of a bianisotropic metamaterial based on material dispersion models,” *Journal of Applied Physics*, vol. 112, no. 6, 2012.

[72] M. Ren, B. Jia, J.-Y. Ou, E. Plum, J. Zhang, K. F. MacDonald, A. E. Nikolaenko, J. Xu, M. Gu, and N. I. Zheludev, “Nanostructured plasmonic medium for terahertz bandwidth all-optical switching.,” *Advanced Materials (Deerfield Beach, Fla.)*, vol. 23, pp. 5540–4, dec 2011.

[73] G. A. Wurtz, R. Pollard, W. Hendren, G. P. Wiederrecht, D. J. Gosztola, V. A. Podolskiy, and A. V. Zayats, “Designed ultrafast optical nonlinearity in a plasmonic nanorod metamaterial enhanced by nonlocality,” *Nature nanotechnology*, vol. 6, pp. 107–11, mar 2011.

[74] A. Nikolaenko, N. Papasimakis, A. Chipouline, F. D. Angelis, E. D. Fabrizio, and N. I. Zheludev, “THz bandwidth optical switching with carbon nanotube metamaterial,” *Optics . . .*, vol. 20, no. 6, pp. 6068–6079, 2012.

[75] A. E. Nikolaenko, N. Papasimakis, E. Atmatzakis, Z. Luo, Z. X. Shen, F. De Angelis, S. A. Boden, E. Di Fabrizio, and N. I. Zheludev, “Nonlinear graphene metamaterial,” *Applied Physics Letters*, vol. 100, no. 18, p. 181109, 2012.

[76] D. J. Cho, W. Wu, E. Ponizovskaya, P. Chaturvedi, A. M. Bratkovsky, S.-Y. Wang, X. Zhang, F. Wang, and Y. R. Shen, “Ultrafast modulation of optical metamaterials.,” *Optics express*, vol. 17, no. 20, pp. 17652–17657, 2009.

[77] K. M. Dani, Z. Ku, P. C. Upadhya, R. P. Prasankumar, S. R. J. Brueck, and A. J. Taylor, “Subpicosecond optical switching with a negative index metamaterial,” *Nano Letters*, vol. 9, no. 10, pp. 3565–3569, 2009.

[78] R. W. Boyd, *Nonlinear Optics*. 3 ed., 2008.

[79] E. Plum, “Giant optical nonlinearity and magnetoelectric effect in reconfigurable plasmonic metamaterials,” in *Metamaterials*, 2014.

[80] V. M. Shalaev, *Optical Metamaterials: Fundamentals and Applications*. 2009.

[81] W. M. Zhu, A. Q. Liu, X. M. Zhang, D. P. Tsai, T. Bourouina, J. H. Teng, X. H. Zhang, H. C. Guo, H. Tanoto, T. Mei, G. Q. Lo, and D. L. Kwong, “Switchable magnetic metamaterials using micromachining processes.,” *Advanced Materials (Deerfield Beach, Fla.)*, vol. 23, pp. 1792–6, apr 2011.

[82] H. Tao, A. Strikwerda, K. Fan, W. Padilla, X. Zhang, and R. Averitt, “Reconfigurable Terahertz Metamaterials,” *Physical Review Letters*, vol. 103, p. 147401, oct 2009.

[83] W. M. Zhu, a. Q. Liu, W. Zhang, J. F. Tao, T. Bourouina, J. H. Teng, X. H. Zhang, Q. Y. Wu, H. Tanoto, H. C. Guo, G. Q. Lo, and D. L. Kwong, “Polarization dependent state to polarization independent state change in THz metamaterials,” *Applied Physics Letters*, vol. 99, no. 22, p. 221102, 2011.

[84] J.-Y. Ou, E. Plum, J. Zhang, and N. I. Zheludev, “An electromechanically reconfigurable plasmonic metamaterial operating in the near-infrared.,” *Nature nanotechnology*, vol. 8, pp. 252–5, apr 2013.

[85] J. Valente, J.-Y. Ou, E. Plum, I. J. Youngs, and N. I. Zheludev, “A magneto-electro-optical effect in a plasmonic nanowire material,” *Nature Communications*, vol. 6, p. 7021, 2015.

[86] B. Dong, W. M. Zhu, Y. H. Fu, J. M. Tsai, H. Cai, D. L. Kwong, E. P. Li, E. Rius, and A. Q. Liu, “An absorptive filter using microfluidic switchable metamaterials,” in *2011 16th International Solid-State Sensors, Actuators and Microsystems Conference*, no. c, pp. 530–533, IEEE, jun 2011.

[87] J. Li, C. M. Shah, W. Withayachumnankul, B. S.-Y. Ung, A. Mitchell, S. Sriram, M. Bhaskaran, S. Chang, and D. Abbott, “Mechanically tunable terahertz metamaterials,” *Applied Physics Letters*, vol. 102, no. 12, p. 121101, 2013.

[88] M. Lapine, I. V. Shadrivov, D. a. Powell, and Y. S. Kivshar, “Magnetoelastic metamaterials.,” *Nature Materials*, vol. 11, pp. 30–3, jan 2012.

[89] I. M. Pryce, K. Aydin, Y. A. Kelaita, R. M. Briggs, and H. A. Atwater, “Highly strained compliant optical metamaterials with large frequency tunability.,” *Nano Letters*, vol. 10, pp. 4222–7, oct 2010.

[90] S. Lee, S. Kim, T.-T. Kim, Y. Kim, M. Choi, S. H. Lee, J.-Y. Kim, and B. Min, “Reversibly stretchable and tunable terahertz metamaterials with wrinkled layouts.,” *Advanced Materials (Deerfield Beach, Fla.)*, vol. 24, pp. 3491–7, jul 2012.

[91] A. Karvounis, J. Y. Ou, W. Wu, K. F. Macdonald, and N. I. Zheludev, “Nano-optomechanical nonlinear dielectric metamaterials,” *Applied Physics Letters*, vol. 107, no. 19, 2015.

[92] A. P. Slobozhanyuk, M. Lapine, D. A. Powell, I. V. Shadrivov, Y. S. Kivshar, R. C. McPhedran, and P. A. Belov, “Flexible helices for nonlinear metamaterials.,” *Advanced Materials (Deerfield Beach, Fla.)*, vol. 25, pp. 3409–12, jul 2013.

[93] C. Tang, Q. Wang, F. Liu, Z. Chen, and Z. Wang, “Optical forces in twisted split-ring-resonator dimer stereometamaterials,” *Optics express*, vol. 21, pp. 11783–11793, jan 2013.

[94] M. Liu, Y. Sun, D. A. Powell, I. V. Shadrivov, M. Lapine, R. C. McPhedran, and Y. S. Kivshar, “Nonlinear response via intrinsic rotation in metamaterials,” *Physical Review B*, vol. 87, p. 235126, jun 2013.

[95] K. Fan, X. Zhao, J. Zhang, K. Geng, G. R. Keiser, H. R. Seren, G. D. Metcalfe, M. Wraback, X. Zhang, and R. D. Averitt, “Optically Tunable Terahertz Metamaterials on Highly Flexible Substrates,” *IEEE Transactions on Terahertz Science and Technology*, vol. 3, pp. 702–708, nov 2013.

[96] R. Yahiaoui, J. P. Guillet, F. de Miollis, and P. Mounaix, “Ultra-flexible multiband terahertz metamaterial absorber for conformal geometry applications,” *Optics letters*, vol. 38, pp. 4988–90, dec 2013.

[97] W. M. Zhu, X. M. Zhang, A. Q. Liu, H. Cai, T. Jonathan, and T. Bourouina, “A micromachined optical double well for thermo-optic switching via resonant tunneling effect,” *Applied Physics Letters*, vol. 92, no. 25, p. 251101, 2008.

[98] G. Stenning and G. Bowden, “Magnetic control of a meta-molecule,” *Opt. Express21 (. . .*, vol. 21, p. 9, jul 2013.

[99] Y. He, P. He, S. Dae Yoon, P. Parimi, F. Rachford, V. Harris, and C. Vittoria, “Tunable negative index metamaterial using yttrium iron garnet,” *Journal of Magnetism and Magnetic Materials*, vol. 313, pp. 187–191, jun 2007.

[100] M. Lei, N. Feng, Q. Wang, Y. Hao, S. Huang, and K. Bi, “Magnetically tunable metamaterial perfect absorber,” *Journal of Applied Physics*, vol. 119, no. 24, p. 244504, 2016.

[101] H.-T. Chen, W. J. Padilla, J. M. O. Zide, A. C. Gossard, A. J. Taylor, and R. D. Averitt, “Active terahertz metamaterial devices.,” *Nature*, vol. 444, pp. 597–600, nov 2006.

[102] K. Fan, H. Y. Hwang, M. Liu, A. C. Strikwerda, A. Sternbach, J. Zhang, X. Zhao, X. Zhang, K. A. Nelson, and R. D. Averitt, “Nonlinear Terahertz Metamaterials via Field-Enhanced Carrier Dynamics in GaAs,” *Physical Review Letters*, vol. 110, p. 217404, may 2013.

[103] Y. C. Jun, J. Reno, T. Ribaudo, E. Shaner, J.-J. Greffet, S. Vassant, F. Marquier, M. Sinclair, and I. Brener, “Epsilon-Near-Zero Strong Coupling in Metamaterial-Semiconductor Hybrid Structures.,” *Nano Letters*, pp. 1–6, oct 2013.

[104] X. Shen and T. J. Cui, “Photoexcited broadband redshift switch and strength modulation of terahertz metamaterial absorber,” *Journal of Optics*, vol. 14, p. 114012, nov 2012.

[105] A. J. Hoffman, L. Alekseyev, S. S. Howard, K. J. Franz, D. Wasserman, V. a. Podolskiy, E. E. Narimanov, D. L. Sivco, and C. Gmachl, “Negative refraction in semiconductor metamaterials.,” *Nature Materials*, vol. 6, pp. 946–50, dec 2007.

[106] C. Rizza, A. Ciattoni, L. Columbo, M. Brambilla, and F. Prati, “Terahertz optically tunable dielectric metamaterials without microfabrication.,” *Optics letters*, vol. 38, pp. 1307–9, apr 2013.

[107] W. J. Padilla, A. J. Taylor, C. Highstrete, M. Lee, and R. D. Averitt, “Dynamical electric and magnetic metamaterial response at terahertz frequencies,” *Conference on Lasers and Electro-Optics and 2006 Quantum Electronics and Laser Science Conference, CLEO/QELS 2006*, vol. 1, pp. 12–13, 2006.

[108] N. H. Shen, M. Massaouti, M. Gokkavas, J. M. Manceau, E. Ozbay, M. Kafesaki, T. Koschny, S. Tzortzakis, and C. M. Soukoulis, “Optically implemented broadband blueshift switch in the terahertz regime,” *Physical Review Letters*, vol. 106, no. 3, pp. 1–4, 2011.

[109] V. Albanis, S. Dhanjal, K. F. MacDonald, P. Petropoulos, H. L. Offerhaus, D. J. Richardson, A. V. Rode, and N. I. Zheludev, “The light-induced structural phase transition in confining gallium and its photonic applications,” *Journal of Luminescence*, vol. 87-89, pp. 646–648, 2000.

[110] K. MacDonald and N. Zheludev, “Active plasmonics: current status,” *Laser & Photonics Reviews*, vol. 4, pp. 562–567, dec 2009.

[111] Y. Zhou, X. Chen, C. Ko, Z. Yang, C. Mouli, and S. Ramanathan, “Voltage-Triggered Ultrafast Phase Transition in Vanadium Dioxide Switches,” *IEEE Electron Device Letters*, vol. 34, pp. 220–222, feb 2013.

[112] J. S. Kyoung, M. A. Seo, S. M. Koo, H. R. Park, H. S. Kim, B. J. Kim, H. T. Kim, N. K. Park, D. S. Kim, and K. J. Ahn, “Active terahertz metamaterials: Nano-slot antennas on VO2 thin films,” *Physica Status Solidi (C)*, vol. 8, pp. 1227–1230, apr 2011.

[113] C. Ye, D. Hewak, M. Hempstead, B. Samson, and D. Payne, “Spectral properties of Er3+-doped gallium lanthanum sulphide glass,” *Journal of Non-Crystalline Solids*, vol. 208, pp. 56–63, nov 1996.

[114] Z. L. Sámson, K. F. MacDonald, F. De Angelis, B. Gholipour, K. Knight, C. C. Huang, E. Di Fabrizio, D. W. Hewak, and N. I. Zheludev, “Metamaterial electro-optic switch of nanoscale thickness,” *Applied Physics Letters*, vol. 96, no. 14, p. 143105, 2010.

[115] B. Gholipour, J. Zhang, K. F. MacDonald, D. W. Hewak, and N. I. Zheludev, “An all-optical, non-volatile, bidirectional, phase-change meta-switch,” *Advanced Materials*, vol. 25, pp. 3050–3054, apr 2013.

[116] T. Cao, L. Zhang, R. E. Simpson, and M. J. Cryan, “Mid-infrared tunable polarization-independent perfect absorber using a phase-change metamaterial,” *Journal of the Optical Society of America B*, vol. 30, p. 1580, may 2013.

[117] T. Cao, R. E. Simpson, and M. J. Cryan, “Study of tunable negative index metamaterials based on phase-change materials,” *Journal of the Optical Society of America B*, vol. 30, p. 439, jan 2013.

[118] Q. Wang, E. T. F. Rogers, B. Gholipour, C.-M. Wang, G. Yuan, J. Teng, and N. I. Zheludev, “Optically reconfigurable metasurfaces and photonic devices based on phase change materials,” *2*, vol. 10, no. 1, pp. 60–65, 2015.

[119] F. Morin, “Oxides Which Show a Metal-to-Insulator Transition at the Neel Temperature,” *Physical Review Letters*, vol. 3, pp. 34–36, jul 1959.

[120] E. E. Chain, “Optical properties of vanadium dioxide and vanadium pentoxide thin films.,” *Applied optics*, vol. 30, pp. 2782–7, jul 1991.

[121] D. W. Ferrara, J. Nag, E. R. MacQuarrie, A. B. Kaye, and R. F. Haglund, “Plasmonic probe of the semiconductor to metal phase transition in vanadium dioxide.,” *Nano Letters*, vol. 13, pp. 4169–75, sep 2013.

[122] D. Hilton, R. Prasankumar, S. Fourmaux, A. Cavalleri, D. Brassard, M. El Khakani, J. Kieffer, A. Taylor, and R. Averitt, “Enhanced Photosusceptibility near Tc for the Light-Induced

Insulator-to-Metal Phase Transition in Vanadium Dioxide," *Physical Review Letters*, vol. 99, p. 226401, nov 2007.

[123] M. Liu, H. Y. Hwang, H. Tao, A. C. Strikwerda, K. Fan, G. R. Keiser, A. J. Sternbach, K. G. West, S. Kittiwatanakul, J. Lu, S. A. Wolf, F. G. Omenetto, X. Zhang, K. A. Nelson, and R. D. Averitt, "Terahertz-field-induced insulator-to-metal transition in vanadium dioxide metamaterial.," *Nature*, vol. 487, pp. 345–8, jul 2012.

[124] M. Seo, J. Kyoung, H. Park, S. Koo, H.-s. Kim, H. Bernien, B. J. Kim, J. H. Choe, Y. H. Ahn, H.-T. Kim, N. Park, Q.-H. Park, K. Ahn, and D.-s. Kim, "Active terahertz nanoantennas based on VO2 phase transition.," *Nano Letters*, vol. 10, pp. 2064–8, jun 2010.

[125] M. J. Dicken, K. Aydin, I. M. Pryce, L. A. Sweatlock, E. M. Boyd, S. Walavalkar, J. Ma, and H. A. Atwater, "Frequency tunable near-infrared metamaterials based on VO2 phase transition.," *Optics express*, vol. 17, pp. 18330–9, sep 2009.

[126] M. D. Goldflam, T. Driscoll, B. Chapler, O. Khatib, N. Marie Jokerst, S. Palit, D. R. Smith, B.-J. Kim, G. Seo, H.-T. Kim, M. D. Ventra, and D. N. Basov, "Reconfigurable gradient index using VO2 memory metamaterials," *Applied Physics Letters*, vol. 99, no. 4, p. 044103, 2011.

[127] O. Buchnev, J. Y. Ou, M. Kaczmarek, N. I. Zheludev, and V. A. Fedotov, "Electro-optical control in a plasmonic metamaterial hybridised with a liquid-crystal cell.," *Optics express*, vol. 21, pp. 1633–8, jan 2013.

[128] S. Xiao, U. K. Chettiar, A. V. Kildishev, V. Drachev, I. C. Khoo, and V. M. Shalaev, "Tunable magnetic response of metamaterials," *Applied Physics Letters*, vol. 95, no. 3, p. 033115, 2009.

[129] A. Diaz, J. Liou, and M. V. Stinger, "Liquid Crystals Tunable Optical Metamaterials," *IEEE Journal of Selected Topics in Quantum Electronics*, vol. 16, no. 2, pp. 410–417, 2010.

[130] Z. Liu, C.-Y. Huang, H. Liu, X. Zhang, and C. Lee, "Resonance enhancement of terahertz metamaterials by liquid crystals/indium tin oxide interfaces.," *Optics express*, vol. 21, pp. 6519–25, mar 2013.

[131] D. Shrekenhamer, W.-C. Chen, and W. J. Padilla, "Liquid Crystal Tunable Metamaterial Absorber," *Physical Review Letters*, vol. 110, p. 177403, apr 2013.

[132] X.-w. Lin, J.-b. Wu, W. Hu, Z.-g. Zheng, Z.-j. Wu, G. Zhu, F. Xu, B.-b. Jin, and Y.-q. Lu, "Self-polarizing terahertz liquid crystal phase shifter," *AIP Advances*, vol. 1, no. 3, p. 032133, 2011.

[133] F. Zhang, W. Zhang, Q. Zhao, J. Sun, K. Qiu, J. Zhou, and D. Lippens, "Electrically controllable fishnet metamaterial based on nematic liquid crystal.," *Optics express*, vol. 19, pp. 1563–8, jan 2011.

[134] M. Rippa, P. Mormile, R. Capasso, M. Zanella, and L. Petti, "Electro-Optical Tuning in Photonic Crystals âĹŠ Dispersed Liquid Crystalline Metamaterials," *Molecular Crystals and Liquid Crystals*, vol. 573, pp. 18–25, may 2013.

[135] O. Buchnev, N. Podoliak, M. Kaczmarek, N. I. Zheludev, and V. A. Fedotov, "Electrically Controlled Nanostructured Metasurface Loaded with Liquid Crystal: Toward Multifunctional Photonic Switch," *Advanced Optical Materials*, vol. 3, no. 5, pp. 674–679, 2015.

[136] N. Papasimakis, Z. Luo, Z. X. Shen, F. De Angelis, E. Di Fabrizio, A. E. Nikolaenko, and N. I. Zheludev, "Graphene in a photonic metamaterial.," *Optics express*, vol. 18, pp. 8353–9, apr 2010.

[137] W. Zhu, I. D. Rukhlenko, L.-M. Si, and M. Premaratne, "Graphene-enabled tunability of optical fishnet metamaterial," *Applied Physics Letters*, vol. 102, no. 12, p. 121911, 2013.

[138] L. Ju, B. Geng, J. Horng, C. Girit, M. Martin, Z. Hao, H. A. Bechtel, X. Liang, A. Zettl, Y. R. Shen, and F. Wang, "Graphene plasmonics for tunable terahertz metamaterials.," *Nature nanotechnology*, vol. 6, pp. 630–4, oct 2011.

[139] H. Yan, X. Li, B. Chandra, G. Tulevski, Y. Wu, M. Freitag, W. Zhu, P. Avouris, and F. Xia, "Tunable infrared plasmonic devices using graphene/insulator stacks," *Nature nanotechnology*, vol. 7, pp. 330–4, may 2012.

[140] R. R. Nair, P. Blake, A. N. Grigorenko, K. S. Novoselov, T. J. Booth, T. Stauber, N. M. R. Peres, and A. K. Geim, "Fine structure constant defines visual transparency of graphene," *Science (New York, N.Y.)*, vol. 320, p. 1308, jun 2008.

[141] W. Zhu, I. D. Rukhlenko, and M. Premaratne, "Graphene metamaterial for optical reflection modulation," *Applied Physics Letters*, vol. 102, no. 24, p. 241914, 2013.

[142] H. Cheng, S. Chen, P. Yu, J. Li, B. Xie, Z. Li, and J. Tian, "Dynamically tunable broadband mid-infrared cross polarization converter based on graphene metamaterial," *Applied Physics Letters*, vol. 103, no. 22, p. 223102, 2013.

[143] Y. Rapoport, V. Grimalsky, I. Iorsh, N. Kalinich, S. Koshevaya, C. Castrejon-Martinez, and Y. S. Kivshar, "Nonlinear reshaping of terahertz pulses with graphene metamaterials," *JETP Letters*, vol. 98, pp. 503–506, dec 2013.

[144] D. A. Powell, I. V. Shadrivov, and Y. S. Kivshar, "Nonlinear electric metamaterials," *Applied Physics Letters*, vol. 95, no. 8, p. 084102, 2009.

[145] I. V. Shadrivov, A. B. Kozyrev, D. W. van der Weide, and Y. S. Kivshar, "Tunable transmission and harmonic generation in nonlinear metamaterials," *Applied Physics Letters*, vol. 93, no. 16, p. 161903, 2008.

[146] I. Gil and J. Bonache, "Tunable metamaterial transmission lines based on varactor-loaded split-ring resonators," *Microwave Theory and Techniques*, vol. 54, pp. 2665–2674, jun 2006.

[147] D. Shrekenhamer, S. Rout, A. C. Strikwerda, C. Bingham, R. D. Averitt, S. Sonkusale, and W. J. Padilla, "High speed terahertz modulation from metamaterials with embedded high electron mobility transistors," *Optics express*, vol. 19, pp. 9968–75, may 2011.

[148] W. L. Chan, H.-T. Chen, A. J. Taylor, I. Brener, M. J. Cich, and D. M. Mittleman, "A spatial light modulator for terahertz beams," *Applied Physics Letters*, vol. 94, no. 21, p. 213511, 2009.

[149] V. Savinov, V. A. Fedotov, P. A. de Groot, and N. I. Zheludev, "Electro-optical modulation of sub-terahertz radiation with superconducting metamaterial," *Conference on Lasers and Electro-Optics 2012*, p. CTh1D.1, 2012.

[150] V. Savinov, V. A. Fedotov, P. a. J. de Groot, and N. I. Zheludev, "Radiation-harvesting resonant superconducting sub-THz metamaterial bolometer," *Superconductor Science and Technology*, vol. 26, p. 084001, aug 2013.

[151] A. E. Nikolaenko, F. De Angelis, S. A. Boden, N. Papasimakis, P. Ashburn, E. Di Fabrizio, and N. I. Zheludev, "Carbon Nanotubes in a Photonic Metamaterial," *Physical Review Letters*, vol. 104, p. 153902, apr 2010.

[152] I. Al-Naib, G. Sharma, M. M. Dignam, H. Hafez, A. Ibrahim, D. G. Cooke, T. Ozaki, and R. Morandotti, "Effect of local field enhancement on the nonlinear terahertz response of a silicon-based metamaterial," *Physical Review B*, vol. 88, p. 195203, nov 2013.

[153] F. Zhang, X. Hu, Y. Zhu, H. Yang, and Q. Gong, "Ultralow-power all-optical tunable dual Fano resonances in nonlinear metamaterials," *Applied Physics Letters*, vol. 103, no. 19, p. 191116, 2013.

[154] G. V. Naik, V. M. Shalaev, and A. Boltasseva, "Alternative plasmonic materials: beyond gold and silver," *Advanced Materials (Deerfield Beach, Fla.)*, vol. 25, pp. 3264–94, jun 2013.

[155] M. Born, E. Wolf, A. B. Bhatia, P. C. Clemmow, D. Gabor, A. R. Stokes, A. M. Taylor, P. A. Wayman, and W. L. Wilcock, *Principles of Optics.* Cambridge: Cambridge University Press, 1999.

[156] O. S. Heavens, *Optical Properties of Thin Solid Films.* Courier Corporation, 1991.

[157] A. Arbabi and L. L. Goddard, “Measurements of the refractive indices and thermo-optic coefficients of Si_3N_4 and SiO_x using microring resonances,” *Optics Letters*, vol. 38, p. 3878, oct 2013.

[158] S. Shu, Z. Li, and Y. Y. Li, “Triple-layer Fabry-Pérot absorber with near- perfect absorption in visible and near-infrared regime,” vol. 21, no. 21, pp. 4795–4801, 2013.

[159] V. A. Fedotov, P. L. Mladyonov, S. L. Prosvirnin, and N. I. Zheludev, “Planar electromagnetic metamaterial with a fish scale structure,” *Physical Review E - Statistical, Nonlinear, and Soft Matter Physics*, vol. 72, no. 5, pp. 1–4, 2005.

[160] J. Hao, J. Wang, X. Liu, W. J. Padilla, L. Zhou, and M. Qiu, “High performance optical absorber based on a plasmonic metamaterial,” *Applied Physics Letters*, vol. 96, no. 25, pp. 3–5, 2010.

[161] K. Aydin, V. E. Ferry, R. M. Briggs, and H. A. Atwater, “Broadband polarization-independent resonant light absorption using ultrathin plasmonic super absorbers,” *Nature Communications*, vol. 2, p. 517, 2011.

[162] C. M. Watts, X. Liu, and W. J. Padilla, “Metamaterial electromagnetic wave absorbers.,” *Advanced Materials (Deerfield Beach, Fla.)*, vol. 24, pp. OP98–120, OP181, jun 2012.

[163] X. Liu, T. Starr, A. F. Starr, and W. J. Padilla, “Infrared Spatial and Frequency Selective Metamaterial with Near-Unity Absorbance,” *Physical Review Letters*, vol. 104, p. 207403, may 2010.

[164] P. Petropoulos, H. S. Kim, D. J. Richardson, V. A. Fedotov, and N. I. Zheludev, “Light-induced metallization at the gallium-silica interface,” *Physical Review B*, vol. 64, p. 193312, 2001.

[165] P. Moitra, B. A. Slovick, W. Li, I. I. Kravchencko, D. P. Briggs, S. Krishnamurthy, and J. Valentine, “Large-Scale All-Dielectric Metamaterial Perfect Reflectors,” *ACS Photonics*, vol. 2, no. 6, pp. 692–698, 2015.

[166] L. D. Landau, “On the theory of phase transitions,” *Zh. Eks. Teor. Fiz.*, vol. 7, no. 1937, pp. 19–32, 1937.

[167] R. Lipowsky, “Critical surface phenomena at first-order bulk transitions,” *Physical Review Letters*, vol. 49, no. 21, pp. 1575–1578, 1982.

[168] R. Trittibach, C. Grutter, and J. H. Bilgram, “Surface melting of gallium single crystals,” *Physical Review B*, vol. 50, no. 4, pp. 2529–2536, 1994.

[169] A. Samanta, M. E. Tuckerman, T.-Q. Yu, and W. E, “Microscopic mechanisms of equilibrium melting of a solid,” *Science*, vol. 346, pp. 729–732, nov 2014.

[170] V. A. Fedotov, *Photonics of Nanoscale Structural Transitions in Confined Gallium.* PhD thesis, University of Southampton, 2002.

[171] Z. B. Hou and R. Komanduri, “General solutions for stationary/moving plane heat source problems in manufacturing and tribology,” *International Journal of Heat and Mass Transfer*, vol. 43, no. 10, pp. 1679–1698, 2000.

[172] K. F. MacDonald, V. A. Fedotov, N. I. Zheludev, B. V. Zhdanov, and R. J. Knize, “Structural phase transition as a mechanism for broadband, low-threshold reflectivity switching in gallium,” *Applied Physics Letters*, vol. 79, no. 15, p. 2375, 2001.

[173] V. Albanis, V. A. Fedotov, and N. I. Zheludev, “Light-induced reflectivity switching in gallium-on-silica films in the blueâĂŞgreen spectral region,” *Optics Communications*, vol. 214, pp. 271–276, 2002.

[174] V. A. Fedotov, K. F. MacDonald, N. I. Zheludev, and V. I. Emel’yanov, “Light-controlled growth of gallium nanoparticles,” *Journal of Applied Physics*, vol. 93, no. 6, pp. 3540–3544, 2003.

[175] V. A. Fedotov and K. MacDonald, “Nanoscale light-induced melting as a mechanism for broadband optical switching,” *Nonlinear Optics, Quantum Optics*, vol. 30, no. 1, pp. 53–76, 2003.

[176] X. G. Gong, G. L. Chiarotti, M. Parrinello, and E. Tosatti, “a-gallium: A metallic molecular crystal,” *Physical Review B*, vol. 43, no. 17, pp. 14277–14280, 1991.

[177] J. Zhang, J.-y. Ou, N. Papasimakis, Y. Chen, K. F. MacDonald, and N. I. Zheludev, “Continuous metal plasmonic frequency selective surfaces,” *Optics Express*, vol. 19, p. 23279, nov 2011.

[178] A. R. Parker, “515 million years of structural colour,” *Journal of Optics A: Pure and Applied Optics*, vol. 2, pp. R15–R28, nov 2000.

[179] M. A. Kats, R. Blanchard, S. Zhang, P. Genevet, C. Ko, S. Ramanathan, and F. Capasso, “Vanadium Dioxide as a Natural Disordered Metamaterial: Perfect Thermal Emission and Large Broadband Negative Differential Thermal Emittance,” *Physical Review X*, vol. 3, p. 041004, oct 2013.

[180] G. Wang, X. Chen, S. Liu, C. Wong, and S. Chu, “Mechanical Chameleon through Dynamic Real-Time Plasmonic Tuning,” *ACS Nano*, vol. 10, no. 2, pp. 1788–1794, 2016.

[181] R. de Waele, S. P. Burgos, A. Polman, and H. A. Atwater, “Plasmon Dispersion in Coaxial Waveguides from Single-Cavity Optical Transmission Measurements,” *Nano Letters*, vol. 9, pp. 2832–2837, aug 2009.

[182] S. Hardy, “The surface tension of liquid gallium,” *Journal of Crystal Growth*, vol. 71, pp. 602–606, may 1985.

[183] M. D. Dickey, R. C. Chiechi, R. J. Larsen, E. A. Weiss, D. A. Weitz, and G. M. Whitesides, “Eutectic Gallium-Indium (EGaIn): A Liquid Metal Alloy for the Formation of Stable Structures in Microchannels at Room Temperature,” *Advanced Functional Materials*, vol. 18, pp. 1097–1104, apr 2008.

[184] B. F. Soares, K. F. MacDonald, V. A. Fedotov, and N. I. Zheludev, “Light-induced switching between structural forms with different optical properties in a single gallium nanoparticulate,” *Nano Letters*, vol. 5, pp. 2104–2107, 2005.

[185] S. Vignolini, N. A. Yufa, P. S. Cunha, S. Guldin, I. Rushkin, M. Stefik, K. Hur, U. Wiesner, J. J. Baumberg, and U. Steiner, “A 3D optical metamaterial made by self-assembly,” *Advanced Materials*, vol. 24, no. 10, pp. 23–27, 2012.

[186] A. García Marín, M. J. Hernández, E. Ruiz, J. M. Abad, E. Lorenzo, J. Piqueras, and J. L. Pau, “Immunosensing platform based on gallium nanoparticle arrays on silicon substrates,” *Biosensors and Bioelectronics*, vol. 74, pp. 1069–1075, 2015.

[187] S. Sacanna, D. J. Pine, and G.-R. Yi, “Engineering shape: the novel geometries of colloidal self-assembly,” *Soft Matter*, vol. 9, pp. 8096–8106, 2013.

[188] A. R. Chandrasekaran and R. Zhuo, “A ‘tile’ tale: Hierarchical self-assembly of DNA lattices,” *Applied Materials Today*, vol. 2, pp. 7–16, 2016.

[189] L. Holland, “The Growth, Structure and Physical Properties of Vacuum Deposited Films,” in *Vacuum Deposition of Thin Films*, ch. 7, pp. 199–246, Aberdeen University Press Ltd, 1 ed., 1963.

[190] E. Søndergård, R. Kofman, P. Cheyssac, and A. Stella, “Production of nanostructures by self-organization of liquid Volmer-Weber films,” *Surface Science*, vol. 364, no. 3, pp. 467–476, 1996.

[191] B. E. Roustom, G. Fóti, and C. Comninellis, “Preparation of gold nanoparticles by heat treatment of sputter deposited gold on boron-doped diamond film electrode,” *Electrochemistry Communications*, vol. 7, no. 4, pp. 398–405, 2005.

[192] A. Di Cicco, S. Fusari, and S. Stizza, "Phase transitions and undercooling in confined gallium," *Philosophical Magazine Part B*, vol. 79, no. 11-12, pp. 2113–2120, 1999.

[193] P. Meakin, "Droplet deposition growth and coalescence," *Reports on Progress in Physics*, vol. 55, no. 2, pp. 157–240, 1992.

[194] J. Schindelin, I. Arganda-Carreras, E. Frise, V. Kaynig, M. Longair, T. Pietzsch, S. Preibisch, C. Rueden, S. Saalfeld, B. Schmid, J.-Y. Tinevez, D. J. White, V. Hartenstein, K. Eliceiri, P. Tomancak, and A. Cardona, "Fiji: an open-source platform for biological-image analysis.," *Nature methods*, vol. 9, no. 7, pp. 676–82, 2012.

[195] P. G. De Gennes, "Wetting: Statics and dynamics," *Reviews of Modern Physics*, vol. 57, no. 3, pp. 827–863, 1985.

[196] M. J. Regan, H. Tostmann, P. S. Pershan, O. M. Magnussen, E. DiMasi, B. M. Ocko, and M. Deutsch, "X-ray study of the oxidation of liquid-gallium surfaces," *Physical Review B*, vol. 55, no. 16, pp. 10786–10790, 1997.

[197] G. Wyszecki and W. S. Stiles, *Color Science: concepts and methods, quantitative data and formulae.* Wiley, 2000.

[198] E. D. Palik, *Handbook of Optical Constants of Solids.* Elsevier, 1998.